LUND UNIVERSITY

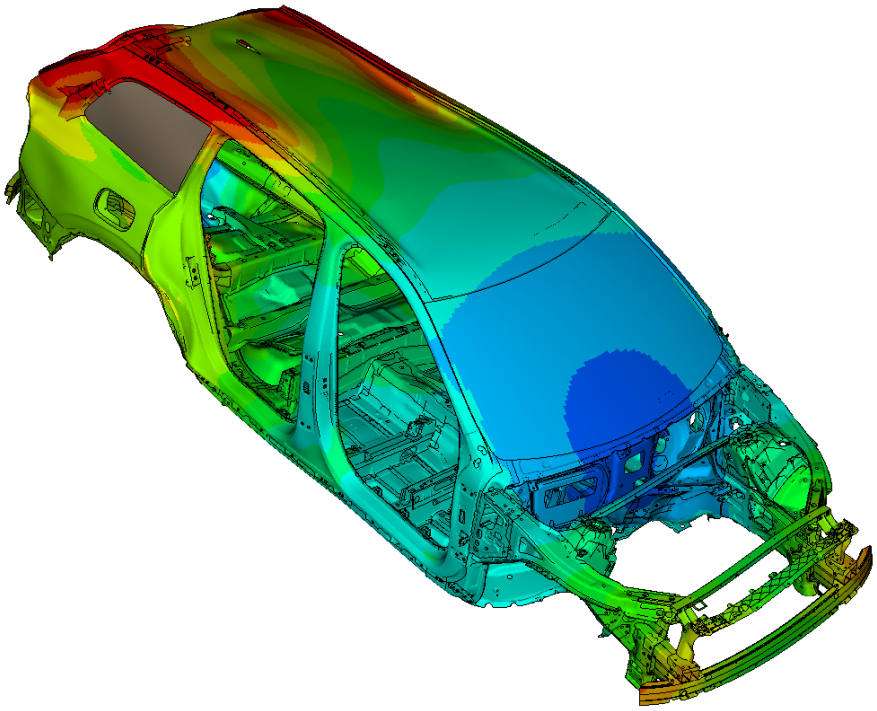

CONCEPTUAL DYNAMIC ANALYSIS OF A VEHICLE BODY

BJÖRN PEDERSEN

Structural Mechanics

Master's Dissertation

DEPARTMENT OF CONSTRUCTION SCIENCES
DIVISION OF STRUCTURAL MECHANICS

ISRN LUTVDG/TVSM--18/5233--SE (1-103) | ISSN 0281-6679
MASTER'S DISSERTATION

CONCEPTUAL DYNAMIC ANALYSIS OF A VEHICLE BODY

BJÖRN PEDERSEN

Supervisors: **PETER PERSSON**, PhD, Division of Structural Mechanics, LTH
and **OLA FLODÉN**, PhD, Volvo Cars.
Examiner: Professor **KENT PERSSON**, Division of Structural Mechanics, LTH.

Printed by V-husets tryckeri LTH, Lund, Sweden, October 2018 *(Pl)*.

For information, address:
Division of Structural Mechanics,
Faculty of Engineering LTH, Lund University, Box 118, SE-221 00 Lund, Sweden.
Homepage: www.byggmek.lth.se

Abstract

The noise, vibration and harshness (NVH) and body dynamic performance of automotive vehicles is highly dependent of the components included in the body structure and compartment, since they add mass, stiffness and damping to the overall structure. Today, the noise levels in the compartment are predicted using complex and detailed computational models during both early and late stages of the vehicle development process. However, detailed information regarding the vehicle structure is limited during the concept phase, which makes the predictions unreliable.

This dissertation investigates if simpler and more robust measures for the vehicle body could instead be used to describe the NVH performance in the concept phase. Three different measures of the vehicle body without trim items was investigated: 1) eigenfrequencies of global bending, torsion and yaw modes, 2) global static bending and torsional stiffness, and 3) a mobility index which reflects the vibrational velocities of the structural frame. In order to decide on appropriate measures, the correlation between the NVH performance of the vehicle body with trim items and the results of the simpler measures is evaluated using linear regression. To evaluate the NVH performance of the complete vehicle body a road noise index representing the broad-band acoustic pressure due to a load resulting from the interaction between the car and road surface was created. This road noise index was used as a measure of the NVH performance of the vehicle body with trim items. These measures are calculated on a finite element (FE) representation of the vehicle.

The correlation was first investigated on a selection of vehicles currently in production by Volvo Cars. Also, a case study was performed on one of the vehicles by modifying its structural properties. It was concluded that the mobility index offers the best correlation out of the early measures investigated, and is a possible robust and simple alternative measure usable in the early concept development stages.

Acknowledgements

This master dissertation was carried out as a joint project at the Division of Structural Mechanics at LTH and the Noise & Vibration Center at Volvo Car Corporation. The work was carried out at Volvo Cars in Gothenburg during the spring and summer of 2018.

I would like to start off by thanking my supervisor Peter Persson at LTH for his guidance. I would also like to extend my gratitude to my supervisor Ola Flodén at Volvo Cars. He has provided countless helpful ideas and vital insight throughout this period. This dissertation could not have been done without his enthusiastic spirit and expertise. Furthermore I want to thank all my colleagues at Volvo Cars, too many to name, who has helped me with issues, big and small, and shown interest in this dissertation. You have shown me what a well functioning workplace looks like.

Finally I would like to thank my family and friends for all their love and support. Especially I would like to thank my girlfriend Kajsa, for putting up with my antics and giving me the motivation necessary to complete this task.

Gothenburg, September 2018

Björn Pedersen

Contents

1. Introduction

1.1 Background

In the automotive industry, different computer-aided engineering (CAE) methods are employed in the development of cars. CAE based methods reduce the need for physical prototypes of the vehicle, which helps to reduce both the time and cost of the development. The complexity of the product leads to great difficulties in ensuring that the vehicle satisfies the requirements on different attributes, such as fuel efficiency, crash performance or noise levels, which often are in conflict with each other. Efficient design iterations and attribute balancing based on CAE methods require that the CAE models are able to deliver results with sufficient accuracy. The performance related to noise, vibration and harshness (NVH) is one of the attributes which is of great importance when producing premium quality vehicles. This dissertation investigates CAE analysis of the NVH performance of car bodies, with focus on methods that are useful in early concept development stages.

Figure 1.1 shows what in this dissertation is defined as the body in grey (BIG). The BIG is one of the stages the body undergoes during production. The BIG consists mainly of welded and bolted sheet metal parts, most often some type of steel. Some parts, especially those made of aluminum are cast. An important distinction of the BIG from other stages of production of the body is that the windshield has been attached, but the body does not completely enclose the interior cavity. The vehicle body is the single biggest component of the car, and a majority of the other components are in some way

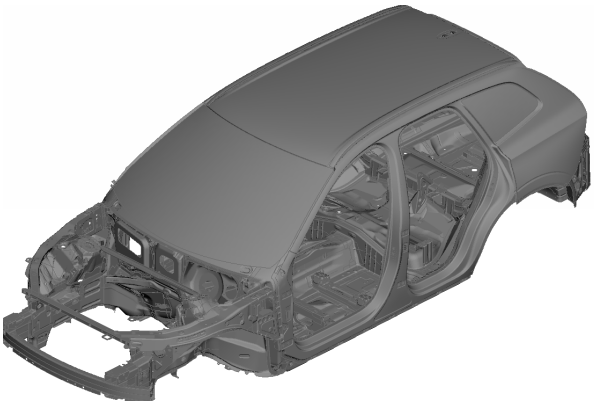

Figure 1.1: Body in Grey (BIG) of one of the vehicles produced by Volvo Cars.

attached to it. The often large panels, such as the roof or floor, of the body makes for good emitters of sound. The body is as stated also structurally attached to sources of vibrations, such as the engine or the tyres through the wheel suspension. The fluid cavity that makes up the cabin in which the passenger of the vehicle is settled has most of it's interface with the body. Hence the dynamic behavior of the body is of great importance for the noise level induced by, for example, the engine and tyres.

The freedom to alter design parameters, such as geometry of the body, is greater in the early stages of the development. At the same time a limited knowledge of the final design imposes difficulties in analyzing the effect of different design changes in the early stages. Streamlining the work in improving the performance related to NVH in an early concept development phase has been investigated to great extent. Different types of optimization methods employed on a vehicle body, or comparable structures, has been investigated by [1, 6, 7, 11, 14, 20]. These studies employ some method of simplifying the virtual model of certain parts of the body. One way of simplifying the virtual model is by using 1-dimensional beam elements and some proposed joint element, such an approach is used by [6, 7, 14, 20]. Some potential sources of errors in using this approach and possible corrections is investigated by [13]. In order to ensure the accuracy of the suggested methods, the cited studies evaluate different objective measures that can be employed on the simplified models. One common approach is to ensure that the simplified model has similar static and/or dynamic stiffness as the reference model, see for example [5, 6, 14, 20]. Multiple ways in validating the stiffness are used in the studies. One is to utilize some defined load case meant to represent the global stiffness. Another is to identify specific points important for passenger comfort or for the behavior of the simplified beam structure. Another measure often employed in combination with the previous is to perform a modal analysis of the simplified model and to compare the results with the modal analysis of the reference model, this is used by [5, 6, 14, 20]. Other measures, such as panel mobility [1] or total radiated power [11] are also used to validate the results. None of the cited papers investigate the correlation of the objective measures of the car body to the NVH performance of the complete vehicle. This is investigated in this dissertation.

1.2 Objective

Often in the automotive industry, the CAE models used throughout the development stages include a detailed representation of the vehicle body along with a complete fluid cavity and trim items such as dashboard and seats. The trim items are often represented using CAE models from older cars, before new designs are available. These detailed models of the vehicle body are used to calculate the sound pressure level in the cabin, which is computationally intensive and leads to highly uncertain results in the early design phase, when knowledge of the final design is limited.

A problem with using such a model, which can yield more accurate results once the design of the trimmed vehicle body is more detailed, is that it becomes a black box where proposed design changes influences the results in an unpredictable way. This leads to a situation where results are hard to interpret and the work to find the root cause of an issue

becomes very extensive, and once found, finding a reasonable solution might be equally difficult.

More simple measures such as the ones used for validating the simpler models described in the Section 1.1, are often evaluated for the BIG. The results of these computations are more robust than calculating the sound pressure levels, and can with a higher degree of certainty be tracked throughout the development stages.

The question then becomes if these simpler measures reflect the performance of the trimmed vehicle body related to NVH. This dissertation investigates the correlation of different objective measures of a BIG to the overall NVH performance of the trimmed body. The long-term aim of the Master's dissertation is to provide an understanding of how different measures usable in early concept phases correlate to the overall NVH performance of the vehicle. Thus, the objective becomes to provide an evaluation of what simpler objective measures are usable in an early concept development phase. These simpler measures are based on measures which are either currently being used in the concept development process or can reasonably be assumed to affect the NVH performance.

1.3 Method

In order to gauge the overall performance of the final vehicle body related to NVH, and compare this performance to simpler measures, a definition of the NVH performance has to be defined. In this dissertation the final vehicle body is represented by the virtual model of the trimmed body of a vehicle currently in production. That is to say all components are modeled as accurately as possible since all designs are final and all necessary information is available. The trimmed body consists, in addition to the actual body, of all trim items such as, doors, dashboard, seats etc. A subset of vehicles produced by Volvo Cars has been selected for analysis. These are all built on the scalable product architecture (SPA), which simplifies the work since the attachments to other parts of the vehicle are of the same type. All different vehicle types currently produced on the SPA platform were included in the analysis. These include sports utility vehicles (SUVs), sedans and estates, and the propulsion types, internal combustion engine (ICE) and plug-in hybrid electric vehicle (PHEV). The cars for which the analysis in the dissertation has been performed are shown in Table 1.1.

Table 1.1: Cars subjected to analysis.

#	Vehicle Type	Propulsion
1	SUV	ICE
2	Sedan	ICE
3	Estate	ICE
4	SUV	ICE
5	Sedan	ICE
6	Estate	ICE
7	SUV	PHEV
8	SUV	PHEV
9	Sedan	PHEV

While NVH involves many different load cases, this dissertation only considers noise induced by road excitation, i.e. road noise. Generally, the road noise below 300 Hz is structurally borne, i.e. it is generated by structural vibrations propagating through the body. Above 300 Hz, airborne noise becomes more important. Only structurally borne noise is considered in this dissertation. The noise resulting from road excitation is one of the large contributors to the overall noise inside the cabin. Road noise can generally be divided into frequency regions which are especially problematic. The noise in those frequency regions originate from different physical phenomena. A low-frequency noise, named *Drumming*, a mid-frequency, named *Rumble*, and a high-frequency, named *Tyre Cavity*, are considered here. The specific frequency cut-offs, for the different types of road noise, used in this dissertation are shown in Table 1.2.

Table 1.2: Frequency cut-offs for the different types of road noise analysed.

Noise type	Lower limit [Hz]	High limit [Hz]
Drumming	30	60
Rumble	70	150
Tyre Cavity	170	240

2. Governing Theory

2.1 Structure-Acoustic Equations

In this section, the governing equations for a continuum mechanical formulation of a structure acoustic system are presented. Continuum mechanics assumes that it is possible to describe the physical behavior of the material without modeling the discrete particles that make up the material, instead it is considered as a macroscopically averaged continuum. These formulations are shown for the structural domain which makes up the vehicle body, the acoustic domain in the vehicle cabin, and the coupling of these two domains.

2.1.1 Structural Domain

Starting with Newton's second law for a solid, the equations of motion for a body occupying an arbitrary domain V is derivable as [15]

$$\sigma_{ij,j} + b_i = \rho^s \ddot{u}_i, \tag{2.1}$$

where σ_{ij} is the stress tensor, the subscript $\bullet_{m,n}$ denotes the gradient $\dfrac{\partial \bullet_m}{\partial x_n}$, b_i is the body force tensor, ρ^s is the mass density of the solid, and $\ddot{u}_i$ is the acceleration tensor.If the deformation gradient $u_{i,j}$ is assumed to be small, the strain tensor is given by

$$\varepsilon_{ij} = \frac{1}{2}(u_{i,j} + u_{j,i}). \tag{2.2}$$

Assuming linear elastic behavior yields the stress strain relationship as

$$\sigma_{ij} = D_{ijkl}\varepsilon_{kl}, \tag{2.3}$$

where D_{ijkl} is the elastic stiffness tensor. At the surface S of the domain V, a traction vector t_i is defined as

$$t_i = \sigma_{ij} n_j, \tag{2.4}$$

where n_j is the outer normal unit vector of the surface S. Boundary conditions (BC) are defined on the surface S of the region V as either prescribed displacements or tractions as

$$\begin{aligned} u_i &= u_i^{bc} \qquad \text{on } S^u, \\ t_i &= t_i^{bc} \qquad \text{on } S^t, \end{aligned} \tag{2.5}$$

where S^u and S^t are separate parts of the surface S that together with the structure-acoustic coupling surface make up the entirety of S and u_i^{bc} and t_i^{bc} are known quantities.

2.1.2 Acoustic Domain

The governing equations, assuming inviscid, irrotational and small displacements, for a fluid domain can be derived as the equation of motion [18]

$$\rho_0^f \ddot{u}_i + \partial_i p = 0, \tag{2.6}$$

and the continuity equation

$$\dot{p} + \rho_0^f c_0^2 \partial_i \dot{u}_i = 0, \tag{2.7}$$

where ρ_0^f is the static density, c_0 is the speed of sound, p is the acoustic pressure, $\partial_i p$ is the gradient of the scalar field p and $\partial_i \dot{u}_i$ is the divergence of the vector field $\dot{u}_i$. Differentiation of (2.7) with respect to time and combining it with (2.6) yields

$$\frac{1}{c_0^2}\ddot{p} - \partial_i \partial_i p = 0. \tag{2.8}$$

In addition to the structure-acoustic coupling the BCs can be defined in multiple ways. The type of BC used in this dissertation is a prescribed pressure gradient on a rigid surface as

$$n_i \partial_i p = 0 \qquad \text{on } S^{\nabla p}. \tag{2.9}$$

2.1.3 Coupling

Modeling structure-acoustic interaction requires a boundary $S^{s,f}$, which is the surface shared by the structural and acoustic domain, to be introduced. On this surface the following relations are enforced

$$\begin{aligned} n_i^f u_i^s &= n_i^f u_i^f, \\ n_i^f t_i^s &= -p^f, \end{aligned} \tag{2.10}$$

where the superscript s denotes the solid and f the fluid domain. These relations represent a continuity in displacements and forces on the surface $S^{s,f}$. Use has been made of

$$n_i^s = -n_i^f \qquad \text{on } S^{s,f}.$$

2.2 Finite Element Formulation

The finite element (FE) formulation allows the previously shown differential equations, which are not feasible to solve analytically for a complex system, to be discretized into a numerically solvable structure. This is done by some assumptions and simplifications and does not offer the exact results, but is used throughout the automotive industry because it provides results with sufficient accuracy, in a time efficient manner, compared to the analytical solution to these differential equations.

2.2.1 Structural Domain

Multiplying (2.1) with an arbitrary weight function ν_i, integrating over the volume and using the divergence theorem, as well as defining a quantity $\varepsilon^{\nu}_{ij} = \frac{1}{2}(\nu_{i,j} + \nu_{j,i})$ and using the symmetry of σ_{ij}

$$\nu_{i,j}\sigma_{ij} = \frac{1}{2}(\nu_{i,j}\sigma_{ij} + \nu_{j,i}\sigma_{ji}) = \frac{1}{2}(\nu_{i,j}\sigma_{ij} + \nu_{j,i}\sigma_{ij}) = \epsilon^{\nu}_{ij}\sigma_{ij},$$

yields the weak form of the equations of motion

$$\int_V \rho^s \nu_i \ddot{u}_i dV + \int_V \varepsilon^v_{ij}\sigma_{ij} dV = \int_S \nu_i t_i dS + \int_V \nu_i b_i dV. \tag{2.11}$$

This may be rewritten using Voigt notation in vector form with the quantities

$$\boldsymbol{\varepsilon}^{\nu} = \begin{bmatrix} \varepsilon^{\nu}_{11} \\ \varepsilon^{\nu}_{22} \\ \varepsilon^{\nu}_{33} \\ 2\varepsilon^{\nu}_{12} \\ 2\varepsilon^{\nu}_{13} \\ 2\varepsilon^{\nu}_{23} \end{bmatrix}, \qquad \boldsymbol{\sigma} = \begin{bmatrix} \sigma_{11} \\ \sigma_{22} \\ \sigma_{33} \\ \sigma_{12} \\ \sigma_{13} \\ \sigma_{23} \end{bmatrix}, \qquad \ddot{\boldsymbol{u}} = \begin{bmatrix} \ddot{u}_1 \\ \ddot{u}_2 \\ \ddot{u}_3 \end{bmatrix}, \qquad \boldsymbol{\nu} = \begin{bmatrix} \nu_1 \\ \nu_2 \\ \nu_3 \end{bmatrix}, \qquad \boldsymbol{t} = \begin{bmatrix} t_1 \\ t_2 \\ t_3 \end{bmatrix}, \qquad \boldsymbol{b} = \begin{bmatrix} b_1 \\ b_2 \\ b_3 \end{bmatrix},$$

resulting in

$$\int_V \rho_s \boldsymbol{\nu}^T \ddot{\boldsymbol{u}} dV + \int_V (\boldsymbol{\varepsilon}^{\nu})^T \boldsymbol{\sigma} dV = \int_S \boldsymbol{\nu}^T \boldsymbol{t} dS + \int_V \boldsymbol{\nu}^T \boldsymbol{b} dV, \tag{2.12}$$

where the bold quantities are the same as the tensor quantities except in vector form. By using Galerkin's method for determining the weight function, the following quantities are introduced:

$$\boldsymbol{\nu} = \boldsymbol{N}_s \boldsymbol{c}, \qquad \boldsymbol{B} = \frac{d\boldsymbol{N}_s}{dx_i}, \qquad \boldsymbol{\varepsilon}^{\nu} = \boldsymbol{B}\boldsymbol{c}, \qquad \boldsymbol{\varepsilon} = \boldsymbol{B}\boldsymbol{a}_s, \qquad \ddot{\boldsymbol{u}} = \boldsymbol{N}_s \ddot{\boldsymbol{a}}_s,$$

where $\boldsymbol{N}_s$ are the global shape functions, $\boldsymbol{c}$ is some arbitrary column matrix and $\boldsymbol{a}_s$ is the nodal displacements. (2.12) can then be rewritten as

$$\boldsymbol{c}^T \left[\left(\int_V \rho_s \boldsymbol{N}_s^T \boldsymbol{N}_s dV \right) \ddot{\boldsymbol{a}}_s + \int_V \boldsymbol{B}^T \boldsymbol{\sigma} dV - \int_S \boldsymbol{N}_s^T \boldsymbol{t} dS - \int_V \boldsymbol{N}_s^T \boldsymbol{b} dV \right] = 0. \tag{2.13}$$

By remembering that $\boldsymbol{c}$ is arbitrary and the linear elastic material relation of (2.3), the following quantities can be defined:

$$\boldsymbol{M}_s = \int_V \rho \boldsymbol{N}_s^T \boldsymbol{N}_s dV, \quad \boldsymbol{K}_s = \int_V \boldsymbol{B}^T \boldsymbol{D} \boldsymbol{B} dV, \quad \boldsymbol{f}_s = \int_S \boldsymbol{N}_s^T \boldsymbol{t} dS + \int_V \boldsymbol{N}_s^T \boldsymbol{b} dV = \boldsymbol{f}_{s,b} + \boldsymbol{f}_{s,l}.$$

Thus (2.13) can be rewritten as

$$\boldsymbol{M}_s \ddot{\boldsymbol{a}}_s + \boldsymbol{K}_s \boldsymbol{a}_s = \boldsymbol{f}_s, \tag{2.14}$$

where $\boldsymbol{M}_s$ is the mass matrix, $\boldsymbol{K}_s$ is the stiffness matrix and $\boldsymbol{f}_s$ the force vector. The BCs of (2.5) can be inserted as nodal values of $\boldsymbol{a}$ or $\boldsymbol{f}_{s,b}$.

2.2.2 Acoustic Domain

Similarly to the structural domain the weak formulation is obtained by multiplying (2.8) with an arbitrary weight function ν, integrating over the volume and using the divergence theorem as

$$\int_V \nu \frac{1}{c_0^2} \ddot{p} dV + \int_V \partial_i \nu \partial_i p dV = \int_S \nu n_i \partial_i p dS. \tag{2.15}$$

Using the approximation

$$p = \boldsymbol{N}_f \boldsymbol{a}_f,$$

where $\boldsymbol{N}_f$ are the global shape functions and $\boldsymbol{a_f}$ are the nodal pressures. Thus (2.15) can be rewritten in vector notation as

$$\boldsymbol{M}_f \ddot{\boldsymbol{a}}_f + \boldsymbol{K}_f \boldsymbol{a}_f = \boldsymbol{f}_f, \tag{2.16}$$

where

$$\boldsymbol{M}_f = \frac{1}{c_0^2} \int_V \rho \boldsymbol{N}_f^T \boldsymbol{N}_f dV, \qquad \boldsymbol{K}_f = \int_V (\boldsymbol{\nabla} \boldsymbol{N}_f)^T \boldsymbol{\nabla} \boldsymbol{N}_f dV, \qquad \boldsymbol{f}_f = \int_S \boldsymbol{N}_f^T \boldsymbol{n}_f^T \boldsymbol{\nabla} p dS.$$

2.2.3 Coupling of Domains

In order to obtain a finite element formulation for the coupled structure-acoustic system, the coupling matrix $\boldsymbol{H}_{s,f}$ is introduced as

$$\boldsymbol{H}_{s,f} = \int_{S^{s,f}} \boldsymbol{N}_s^T \boldsymbol{n}_f \boldsymbol{N}_f dS. \tag{2.17}$$

This allows (2.10) to be rewritten as

$$\begin{aligned} \boldsymbol{f}_f &= \boldsymbol{H}_{s,f} \boldsymbol{a}_f, \\ \boldsymbol{f}_{s,b} &= -\rho_{0,f} c_0^2 \boldsymbol{H}_{s,f}^T \ddot{\boldsymbol{a}}_s. \end{aligned} \tag{2.18}$$

Combining (2.18) with (2.14) and (2.16) yields the coupled system as

$$\begin{bmatrix} \boldsymbol{M}_s & \boldsymbol{0} \\ \rho_{0,f} c_0^2 \boldsymbol{H}_{s,f}^T & \boldsymbol{M}_f \end{bmatrix} \begin{bmatrix} \ddot{\boldsymbol{a}}_s \\ \ddot{\boldsymbol{a}}_f \end{bmatrix} + \begin{bmatrix} \boldsymbol{K}_s & -\boldsymbol{H}_{s,f} \\ \boldsymbol{0} & \boldsymbol{K}_f \end{bmatrix} \begin{bmatrix} \boldsymbol{a}_s \\ \boldsymbol{a}_f \end{bmatrix} = \begin{bmatrix} \boldsymbol{f}_{s,l} \\ \boldsymbol{0} \end{bmatrix} + \begin{bmatrix} \boldsymbol{f}_{s,b} \\ \boldsymbol{f}_{f,b} \end{bmatrix}. \tag{2.19}$$

2.3 Structural Dynamic Analysis

This section shows different ways of analyzing a dynamic system, more specifically a multi-degree of freedom (MDOF) system, e.g. the one in (2.14). For these types of analyses, a transformation from physical to modal coordinates is often beneficial. How this modal decomposition is performed and used is also shown. Finally, some useful metrics such as the modal assurance criterion (MAC) and the use of frequency response functions (FRFs) are shown and explained.

2.3.1 Modal Decomposition

For an undamped MDOF structural system experiencing free vibrations, (2.14) becomes

$$\boldsymbol{M}\ddot{\boldsymbol{a}}(t) + \boldsymbol{K}\boldsymbol{a}(t) = \boldsymbol{0}, \tag{2.20}$$

where $\boldsymbol{a}(t)$ is a function of time. Solutions to this differential equation can be found by making the ansatz

$$\boldsymbol{a}(t) = \hat{A} e^{i\omega t} \boldsymbol{\Phi}, \tag{2.21}$$

where $\hat{A}$ is the complex amplitude, i is the unit imaginary number, ω is the angular frequency and $\boldsymbol{\Phi}$ is a vector constant in time. Differentiating (2.21) with respect to time and inserting it into (2.20) yields

$$(\boldsymbol{K} - \omega^2 \boldsymbol{M})\boldsymbol{\Phi} = \boldsymbol{0}. \tag{2.22}$$

The solutions of which is found by solving for

$$\det(\boldsymbol{K} - \omega^2 \boldsymbol{M}) = \boldsymbol{0}, \tag{2.23}$$

which for an n degrees of freedoms (DOFs) system has n solutions, $\omega_j = \omega_1 \ \ldots \ \omega_n$, which are the eigenfrequencies of the system. By inserting the eigenfrequencies into (2.22), it is possible to solve for the corresponding mode shape, or eigenvector $\boldsymbol{\Phi}_j$. The eigenvectors $\boldsymbol{\Phi}$ form an orthogonal base. Therefore the solution to (2.20) can be described by the sum

$$\boldsymbol{a}(t) = \sum_{j=1}^{n} q_j(t) \boldsymbol{\Phi}_j, \tag{2.24}$$

where

$$q_j(t) = \hat{q}_j e^{i\omega_j t}. \tag{2.25}$$

$\hat{q}_j$ is determined by the initial conditions of the system and describes the complex amplitude of $\boldsymbol{\Phi}_j$.

2.3.2 Forced Harmonic Vibrations

If a structural system is subjected to a harmonic force, a steady state behavior will appear after an initial transient response. If harmonic excitations of an undamped MDOF system is assumed, (2.14) can be written as

$$\boldsymbol{M}\ddot{\boldsymbol{a}}(t) + \boldsymbol{K}\boldsymbol{a}(t) = \hat{\boldsymbol{f}}e^{i\omega t}, \tag{2.26}$$

where $\hat{\boldsymbol{f}}$ is the constant complex vector describing the distribution of the load. The solution to this differential equation is given by the complementary and particular solution. The complementary solution has already been acquired in (2.24). The particular solution is derived in a similar way by making the ansatz

$$\boldsymbol{a}(t) = \hat{\boldsymbol{a}}e^{i\omega t}, \tag{2.27}$$

where $\hat{\boldsymbol{a}}$ is a complex vector constant in time. Thus (2.26) can be rewritten in the frequency domain as

$$(\boldsymbol{K} - \omega^2\boldsymbol{M})\hat{\boldsymbol{a}} = \hat{\boldsymbol{f}}. \tag{2.28}$$

By multiplying this with $\boldsymbol{\Phi}_k^T$ from the left and modally decomposing $\hat{\boldsymbol{a}}$ as

$$\hat{\boldsymbol{a}} = \sum_{j=1}^{n} \hat{r}_j(t)\boldsymbol{\Phi}_j, \tag{2.29}$$

the following is acquired:

$$-\omega^2 \sum_{j=1}^{n} \boldsymbol{\Phi}_k^T\boldsymbol{M}\boldsymbol{\Phi}_j\hat{r}_j + \sum_{j=1}^{n} \boldsymbol{\Phi}_k^T\boldsymbol{K}\boldsymbol{\Phi}_j\hat{r}_j = \boldsymbol{\Phi}_k^T\hat{\boldsymbol{f}}. \tag{2.30}$$

Making use of the orthogonality criterion

$$\begin{aligned} \boldsymbol{\Phi}_i^T\boldsymbol{M}\boldsymbol{\Phi}_j = 0 \quad \text{if } i \neq j, \\ \boldsymbol{\Phi}_i^T\boldsymbol{K}\boldsymbol{\Phi}_j = 0 \quad \text{if } i \neq j, \end{aligned} \tag{2.31}$$

creates n uncoupled systems as

$$-\omega^2\mu_k\hat{r}_k + \kappa_k\hat{r}_k = f_k, \tag{2.32}$$

where

$$\mu_k = \boldsymbol{\Phi}_k^T\boldsymbol{M}\boldsymbol{\Phi}_k, \qquad \kappa_k = \boldsymbol{\Phi}_k^T\boldsymbol{K}\boldsymbol{\Phi}_k, \qquad f_k = \boldsymbol{\Phi}_k^T\hat{\boldsymbol{f}}, \tag{2.33}$$

for $k = 1...n$. Each of these uncoupled systems describes the amplitude of one eigenmode. These amplitudes are given by

$$\hat{r}_k = \frac{f_k}{\kappa_k}\frac{1}{1-(\omega/\omega_k)^2}, \tag{2.34}$$

where

$$\omega_k = \sqrt{\frac{\kappa_k}{\mu_k}}. \tag{2.35}$$

Thus, the particular solution is found and the response of the system is described by the sum of the complimentary and particulate solution as

$$\boldsymbol{a}(t) = \sum_{j=1}^{n} \hat{q}_j e^{i\omega_j t}\boldsymbol{\Phi}_j + \sum_{j=1}^{n} \frac{f_j}{\kappa_j} \frac{1}{1-(\omega/\omega_j)^2}\boldsymbol{\Phi}_j e^{i\omega t}. \tag{2.36}$$

2.3.3 Damping

Damping exists as viscous, frictional or other phenomena which dissipates energy from the dynamical system. One way of adding damping to a numerical system is introducing a damping matrix to the equations of motion as

$$\boldsymbol{M}\ddot{\boldsymbol{a}}(t) + \boldsymbol{C}\dot{\boldsymbol{a}}(t) + \boldsymbol{K}\boldsymbol{a}(t) = \hat{\boldsymbol{f}}e^{i\omega t}. \tag{2.37}$$

There exists multiple ways of constructing this damping matrix, each with it's assumptions and simplifications. One distinct way of dividing different damping matrices is ones that are possible to modally diagonalize and those that are not, often referred to as classical or non-classical matrices respectively. A damping matrix constructed with the help of modal damping ratios is of the classical kind [4]. A diagonalizable system is of great help when solving the numerical system, since it yields uncoupled single degree of freedom systems. This can be performed by again making the same ansatz as in (2.27), modally decomposing $\hat{\boldsymbol{a}}$ as in (2.29) and assuming that $\boldsymbol{C}$ is diagonalizable. The damped uncoupled system then takes the form

$$-\omega^2\mu_j\hat{r}_j + i\omega\gamma_j\hat{r}_j + \kappa_j\hat{r}_j = f_j, \tag{2.38}$$

where $\gamma_j = \boldsymbol{\Phi}_j^T\boldsymbol{C}\boldsymbol{\Phi}_j$, while the other quantities were introduced in (2.33). The damping ratio ζ_j, which can be acquired experimentally, is introduced as

$$\zeta_j = \frac{\gamma_j}{2\mu_j\omega_j}, \tag{2.39}$$

where ω_j was defined in (2.35). Thus

$$-\omega^2\mu_j\hat{r}_j + 2i\zeta_j\mu_j\omega_j\omega\hat{r}_j + \kappa_j\hat{r}_j = f_j, \tag{2.40}$$

which can be solved for $\hat{r}_j$ as

$$\hat{r}_j = \frac{f_j}{\omega_j^2} \frac{1}{1-(\omega/\omega_j)^2 + 2i\zeta_j(\omega/\omega_j)}, \tag{2.41}$$

to obtain the particular solution of the damped system. In case of a damped system, the transient response, or complementary solution, will be damped out and only the steady state response, or particular solution, will remain.

2.3.4 Frequency Response Function

A FRF is a transfer function expressed in the frequency domain which describes the steady state response of the system as a function of the applied harmonic force. In the automotive industry, this is typically used to gain an understanding of how the structure transmits vibrations. Specifically, from an NVH perspective, two types of FRFs are of particular interest. The vibrational velocity as a function of force, also called mobility and the acoustic pressure as a function of force. The relation shown in (2.37) can easily be described using FRFs as

$$\hat{\boldsymbol{a}} = (\boldsymbol{K} + i\omega\boldsymbol{C} - \omega^2\boldsymbol{M})^{-1}\hat{\boldsymbol{f}} = \boldsymbol{H}(\omega)\hat{\boldsymbol{f}}, \tag{2.42}$$

where the matrix $\boldsymbol{H}(\omega)$ contains these FRFs, not to be confused with the coupling matrix $\boldsymbol{H}_{s,f}$ introduced in (2.17). Every FRF in $\boldsymbol{H}(\omega)$ contains the complex vibration amplitude of one DOF when a unit load is applied in another DOF. The FRF for each of these uncoupled system in modal coordinates is

$$H_j = \frac{1}{\omega_j^2}\frac{1}{1-(\omega/\omega_j)^2 + 2i\zeta_j(\omega/\omega_j)}, \tag{2.43}$$

This specific FRF describes the displacement as a function of the force. By remembering the ansatz used when arriving at this solution, the mobility, also often called vibration transfer function (VTF), i.e. the vibration velocity as a function of force, can be acquired as

$$H_j = \frac{1}{\omega_j^2}\frac{i\omega}{1-(\omega/\omega_j)^2 + 2i\zeta_j(\omega/\omega_j)} \tag{2.44}$$

Similarly, (2.19) makes it possible to calculate the acoustic pressure for a given input force. Such an FRF is often referred to as a noise transfer function (NTF).

2.3.5 Modal Reduction

In order to further increase computational efficiency, it is possible to reduce the number of DOFs. One way of doing this is through the Rayleigh-Ritz method, where the system is assumed to be controlled by $\hat{n} < n$ approximated modes. By assuming that the lower frequency eigenmodes control the behavior of the system, one way of choosing these approximated modes is simply as a subset of the actual eigenmodes [4]. That is to say

$$\hat{\boldsymbol{a}} = \sum_{j=1}^{\hat{n}} \hat{r}_{j,\text{reduced}}\boldsymbol{\Phi}_j \quad \text{instead of} \quad \hat{\boldsymbol{a}} = \sum_{j=1}^{n} \hat{r}_j\boldsymbol{\Phi}_j. \tag{2.45}$$

Since the eigenmodes are orthogonal, the system of equations remains uncoupled and a reduced system is acquired which is less computationally intensive to solve.

2.3.6 Modal Assurance Criterion

In order to compare the similarity of eigenmodes of different models or systems, MAC is defined as

$$MAC = \frac{\mathbf{\Phi}_1^T \mathbf{\Phi}_2}{|\mathbf{\Phi}_1^T \mathbf{\Phi}_1||\mathbf{\Phi}_2^T \mathbf{\Phi}_2|}, \tag{2.46}$$

where $\mathbf{\Phi}_1$ and $\mathbf{\Phi}_2$ are the eigenmodes to be compared. A MAC-value of 1 means that the two eigenmodes are co-linear, while a value of 0 means that they are orthogonal.

2.4 Statistical Metrics

Investigating the correlation between different measures requires some way of quantifying if and how much the measures correlate. The field of statistics offer many different ways of evaluating these relationships. One way of doing this is through the use of simple linear regression. Here the relationship between a response variable y and explanatory variable x is modeled as a linear function of x as well as some disturbance ε. This takes the form as [17]

$$y_i = \beta_0 + \beta_1 x_i + \varepsilon_i, \tag{2.47}$$

where y_i, x_i and ε_i are one of the occurrences of y, x and ε respectively, while β_0 and β_1 are the coefficients of the of the linear model. In order to find an estimate of the model coefficients, a least squared approach is used where the result describes a linear function that minimizes the sum of squared residuals $\hat{\varepsilon}$. Note that $\hat{\varepsilon}$ is a part of the model and not the actual error, which is ε. Thus the coefficients are found with the use of [17]

$$\beta_1^* = \frac{\sum_{i=1}^n (x_i - \bar{x})(y_i - \bar{y})}{\sum_{i=1}^n (x_i - \bar{x})^2}, \qquad \beta_0^* = \bar{y} - \beta_1^* \bar{x}, \tag{2.48}$$

where β_0^* and β_1^* are the estimated coefficients, and $\bar{x}$ and $\bar{y}$ are the arithmetic mean of the observations. A coefficient of determination, which is used to judge how well the model fits the observations, is defined as

$$R^2 = 1 - \frac{\sum_{i=1}^n (y_i - \hat{y}_i)^2}{\sum_{i=1}^n (y_i - \bar{y})^2}, \tag{2.49}$$

where $\hat{y}_i$ is the calculated value using the model parameters.

3. Structure-Acoustic Analysis

In this chapter, the overall procedure used in the dissertation for performing the structure-acoustic analysis of a vehicle body is described. Initially, an overview of the used software solutions and their applications is given. Second, an explanation of how the different structural parts, the acoustic cavity, and their interaction are modeled is given. Finally, the procedure utilized in certain analyses is explained.

3.1 Software

In order to solve an FE problem some type of solver is needed. In this dissertation, MSC Nastran v.2014.1 is used for this purpose. MSC Nastran was initially developed for NASA in the 1960s but is now used in various industries, one of them being automotive. To use MSC Nastran, an FE representation of the system along with a file containing parameters for the solver, e.g. boundary conditions, material parameters, applied loads etc., is needed. The output received can either be in the form of text files or others prepared for use in some post-processor. Numerous different types of problems are solvable with the use of MSC Nastran. Table 3.1 shows the different types of solvers used in this dissertation as well as a description of what type of problem they are used for. MSC Nastran can be used in conjunction with AMLS, developed by CDH AG, in order to reduce the computational cost of frequency response and eigenvalue analysis. When applicable, the combined use of AMLS and MSC Nastran was utilized.

Table 3.1: MSC Nastran solvers used in the dissertation.

Solver	Description
SOL 101	Static
SOL 103	Eigenvalue problem
SOL 111	Modal frequency response

To prepare an FE model from the CAD-representation of the vehicle body for use in MSC Nastran, Ansa is used. Ansa is a pre-processing tool developed by Beta CAE Systems, generally used to convert CAD-geometry to an FE model. The models used in this dissertation were created by employees at Volvo Cars. Ansa was, however, used in the dissertation work to modify the existing models.

The results of MSC Nastran SOL 103 was visualized and analyzed using Meta, a post-processing tool also developed by Beta CAE Systems. The results from SOL 101 and 111

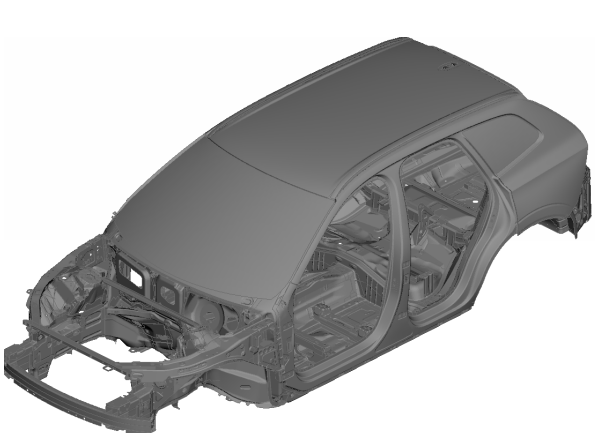

(a) BIG

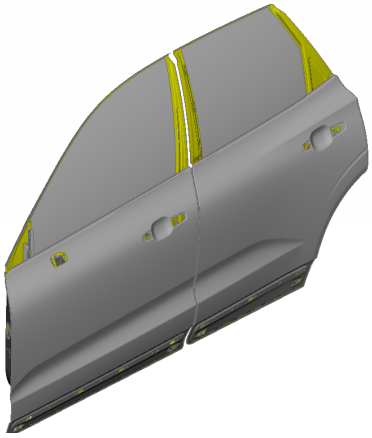

(b) Doors

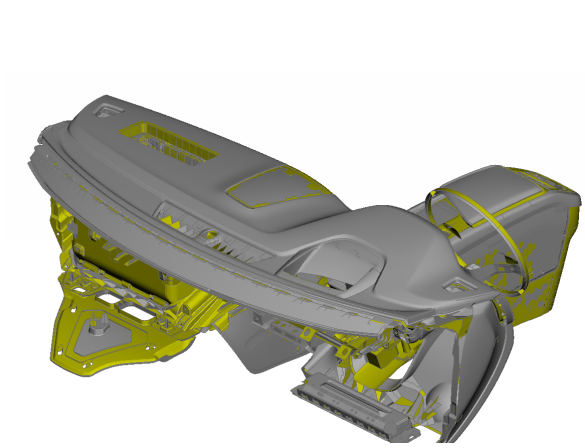

(c) Instrument panel, tunnel console and steering wheel.

(d) Seats

Figure 3.1: FE-models of some structural parts of the vehicle body. The figure shows a meshed model but the mesh size is too small to be visible.

were analyzed using Matlab. Matlab is a programming language as well as software suite, developed by MathWorks, designed to simplify matrix manipulation and scripting.

3.2 Modeling of Structural Parts

Figure 3.1 shows a selection of the FE-models of the structural parts that make up the vehicle body. The sheet metal parts, which makes up the majority of the BIG, are modeled using 4-node shell elements named CQUAD4 in MSC Nastran. This is done since sheet metal parts normally have a thickness that is small compared to the other dimensions of the part. The windscreen is modeled in a similar fashion accounting for the laminated structure. The default mesh size used is 5 mm when meshing these shell elements. This is determined by the highest eigenfrequency that is necessary to resolve. Other parts of the BIG, such as casted aluminium or molded plastic parts with complex geometry, are

modeled with 8- or 20-node solid hexahedral elements named CHEXA.

In order to connect the different parts of the BIG, a couple of different techniques are used. Welds are modeled using hexahedral solid elements between the welded parts with rigid body elements connecting the nodes of the sheet metal to that of the weld. In MSC Nastran, two kinds of rigid body elements exists. One is the rigid body element named RBE2, which is a true rigid body connection where the slave nodes follow the master. The other type, named RBE3, uses several masters and one slave node where the slave nodes follows the average displacement of the masters. For welds, RBE3 elements are used to connect the solid element of the weld with that of the sheet metal. Adhesive joints such as the attachment of the windscreen is modeled in a similar fashion, but the dimensions and material parameters of the solid elements differ.

Bolt joints are modeled using a bar element, named CBAR, in the centre of the hole. RBE2 elements connect the bar element with the nodes of the sheet metal which would be in contact with the nut or bolt head. Several other types of joints exist, but are all modeled using some combination of solid or bar elements and rigid body elements.

Larger trim items such as doors, seats, etc., are generally modeled in a similar fashion to the BIG with a couple of additions. Different types of sealings as well as some other parts are modeled using a generalized spring damper element named CBUSH. Some parts being modeled by scalar spring elements, named CELAS. If the trim item can be assumed to be co-oscillating with the BIG and the stiffness addition is small, such as for plastic interior panels, it is modeled using point masses. These point mass elements, named CONM2, are attached with rigid body elements to the surrounding structure. Finally some surface layers, such as carpets and paint, are modeled using non-structural mass (NSM). NSM is simply an increase in the density of the shell element it's applied to.

3.3 Modeling of Acoustic Cavity

Figure 3.2 shows an FE-model of the acoustic cavity. This is created by taking the vehicle body with trim items and creating a volume that is enclosed by this structure. Consequently, the acoustic cavity model contains holes where the structural trim items fit, as seen in Figure 3.2b. Special consideration is given to items such as seat cushions. While not significant enough to be modeled as a part of the structure it has impact on the acoustics of the fluid cavity. As previously mentioned, the fluid cavity contains holes for the trim items, and the seat cushions are modeled separately as heavy air. This means that the fluid that represents the cushions are given a density higher than normal air. This in order to decrease the speed of sound in the porous material. The acoustic cavity is then meshed using solid elements with sufficient mesh size to accurately represent the acoustic pressure waves at the highest frequency of interest.

The interface where the fluid is allowed to couple to the structure is defined in Ansa, while MSC Nastran performs the search algorithm for coupling the two systems at their coinciding boundaries.

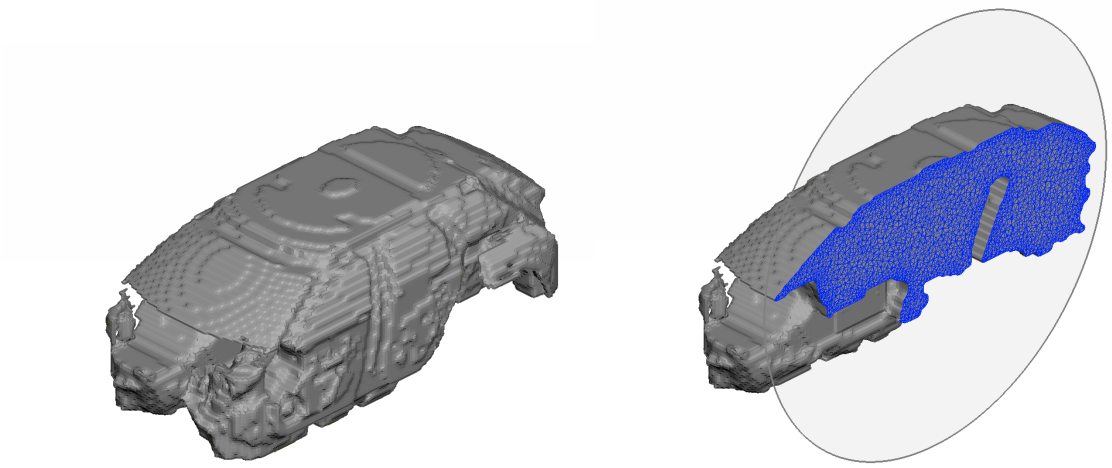

(a) (b)

Figure 3.2: FE-model of the acoustic fluid cavity.

3.4 Modal Frequency Response Analysis Procedure

Performing an analysis of a modal frequency response problem such as the ones solved by MSC Nastran SOL 111 requires the eigenmodes of the system. For a purely structural system these are calculated by solving the eigenvalue problem shown in Section 2.3. For a coupled system, the eigenmodes are calculated for the structural and fluid domain separately in a similar fashion. The system is then modally reduced using the procedure described in Section 2.3. Typically, the eigenmodes are calculated up to about twice the frequency of what the FRF is calculated to.

If an FRF for the structural mobility, i.e. a VTF, is sought, the evaluation points are simply defined somewhere on the structure in Ansa. When calculating the FRF for the acoustic pressure, i.e. an NTF, the outer ear positions at the two seats in the front and the two in the back are used as evaluation points. These four evaluation points are referred to as microphone positions in this dissertation.

When calculating the acoustic pressure response for a given input force the principle of reciprocity is used since the number of excitation points, where the load is applied, is much greater than the number of microphone positions where the pressure is calculated. Instead of applying a unit harmonic force at every excitation points and calculating the acoustic pressure, a unit acoustic source is applied at the positions of the microphones and the velocity response is calculated at the force input points. The relationship between the acoustic pressure due to an applied force is equivalent to the relationship of a velocity response due to an acoustic source as explained in [9]. Due to the linearity of the system this reciprocal approach is feasible and increases the computational efficiency.

In order to model the damping in the structure, modal damping is used. The values for the damping ratios ζ_i are based on experimental data for the structure and the fluid respectively. The damping ratios are defined in certain frequency ranges, and the eigenmodes are damped accordingly. Above a certain frequency, the damping is assumed constant. Modal damping means that the damping is applied uniformly on the com-

plete structure and the complete fluid separately and is not a characteristic of the specific material of a part.

3.5 Road Noise Calculations

Since road noise, i.e. the noise coming from the interaction between the vehicle and the road surface, is considered in the dissertation, the loads acting on the vehicle body from this interaction needs to be acquired. Such loads are available for the vehicle bodies investigated in the dissertation as they have been previously determined by employees at Volvo Cars. The procedure to determine the forces follows the one described in [3, 16], and is explained briefly here since those forces are used in the dissertation.

The dynamic forces acting on a vehicle body, induced by road excitations, depend on the interaction between road, tyres, chassis' components and vehicle body. In order to calculate these forces, the different cars are driven around a test track with multiple accelerometers attached at the knuckle, a part of the wheel suspension. From these accelerations, an equivalent force acting at the interface between the wheel and the wheel suspension is calculated using an FRF acquired from the FE-model of the chassis. This equivalent force is then used to, by using a FE-model of the complete vehicle, calculate the forces acting on the interface between the chassis and the vehicle body.

Using this road induced force, it is possible to calculate the road noise level at the microphone positions. This is done by multiplying each NTF of the trimmed vehicle body, acquired by the use of the procedure described in Section 3.4, with the force acting on the corresponding point of the vehicle body. As a part of the post-processing steps, the NTFs are given as the magnitude of the complex amplitude. Because of this the pressure level at a microphone position is calculated as a root of sum of squares [10], as they can be considered uncorrelated sources, as

$$P_{\text{Mic: }1}(f) = \sqrt{\sum_{n=1}^{N} \sum_{m=x,y,z} (F_{n,m}(f) \;\; NTF_{n,m\rightarrow,\text{ Mic: }1}(f))^2} \tag{3.1}$$

where $F_{n,m}(f)$ is the force, applied at point n direction m as a function of frequency, $NTF_{n,m\rightarrow,\text{ Mic: }1}(f)$ is the NTF from point n direction m for microphone one. This yields the pressure level for one microphone as a function of frequency. Figure 3.3 shows a graphical representation of the quantities used in (3.1).

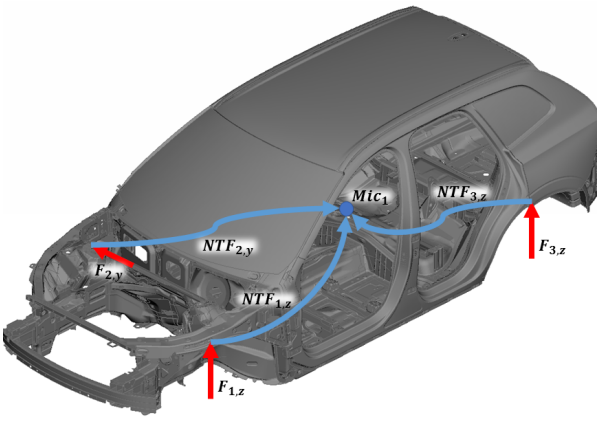

Figure 3.3: Schematic of road-induced forces acting on a vehicle body, and the NTFs from the forces to the sound pressure at the driver's ear position.

4. Evaluation of NVH Performance

In order to judge the overall NVH performance of the final vehicle body, a suitable measure was developed. The term "final vehicle body" refers the BIG with trim items, such as doors, seats, steering column, instrument panel etc. included. In the chapter, the procedure used to acquire this measure is described. Since the thesis work focuses on the NVH performance in terms of road noise, a road noise index was used to judge the performance.

4.1 Dynamic Forces Acting on a Vehicle Body

The road noise is possible to calculate using the procedure described in Section 3.5 for every individual car. When comparing different car bodies to each other, the same loads should be applied in order to make a fair comparison. Thus, it was investigated whether it was reasonable to replace the individual car loads with a set of common loads. These common loads would be the average of the loads for the different cars. A requirement, for this to be reasonable, would be that no individual car would differ greatly from the others. If the loads differ significantly, among the cars, unit forces would be the most appropriate choice instead.

The road loads of the cars specified in Table 1.1 was collected. The load data files, 12 in total, were only available for the ICE cars. Some cars shared the same load files and some cars had multiple load files. When the forces at the specified points of the vehicle body is calculated, the phase angle is disregarded and the forces are given as the magnitude of the complex amplitude. To compare the different forces, an arithmetic mean was calculated for the frequency bands shown in Table 1.2, as

$$\bar{F} = \frac{1}{n} \sum_{i=\omega_1}^{\omega_2} F(i), \tag{4.1}$$

where $\bar{F}$ is the arithmetic mean of one frequency band, $F(i)$ is the calculated force at the angular frequency ω_i, and ω_1 and ω_2 are the frequency limits. A schematic view of the mean value calculation is shown in Figure 4.1. Note that a root mean square could have been used instead. Since the forces are strictly positive, the only difference would be in how outliers affect the value. The averages were calculated for every load point and every direction (x, y and z) for each of the different load files.

The data was compiled and compared both intra- and inter car-wise in order to identify common important load points and directions. A comparison of the first five points is shown in Tables 4.1–4.3, where the forces have been normalized with respect to the largest

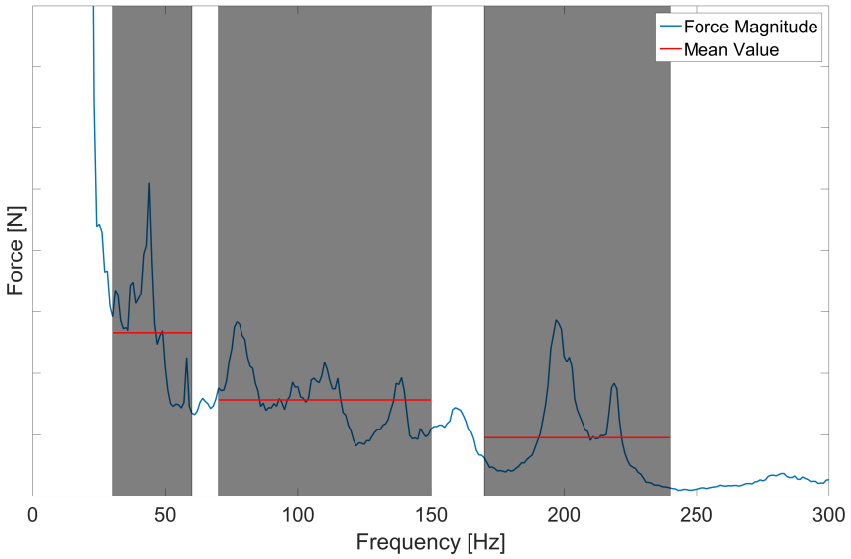

Figure 4.1: Example of a road-induced force as a function of frequency, with calculated arithmetic mean for three frequency bands.

calculated mean for each band. For a complete view of the data, see Appendix A. The mean force value across all the investigated cars was calculated as

$$\bar{F} = \frac{1}{n} \sum_{i=1}^{n} \bar{F}_{car,i} \tag{4.2}$$

where $\bar{F}$ is the arithmetic mean across the cars, $\bar{F}_{car,i}$ is the arithmetic mean of one of the cars in one frequency band, and n is the total number of cars. The mean across cars is shown as a shaded column in Tables 4.1–4.3. By inspecting Tables 4.1–4.3, it is found that it is possible to identify common important load points and directions for the vehicles in the analyzed frequency bands. These mean value were then discretized and assigned a value of 0, 0.5 or 1 by rounding the mean value across the cars. The discretized value is used in the calculation of the road noise index.

Table 4.1: Averages of road induced forces on different Volvo cars in the drumming frequency band (30–60 Hz) for the first five load points. The forces are normalized to a largest value of 1. For all points see Appendix A.

Point #	Direction	Discretized Value	Mean	Car #	Car #	Car #	Car #
001	x	0.5	0.4	0.5	0.3	0.4	0.3
001	y	0	0.2	0.3	0.2	0.3	0.2
001	z	0	0.2	0.3	0.2	0.2	0.2
002	x	0.5	0.5	0.6	0.3	0.6	0.3
002	y	1	0.9	0.9	0.6	1	0.9
002	z	0	0.2	0.3	0.2	0.3	0.2
003	x	0	0.2	0.2	0.2	0.2	0.1
003	y	0.5	0.6	0.7	0.5	0.6	0.5
003	z	0	0.1	0.1	0.1	0.1	0.1
004	x	0	0.2	0.2	0.1	0.2	0.1
004	y	0.5	0.5	0.6	0.4	0.5	0.4
004	z	0	0.1	0.1	0.1	0.1	0.1
005	x	0	0.2	0.2	0.2	0.2	0.1
005	y	0	0.2	0.2	0.2	0.2	0.2
005	z	0.5	0.7	0.7	0.7	0.7	0.5

Table 4.2: Averages of road induced forces on different Volvo cars in the rumble frequency band (70–150 Hz) for the first five load points. The forces are normalized to a largest value of 1. For all points see Appendix A.

Point #	Direction	Discretized Value	Mean	Car #	Car #	Car #	Car #
001	x	0.5	0.5	0.5	0.5	0.5	0.4
001	y	0.5	0.3	0.3	0.3	0.3	0.3
001	z	0.5	0.3	0.4	0.3	0.3	0.3
002	x	0.5	0.4	0.5	0.3	0.5	0.5
002	y	1	1	1	1	1	1
002	z	0.5	0.5	0.5	0.4	0.5	0.4
003	x	0.5	0.3	0.3	0.3	0.3	0.3
003	y	0.5	0.6	0.6	0.6	0.6	0.7
003	z	0	0.1	0.1	0.1	0.1	0.1
004	x	0.5	0.3	0.2	0.3	0.3	0.3
004	y	0.5	0.6	0.5	0.7	0.5	0.6
004	z	0	0.1	0.1	0.1	0.1	0.1
005	x	0	0.1	0.1	0.2	0.1	0.1
005	y	0	0.1	0.1	0.1	0.1	0.1
005	z	0.5	0.3	0.3	0.3	0.3	0.3

Table 4.3: Averages of road induced forces on different Volvo cars in the tyre cavity frequency band (170–240 Hz) for the first five load points. The forces are normalized to a largest value of 1. For all points see Appendix A.

Point #	Direction	Discretized Value	Mean	Car #	Car #	Car #	Car #
001	x	1	0.9	0.9	1	0.7	0.8
001	y	0.5	0.3	0.3	0.3	0.2	0.3
001	z	0.5	0.5	0.4	0.6	0.5	0.5
002	x	0.5	0.7	0.6	0.7	0.7	0.6
002	y	0.5	0.7	0.8	0.6	0.7	0.8
002	z	0.5	0.6	0.7	0.5	0.8	0.5
003	x	0	0.1	0.1	0.2	0.1	0.2
003	y	0.5	0.3	0.2	0.3	0.3	0.4
003	z	0	0.1	0.1	0.1	0.1	0.1
004	x	0	0.1	0.1	0.2	0.1	0.2
004	y	0.5	0.3	0.3	0.4	0.3	0.4
004	z	0	0.1	0.1	0.1	0.1	0.1
005	x	0	0.2	0.2	0.2	0.2	0.2
005	y	0	0.1	0.1	0.1	0.1	0.1
005	z	0.5	0.4	0.4	0.4	0.5	0.4

4.2 Road Noise Index

In order to compare the different cars a road noise index was created. The purpose of this road noise index was to portray the broad-band NVH-performance of a vehicle body, with trim items, subjected to a road load.

The narrow-band acoustic pressure was calculated using the procedure described in Section 3.5 and the discretized forces shown in Section 4.1. This yields the pressure level for one microphone as a function of frequency. The pressure level for a larger frequency band is calculated in a similar way as [2]

$$P_{\text{Broadband}} = \sqrt{\sum_{n=1}^{N} P^2_{\text{Narrowband, } n}}$$

This results in 12 different broadband pressures, one for each of the microphones and frequency bands, shown in Table 1.2. The road noise index in one frequency band is calculated as the arithmetic mean of the four microphone pressures in each frequency band. The road noise index is used as the measure of the NVH performance of the final vehicle body for all the comparisons. The road noise index is an index and not a measurable sound pressure level. For comparison, the road noise index was also calculated using unit loads, instead of the discretized forces.

5. Early Prediction Measures

Three different objective measures usable in the concept development phase were evaluated. As a representation of the vehicle body, in the concept development phase, the BIG was chosen as seen in Figure 5.1a. Thus, no information of the different trim items are needed, which generally are designed in later stages. In the chapter, the procedure for calculating these measures are described. Throughout the chapter, a schematic view of the BIG is used to describe locations of different points. Figure 5.1 shows a comparison of the BIG and this schematic view, to show how points on the schematic view correspond to the same points on the BIG.

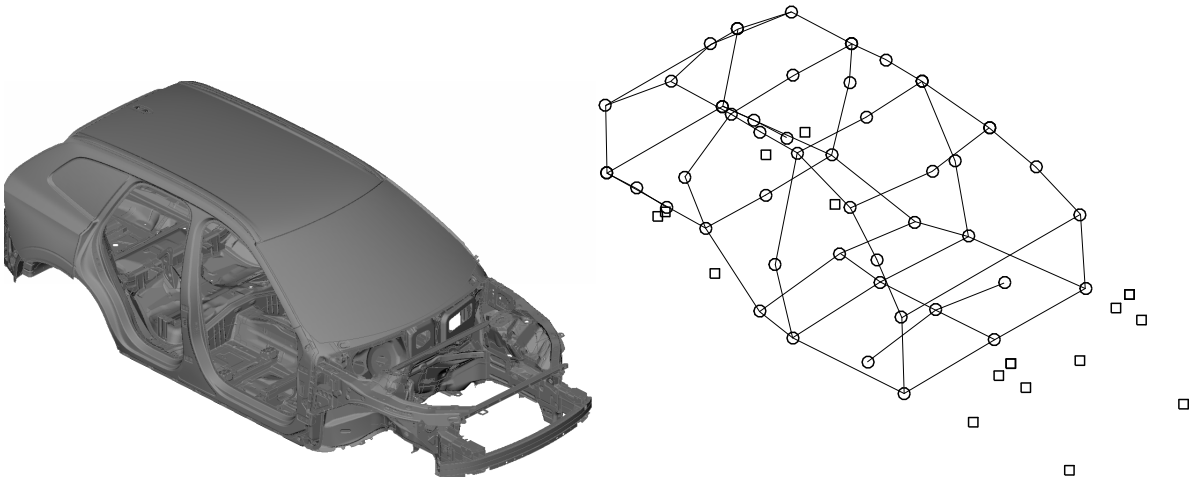

(a) BIG (b) Schematic view of the BIG.

Figure 5.1: A comparison of the BIG and the schematic view of the BIG.

5.1 Eigenfrequencies

Eigenfrequencies of certain BIG modes are often calculated during the different stages of automotive development since they are related to several vehicle attributes. Using global first order bending and torsional modes to evaluate vehicle body performance was investigated in [12, 20]. From an NVH point of view it is of interest to evaluate whether the eigenfrequencies are reflective of the overall NVH performance of the body and the complete vehicle.

The first global modes of the vehicle bodies were investigated. The modes up to 100 Hz of the bodies, acquired using MSC Nastran SOL 103, were examined visually. Three types of modes were selected for analysis. The first mode type was torsion around the longitudinal axis, which in the dissertation is named the *Torsion* mode. The second mode type was bending around the vertical axis, named *Yaw*. For higher cars, this mode exhibited a shearing motion at the top rear, why it often is called a parallelogram- or prairie wagon-mode in the automotive industry. The third mode type was bending around the transversal axis, which is named *Bending*. The bending mode exhibited a pumping behaviour, where the roof and floor were oscillating out of phase.

A complex geometrical shape such as the vehicle body has equally convoluted eigenmodes, and none of the modes are pure first order bending or torsional modes. Because of this, it was analyzed which of the modes that were global, in a sense that they controlled the global behavior of the vehicle body, and that eigenmodes from the different vehicles were compared to ensure that they represent the same type of deflection shape.

The globality of the eigenmodes were judged visually, as well as with the help of a tool available in Meta version 17.1.3. The tool is called "Identify Global-Local Modes" and accepts two inputs. The first input is a criterion set from 1–100 where a value of 100 means that the mode is considered as global if it affects all grid points of a structure, this value was set to 95. The second input being a coefficient which the max displacement of a mode is multiplied with, this was left at the default value of 0.01. Initially, the modes were inspected visually and grouped into the three different types. Second, the Meta tool was used to extract the global modes. The eigenmodes that were considered global both by visual inspection and the Meta tool were chosen for further examination.

In order to ensure that the modes from different vehicles were representing the same type of deflection shape, the chosen modes were compared using MAC-values, which are defined in (2.46).

Since different cars have different geometries, the MAC-value could not be computed for the entire structure. Instead, 18 points were selected to represent the vehicles. The points were distributed throughout the lower body and on points which were assumed to describe the global behavior of the body, such as beams or attachment points to the chassis. The reason for choosing points on the lower part of the body was twofold. First, the structure in the lower body is generally more robust due to safety requirements and load bearing capabilities among other, and therefore more important for the global behavior compared to the upper body. Second, the structure in the lower body is determined earlier in the development cycle and is therefore more usable in an early concept phase when the structure in the upper body might still be largely undetermined. Figure 5.2 shows the placement of the points used in the calculation of MAC-values.

The *Yaw*, *Torsion* and *Bending* modes of the investigated vehicle bodies, as seen in Table 1.1, were compared, and the modes resulting in the best overall MAC-values among the different bodies were selected for the evaluation of eigenfrequencies. That is to say that the selection of eigenmodes from the earlier selection was reduced to three, one of each type, for every vehicle. These eigenfrequencies were investigated as a measure of the BIG in the early concept phase.

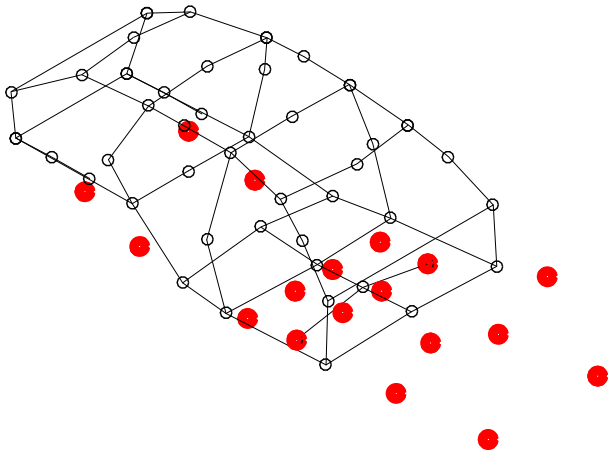

Figure 5.2: Placement of the points used in the calculation of the MAC shown in red.

5.2 Global Stiffness

The global stiffness of the vehicle body is, for certain load cases, often calculated and reported throughout the development stages as since it is related to several vehicle attributes. Because of this, it is of interest to evaluate whether this currently used measure is reflective of the overall NVH performance of the body.

The stiffness was evaluated according to a standard procedure used at Volvo Cars, also used by [8, 19]. The use of global bending and torsional stiffness for evaluating vehicle body performance was investigated by [12, 20]. In general, the body is constrained in a manner to ensure a statically determined system and a static load is applied to trigger global deformations. The deflections are calculated at certain evaluation points assumed to represent the global deformation of the body. The stiffness is subsequently calculated as

$$K = \frac{F}{u},$$

where K is the global stiffness, F is the applied load and u is the measured deflection. The static deflections are acquired by using MSC Nastran SOL 101.

5.2.1 Torsional Stiffness

The torsional stiffness is calculated by constraining the rear left damper attachment point in the x-,y- and z-direction and the rear right damper attachment point in the z-direction. Also, the frontmost point of the body was constrained in order to prevent the system from becoming a mechanism. A force couple is applied at the front left and right damper towers to provide a moment at the front section of the body. The deflection is evaluated at points below the damper towers, along the vertical axis, but at the same longitudinal position as the point where the load is applied. The deflection evaluation points were chosen to minimize the influence of the local stiffness of the damper towers. The positions of the constraints, the loads as well as the evaluation points are shown in Figure 5.3.

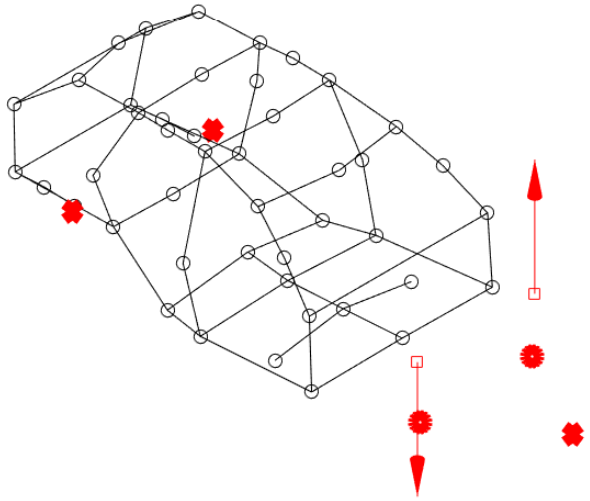

Figure 5.3: Placement of the points used in the calculation of the torsional stiffness shown in red. The points where the boundary conditions are applied are shown as crosses, the forces are applied as squares and where the displacements are evaluated as circles.

The stiffness K is then calculated as

$$K = \frac{M}{\varphi},$$

where M is the applied moment and φ is the deflection angle, which is calculated as

$$\begin{aligned} M &= FL_{load}, \\ \varphi &= (-D_{z,lhs} + -D_{z,rhs})L_{eval}, \end{aligned}$$

where F is the applied load which for all simulations was a unit load, L_{load} is the transversal distance between the two points where the load is applied, $D_{z,lhs}$ and $D_{z,rhs}$ are the vertical displacements on the left hand side and right hand side, respectively, and L_{eval} is the transversal distance between the two evaluation points.

5.2.2 Bending Stiffness

Calculating the bending stiffness is done by constraining the rear left damper attachment point in the x-,y- and z-direction, the rear right damper attachment point in the z-direction, the front left damper attachment point in the y- and z-direction and the front right damper attachment point in the z-direction. Two point forces are applied to points centered and connected, via a rigid element, to the front seat attachment points, i.e. one load is applied to the left front seat attachments and one to the right front seat attachments. The deflection is evaluated at five points along the tunnel. The positions of the constraints, the loads as well as the evaluation points are shown in Figure 5.4.

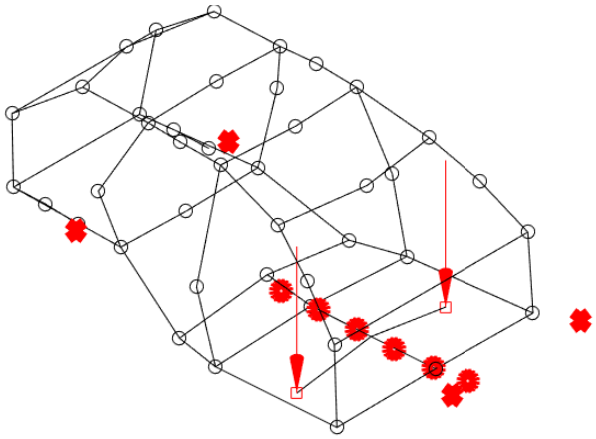

Figure 5.4: Placement of the points used in the calculation of the bending stiffness shown in red. The points where the boundary conditions are applied are shown as crosses, the forces are applied as squares and where the displacements are evaluated as circles.

The stiffness K is then calculated as

$$K = \frac{2F}{D_{z,mean}},$$

where F is the applied force, which for all simulations was a unit load, and $D_{z,mean}$ is the mean vertical deflection of these five evaluation points along the tunnel. The reason for using the arithmetic to minimize he influence of differences in local response between the cars.

5.3 Mobilities

The third type of early prediction measure investigated in the dissertation is mobility transfer functions in the BIG, i.e. the velocity response due to loading in the attachment points between vehicle body and chassis. When calculating the vibrational velocities in the structure no information is needed about the fluid in the cavity of the body which greatly simplifies the procedure. If the evaluation points for the velocity response are chosen on large structural members such as beams and pillars, the usefulness in early concept phases is further increased because the properties of these are defined earlier than those of the panels, which also are part of the body. The shape of the panels might change late in the development, for example by adding different embossings and damping materials. Another reason for evaluating the vibrational velocities at the structural members is the assumption that vibrations from these members will be transferred to the panels, which are the main sources of sound radiation. The velocity FRFs are often called mobilities,

and are traditionally divided into two different kinds. The first kind being point mobilities, where the response is calculated for the same degree of freedom as the load is applied in. Such FRFs give a representation of how much vibration energy that enters the system. The second kind is transfer mobilities, where the response is calculated at some other point in the structure, such as he main structural members as discussed above. This is a measure of how the vibrations are transferred throughout the system.

In a similar way to how the road noise index is calculated, see Chapter 4, the vibration transfer function at certain points were used to calculate a mobility index as a measure usable in the early concept phase. For the sedan cars, described in Table 1.1, 42 points were defined to which the mobilities was calculated, for the estates and SUVs 45 points were defined, this because of the extra structural beams at the rear of the vehicle. These points were spread throughout the beam structure that makes up the body. In general, the points were located at joints between major beam structures and on the midpoints of the beams. Consideration was also taken to ensure that the points were located on locally stiff parts, such as, positions where multiple sheets of metal overlap, or positions close to welds. The mobilities were calculated from the same load points used in the calculation of the road noise index, see Chapter 4. Figure 5.5 shows the distribution of the load and evaluation points across the BIG.

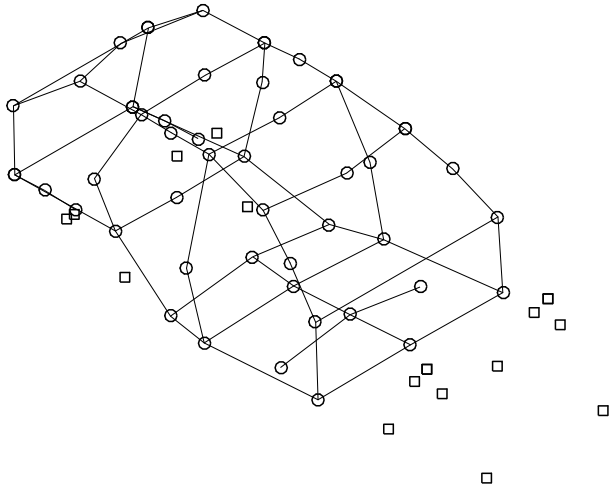

Figure 5.5: Positions of the points used for the evaluation of mobilities, shown as circles. The black squares show the positions where the loads are applied.

The mobilities are acquired using MSC Nastran SOL 111 and converted to a format usable in Matlab, where the magnitude of the complex amplitude of the mobilities were used to calculate the mobility index. The velocity at a certain evaluation point and direction, caused by the road-induced forces, is calculated as a root of sum of squares similar to (3.1) as.

$$V_{p,q}(f) = \sqrt{\sum_{n=1}^{N} \sum_{m=x,y,z} \left(F_{n,m}(f)\ VTF_{n,m\rightarrow p,q}(f)\right)^2}. \tag{5.1}$$

where $V_{p,q}(f)$ is the velocity in point p, direction q , as a function of frequency, $F_{n,m}(f)$ is

the force applied in point n, direction m, as a function of frequency, and $VTF_{n,m\to p,q}(f)$ is the mobility for a load applied in point n, direction m, and velocity response in point p, direction q. This yields the velocity in each point and direction as a function of frequency. The magnitude of the velocity in each specific point is calculated as

$$V_p(f) = \sqrt{\sum_{q=x,y,z} V_{p,q}(f)^2}.$$

The velocity magnitude for a larger frequency band is calculated again using a root of sum of squares

$$V_{\text{Broadband}}(f) = \sqrt{\sum_{n=1}^{N} V_{\text{Narrowband, }n}(f)^2}.$$

The mobility index is then calculated as the arithmetic mean of the broadband velocities for the evaluation points. Thus, the mobility index can be calculated for all, or some subset, of the evaluation points.

For the specific case where the vibration velocities is evaluated at the same points as the load is applied (5.1) changes slightly to

$$V_{p,q}(f) = \sqrt{\left(F_{p,q}(f)\ \ VTF_{p,q\to p,q}(f)\right)^2}.$$

This specific type of mobility index is called point mobility index. The mobility index was calculated using two sets of forces: the discretized forces described in Chapter 4 and unit forces.

6. Survey of Current Vehicles

The early measures, described in Chapter 5, and the road noise index, described in Chapter 4, were calculated using the models of the cars shown in Table 1.1 for the frequency bands shown in Table 1.2. The early measures were calculated using a model of the BIG, while the road noise index was calculated using a model of the BIG with all trim items included. For the PHEV vehicles the measures was calculated both with and without the battery. In the results only the values where the battery is included are shown. The reason for this was twofold. First the battery is an integral part of the body and the overall structure of the BIG is from the start designed with a specific battery in mind, the battery in itself adds significant mass and stiffness to the structure. Secondly including the battery gave values more in line with that of the ICE vehicles, excluding it gave significant outliers. Note that the road noise index and mobility index are not normalized to the width of the frequency bands. Therefore, it is not possible to compare the mobility or road noise indices between the different frequency bands to draw any conclusions regarding their relative levels. Additionally, a simple linear regression model was calculated using the procedure described in Section 2.4. For the datasets resulting in an R^2 value of above 0.25, the line representing the regression model is included in the plot. The minimal allowable R^2 value was set as low as 0.25 in order to visualize tendencies of correlation, and not to construct an accurate model used for predicting noise. Note that the datasets only contain nine points each, which emphasizes that caution should be exercised when analyzing the linear regression model.

6.1 Eigenfrequencies

The procedure for selecting global eigenmodes described in Chapter 5 was applied to the BIGs of the nine car models. The MAC-values for the selected modes are shown in Figure 6.1–6.3. For the PHEV-vehicles, the MAC-values were calculated for the BIG both with and without the battery included in the model. In the figures, this is indicated as "No Battery" for the models where the battery was excluded.

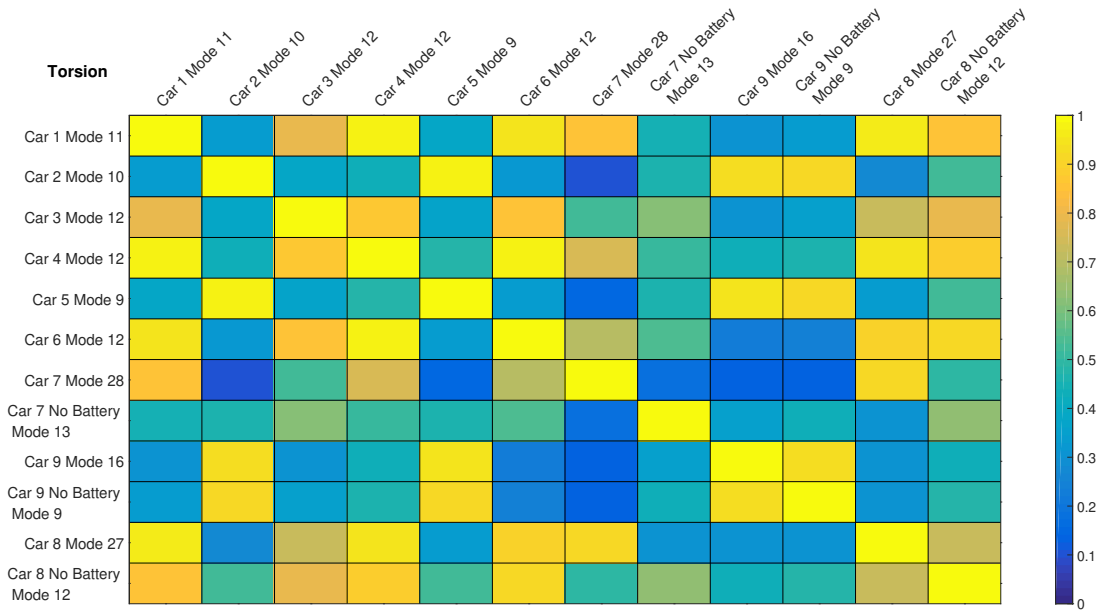

Figure 6.1: MAC-values for the BIG *Torsion* modes of the vehicles analyzed in the survey.

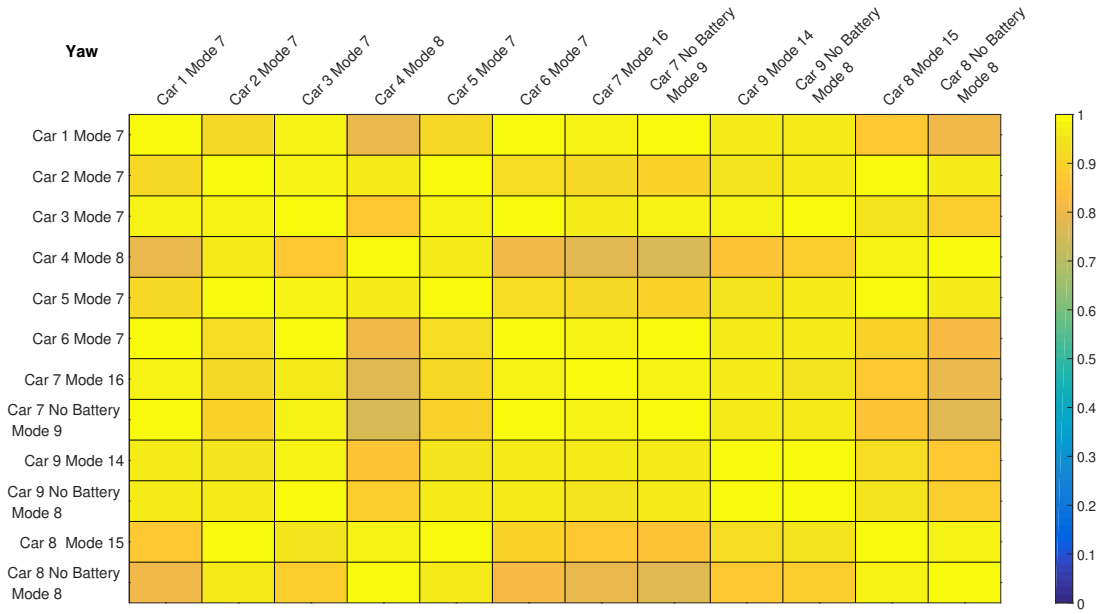

Figure 6.2: MAC-values for the BIG *Yaw* modes of the vehicles analyzed in the survey.

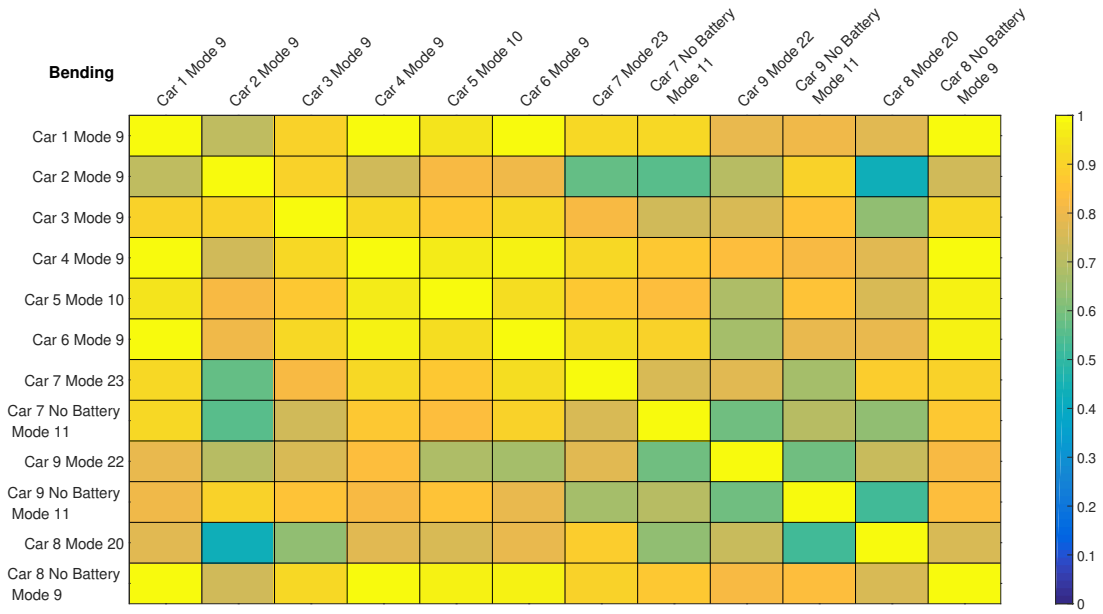

Figure 6.3: MAC-values for the BIG *Bending* modes of the vehicles analyzed in the survey.

It can be seen that the MAC-values for the *Torsion* modes are rather poor. By consulting Table 1.1 it is evident that this discrepancy is between the sedans and the other cars. That is to say that the *Torsion* modes are quite similar among the sedans, the same can be said among the estate and SUVs. Because of this, the sedans are separated from the dataset of all nine cars when calculating the linear regression model for the *Torsion* modes. Some discrepancy can also be seen for the *Bending* modes of the PHEVs compared to the ICE-cars. The *Yaw* modes exhibit good MAC-values for all cars.

The comparison of the eigenfrequencies as an early measure and the road noise index, for the frequency bands used in the dissertation, is shown in Figure 6.4. By inspecting Figure 6.4, a tendency of higher eigenfrequency for the *Bending* modes leading to higher road noise index in the drumming and rumble frequency band is discernable.

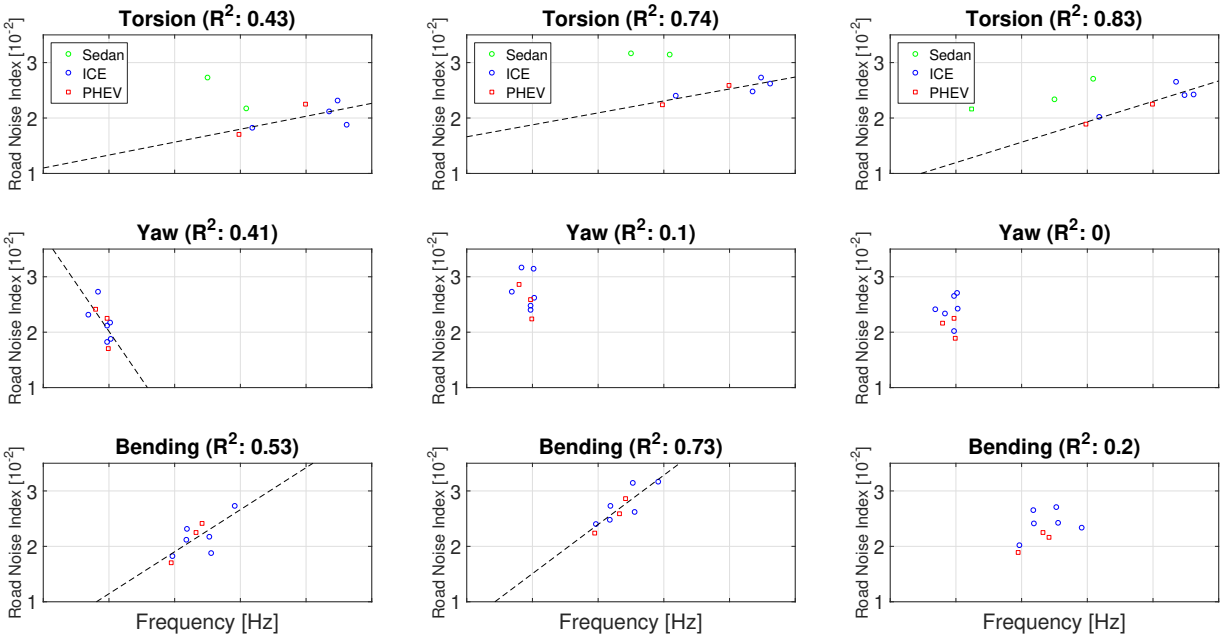

(a) Drumming: 30–60 Hz (b) Rumble: 70–150 Hz (c) Tire Cavity: 170–240 Hz

Figure 6.4: The eigenfrequencies of the BIG eigenmodes and the road noise index in the different frequency bands. The dotted line is the linear approximation acquired by use of linear regression, shown for datasets with $R^2 > 0.25$. The x-axis grid spacing is 5 Hz.

6.2 Stiffness

The comparison of the global stiffness of the BIG as an early measure and the road noise index, for the frequency bands used in the dissertation, is shown in Figure 6.5. In the results, it is possible to see a tendency that higher bending stiffness results in lower road noise index in the drumming frequency band, which is the opposite of what is indicated by the eigenfrequencies. The correlation in the other frequency bands is poor.

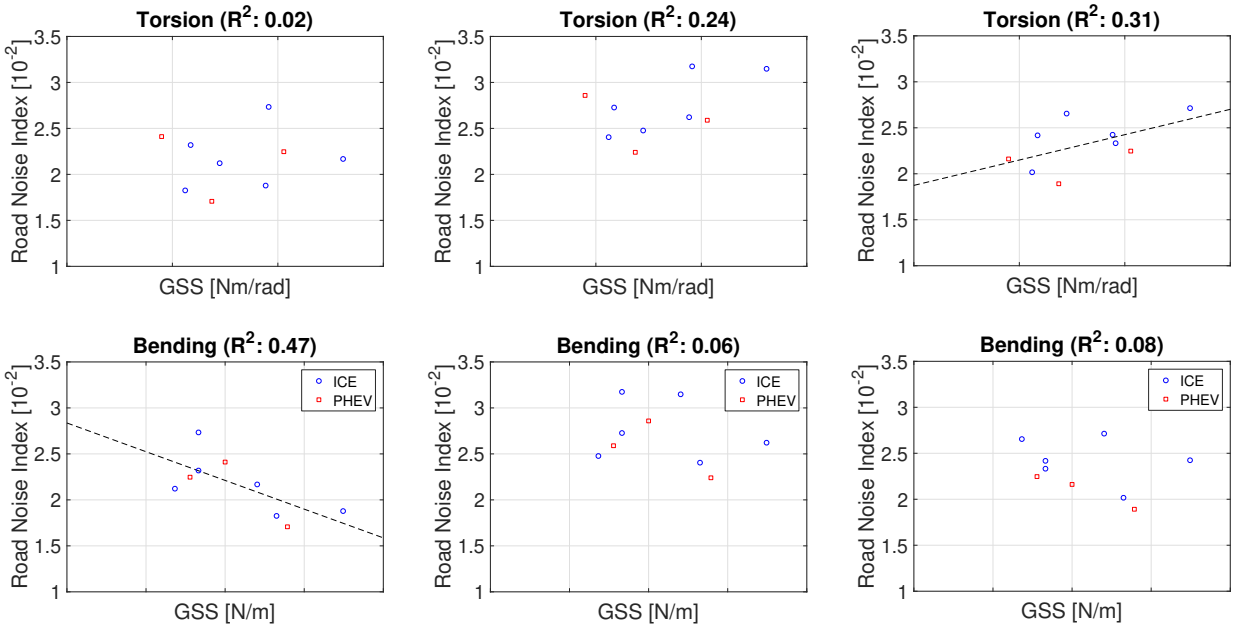

(a) Drumming: 30–60 Hz (b) Rumble: 70–150 Hz (c) Tire Cavity: 170–240 Hz

Figure 6.5: The global stiffness and the road noise index in the different frequency bands. The dotted line is the linear approximation acquired by use of linear regression, shown for datasets with $R^2 > 0.25$. The x-axis grid spacing is $1 * 10^5$ Nm/rad and $5 * 10^5$ N/m for the top and bottom row of plots, respectively.

6.3 Mobilities

The comparison of the mobility index of the BIG as an early measure and the road noise index, for some subsets of evaluation points in the frequency bands used in the dissertation, is shown in Figures 6.6 and 6.8. Figure 6.6 shows the mobility index, calculated using all common evaluation points. Figure 6.8 shows the point mobility index, calculated using the load points. For a complete view of all the evaluated subsets, see Appendix B. A figure showing the evaluation points used for the different result plots are included after each plot figure, both in this chapter and in Appendix B. In Figure 6.6, a tendency of correlation between the mobility index and the road noise index is seen in the rumble and tyre cavity frequency bands. The same can be observed in Figure 6.8 for the point mobility index in all of the frequency bands.

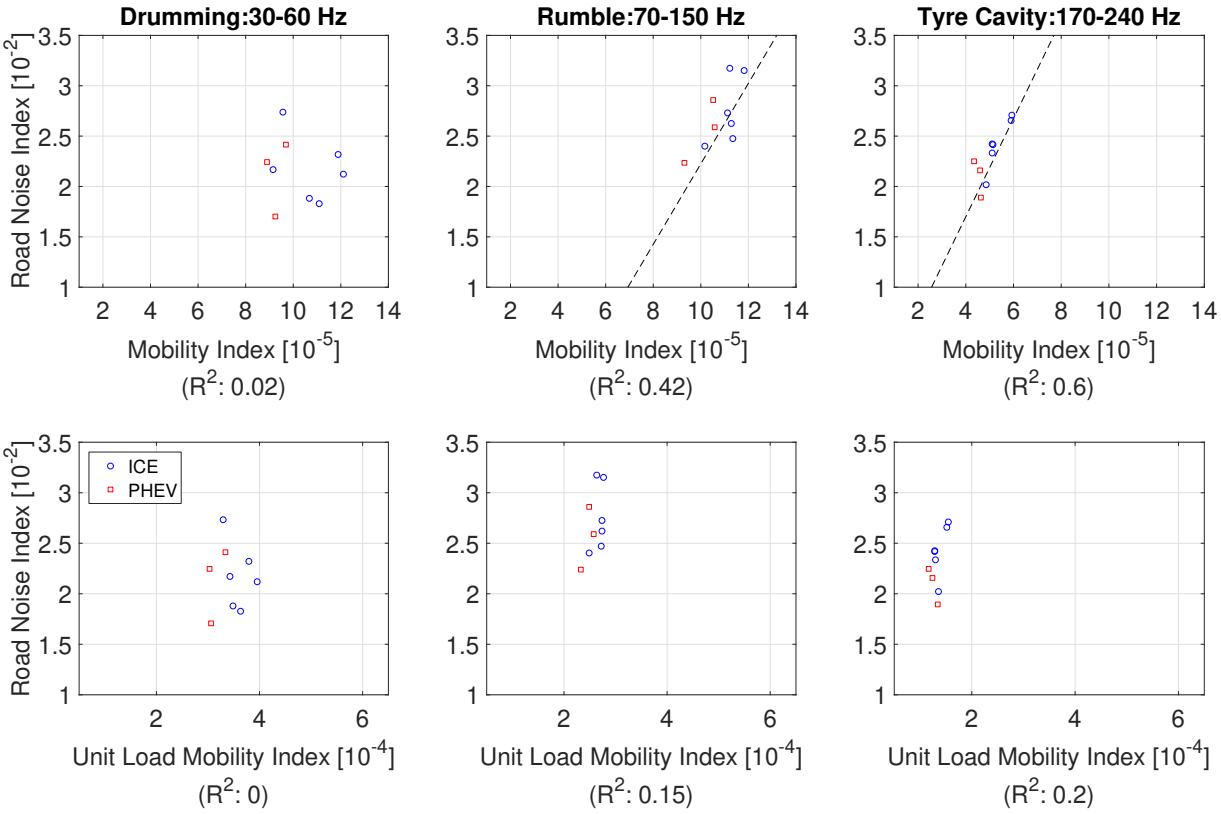

Figure 6.6: The mobility index of the BIG, calculated both using the road-induced forces described in Chapter 4 (top row) and a unit load (bottom row), and the road noise index. The mobility index is calculated using the evaluation points highlighted in Figure 6.7. The dotted line is the linear approximation acquired by use of linear regression, shown for datasets with $R^2 > 0.25$.

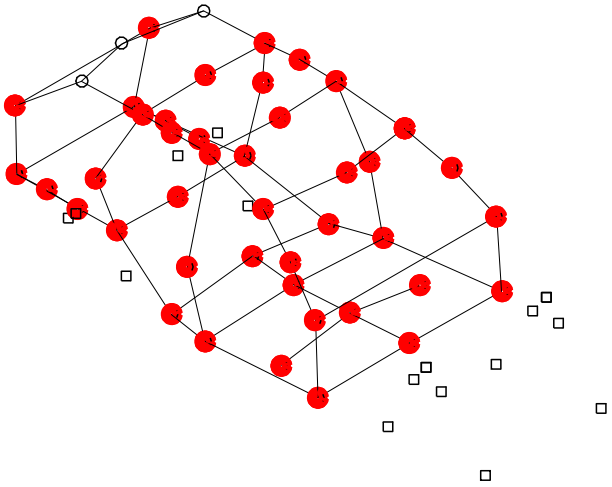

Figure 6.7: Highlighted points show the evaluation points used for the result plots in Figure 6.6. These points are all the points that the nine cars have in common.

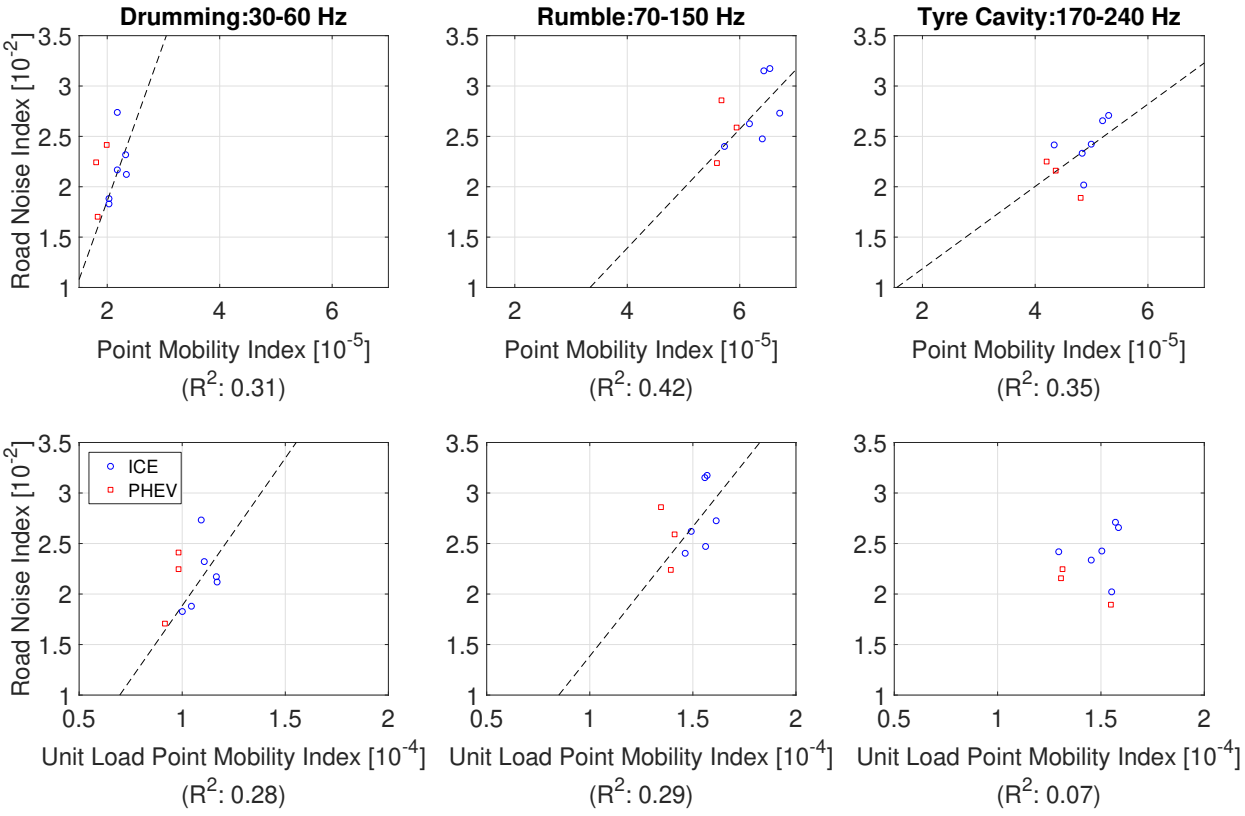

Figure 6.8: The point mobility index of the BIG, calculated both using the road-induced forces described in Chapter 4 (top row) and a unit load (bottom row), and the road noise index. The point mobility index is calculated using the evaluation points highlighted in Figure 6.9. The dotted line is the linear approximation acquired by use of linear regression, shown for datasets with $R^2 > 0.25$.

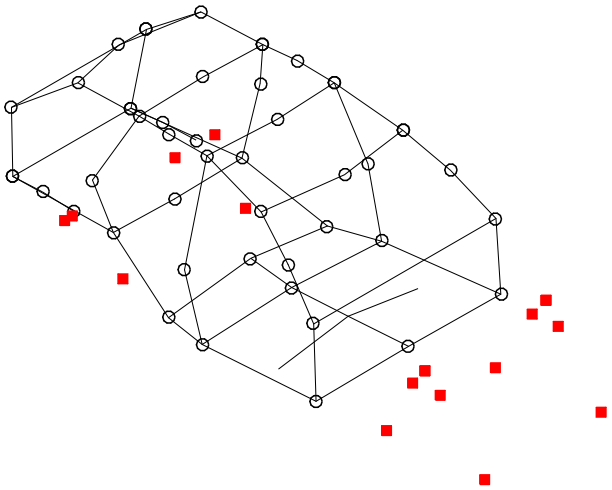

Figure 6.9: Highlighted points show the evaluation points used for the result plots in Figure 6.8. These points are the load points.

7. Case Study

The survey of different vehicles presented in Chapter 6 was performed for a relatively small set of vehicles, including both sedans, SUVs and estates. In order to evaluate the early measures for an increased amount of data points, and thereby increase the statistical basis of the metrics used, a case study was performed. A single car, number 1 from Table 1.1, was chosen for the analyses. In order to create a set of modified BIGs, the material properties of the BIG were modified, which in turn affects the early measures as well as the road noise index. As the dissertation aims to investigate the correlation of measures usable in an early concept phase, where the beam structure of the BIG is defined, the changes were performed only on the beam structure. Figure 7.1 shows the BIG and the corresponding beam structure. This beams structure was divided into seven sets, on which the changes were performed. Figure 7.2 shows the seven sets that the beam structure was divided into. The density (ρ) and young's modulus (E) of these sets were altered in order to mimic a design change to the structure. The sets consist only of parts that are made of some type of steel. Parts made of other materials were excluded in order to simplify the work necessary to perform the case study. In reality, multiple kinds of steel are used in the beam structure of the BIG, but to further simplify the work, a singular kind of steel was used in the case study. Hence, all sets had the same baseline properties, which can be seen in Table 7.1.

In order to find realistic ranges for the variation in material parameters, an iterative procedure was conducted. The parameters were altered individually to a degree that

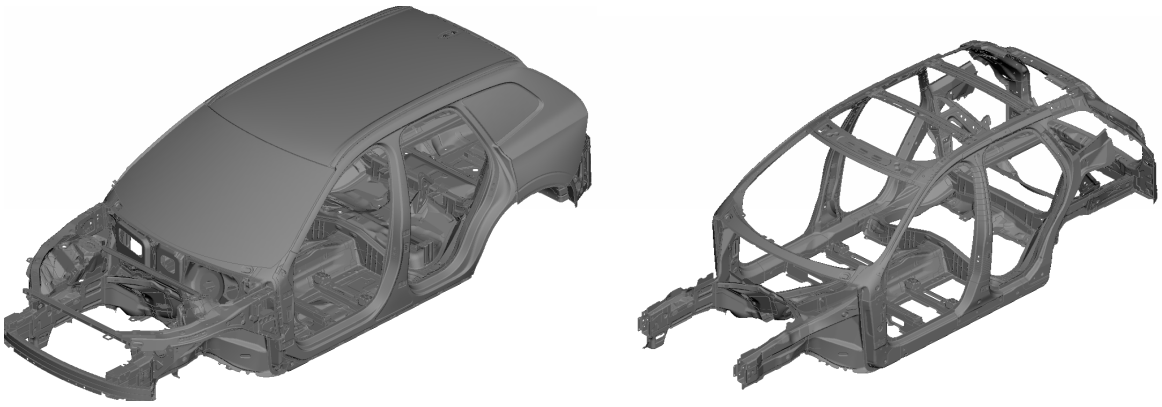

(a) BIG (b) Beam strucure.

Figure 7.1: BIG and the beam structure investigated in the case study.

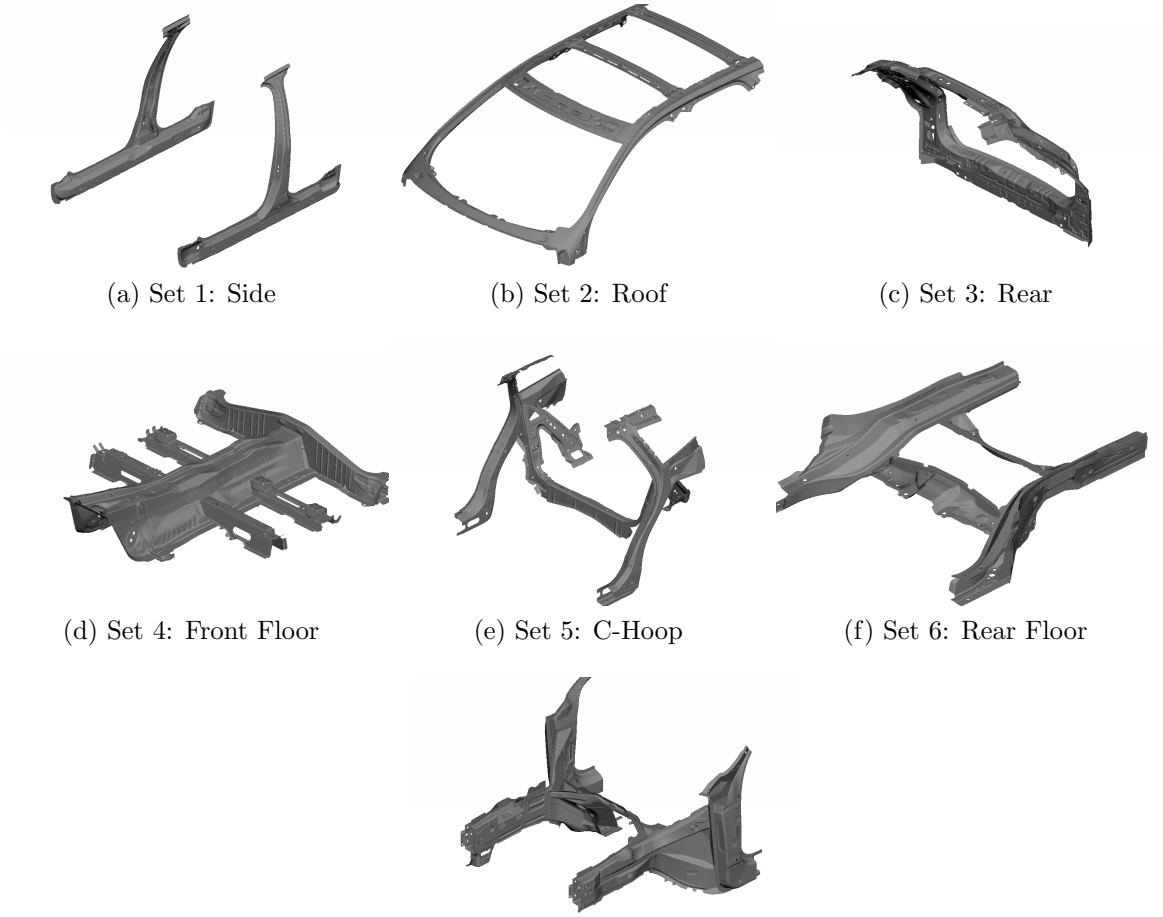

(a) Set 1: Side (b) Set 2: Roof (c) Set 3: Rear

(d) Set 4: Front Floor (e) Set 5: C-Hoop (f) Set 6: Rear Floor

(g) Set 7: Front

Figure 7.2: Division of the beam structure of the BIG into sets used in the case study

created a variation of the early measures and the road noise index similar to that found in the survey in Chapter 6. The ranges of parameter values can be seen in Table 7.1. In the case study, the material parameter of the different sets were varied individually as well as in a combined way. A full factorial investigation of the affect of the material properties was not possible. Instead, the material properties were varied in the 88 ways shown in Appendix C. The linear regressions presented in this chapter are based only on the 88 data points from the case study. However, the survey data points are included for the purpose of visually comparing the survey and the case study.

Table 7.1: Material data used in the case study.

Set	Material Property	Low	Baseline	High
1: Side	E [GPa]	70	210	630
	ρ [kg/m^3]	4700	7850	10100
2: Roof	E	105	210	630
	ρ	4700	7850	10100
3: Rear	E	105	210	630
	ρ	4700	7850	10100
4: Front Floor	E	140	210	315
	ρ	4700	7850	10100
5: C-Hoop	E	105	210	630
	ρ	4700	7850	10100
6: Rear Floor	E	105	210	630
	ρ	4700	7850	10100
7: Front	E	105	210	630
	ρ	4700	7850	10100

7.1 Eigenfrequencies

Figure 7.3 show the comparison between the eigenfrequencies of the BIG and the road noise index for the different frequency bands. No clear correlation is distinguishable for any of the modes or frequency bands. Hence, the observed tendency in Section 6.1 that a higher eigenfrequency of the *Bending* mode leads to more road noise in the drumming and rumble frequency band is not present in the case study.

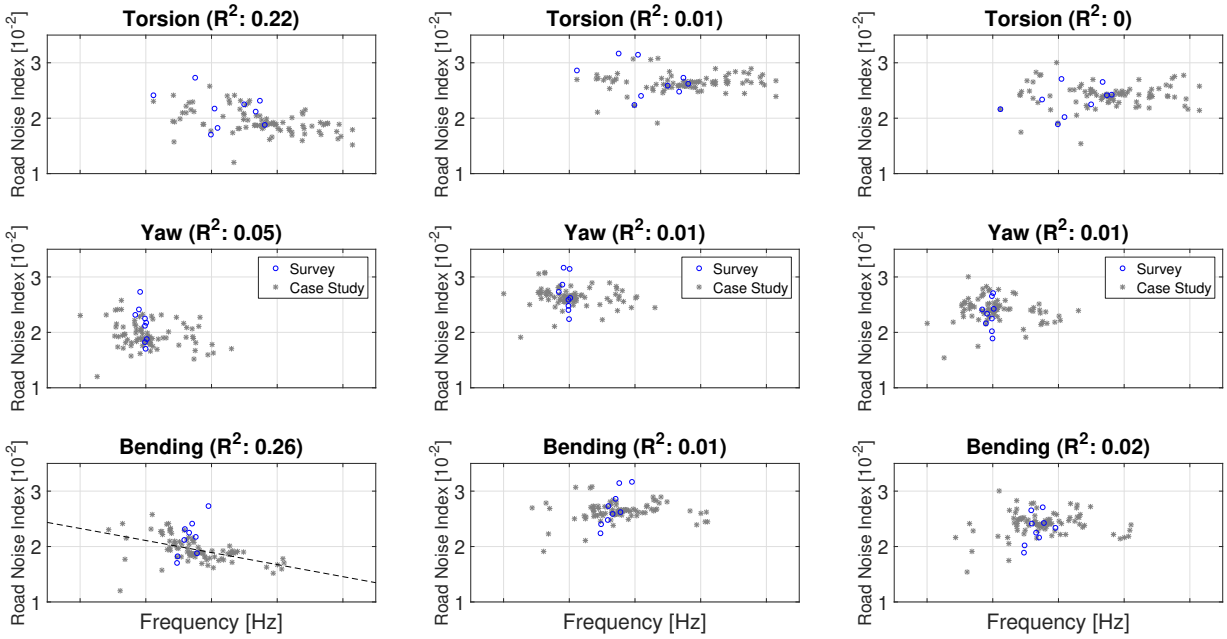

(a) Drumming: 30–60 Hz (b) Rumble: 70–150 Hz (c) Tire Cavity: 170–240 Hz

Figure 7.3: The eigenfrequencies of the BIG and the road noise index, for the different frequency bands. The dotted line is the linear approximation acquired by the use of linear regression. The x-axis grid spacing is 10 Hz.

7.2 Stiffness

Figure 7.4 show the comparison of the global stiffness of the BIG and the road noise index for the different frequency bands. A tendency for higher torsional and bending stiffness leading to less noise in the drumming region can be observed, which was observed only for the bending stiffness in the survey study in Section 6.2.

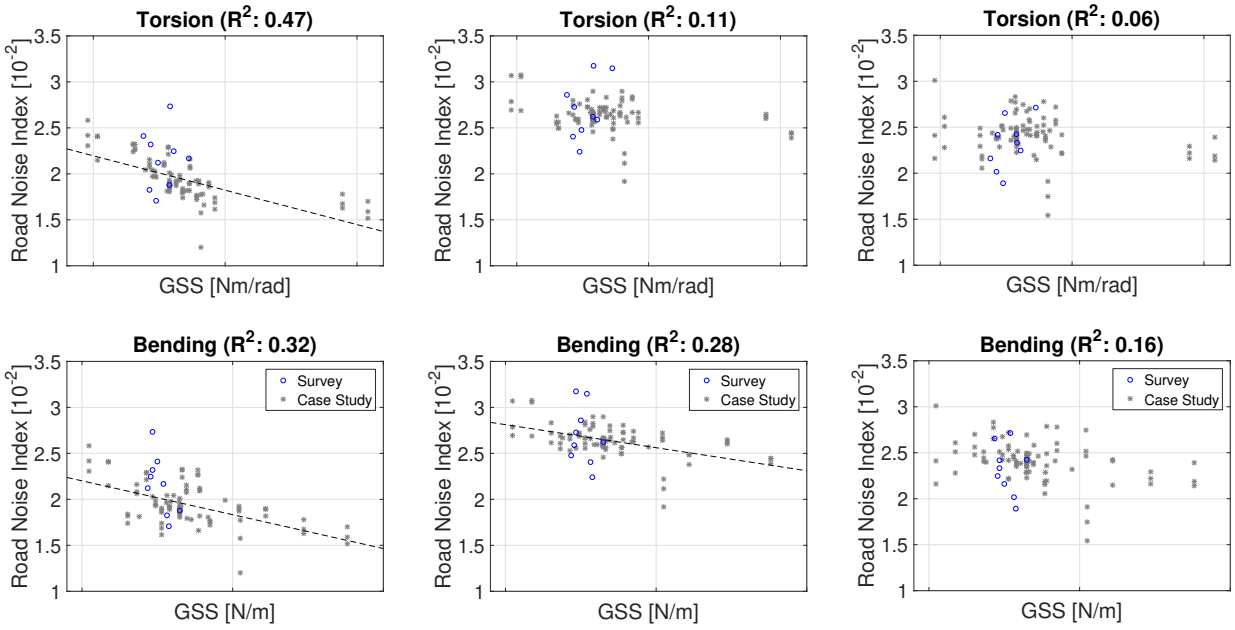

(a) Drumming: 30–60 Hz (b) Rumble: 70–150 Hz (c) Tire Cavity: 170–240 Hz

Figure 7.4: The global stiffness and the road noise index in the different frequency bands, the dotted line is the linear approximation acquired by the use of linear regression. The x-axis grid spacing is $5 * 10^5$ Nm/rad and $5 * 10^6$ N/m for the top and bottom row of plots, respectively.

7.3 Mobilities

Figures 7.5 and 7.6 shows the comparison of the mobility index and the road noise index for the different frequency bands. The evaluation points used to make this comparison are shown in Figures 6.7 and 6.9. See Appendix B for the results of the remaining subsets of points that were evaluated. The observations made in the survey in Section 6.3 are in general valid here as well. The addition is that the mobility index and the point mobility index calculated using a unit force, instead of the road-induced forces used for the road noise index, result in a better correlation.

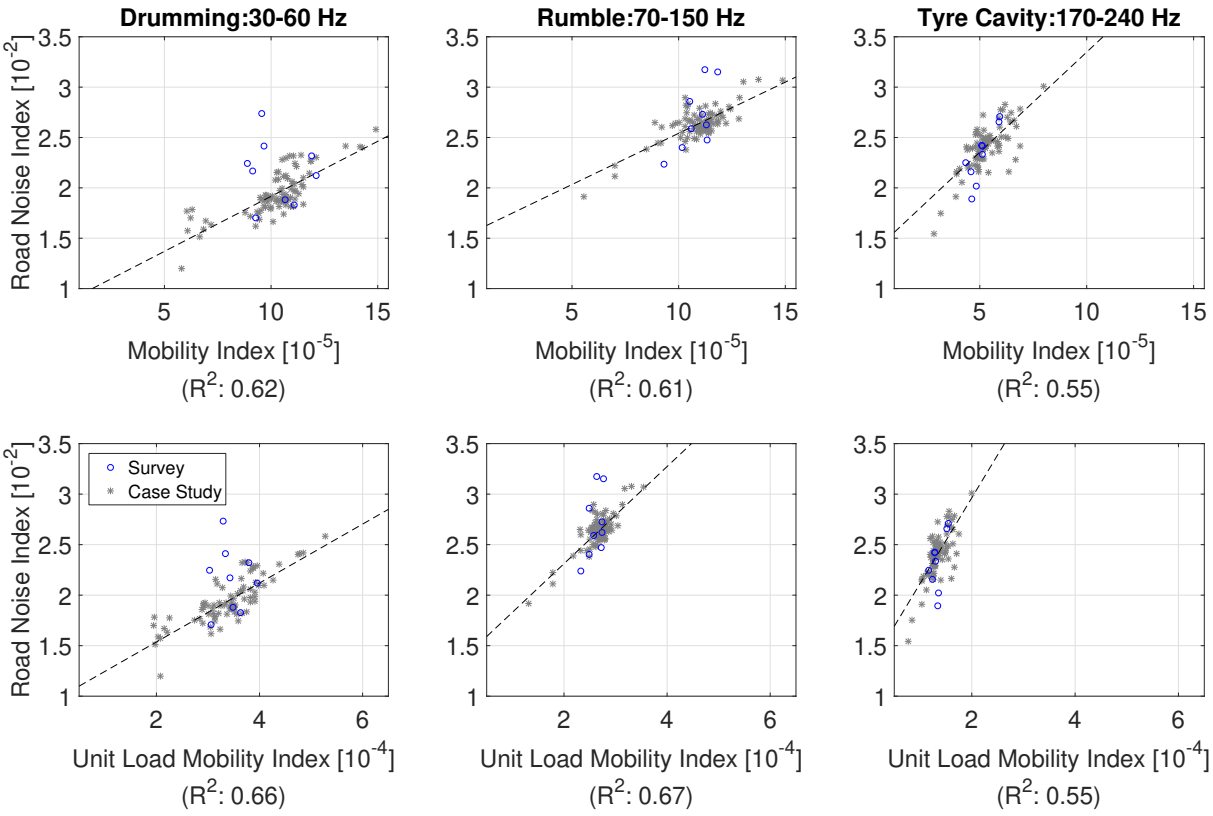

Figure 7.5: The mobility index of the BIG, calculated both using the road-induced forces described in Chapter 4 (top row) and a unit load (bottom row), and the road noise index. The mobility index is calculated using the evaluation points highlighted in Figure 6.7. The dotted line is the linear approximation acquired by use of linear regression, shown for datasets with $R^2 > 0.25$.

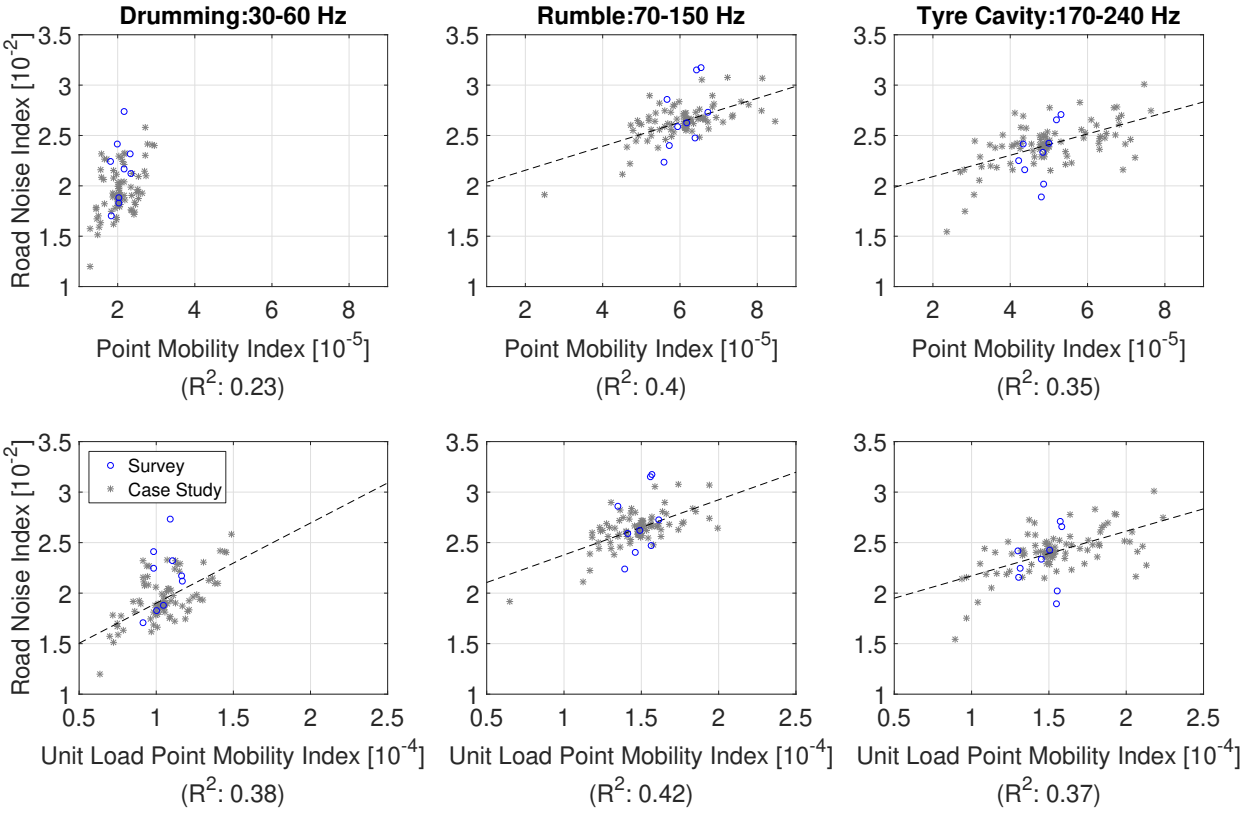

Figure 7.6: The point mobility index of the BIG, calculated both using the road-induced forces described in Chapter 4 (top row) and a unit load (bottom row), and the road noise index. The point mobility index is calculated using the evaluation points highlighted in Figure 6.9. The dotted line is the linear approximation acquired by use of linear regression, shown for datasets with $R^2 > 0.25$.

8. Conclusion and Discussion

In the dissertation, it was investigated whether simpler and more robust measures, could be used in an early concept development phase to predict the effect of the vehicle body structure on the NVH performance of the complete vehicle. The early measures were evaluated by analyzing the correlation of these to the NVH performance of the complete vehicle body. The overall NVH performance was assessed using a road noise index in order to represent the noise levels caused by road-induced loads acting on the vehicle body.

8.1 Main Observations

The results in Chapter 6 show: 1) tendencies of higher eigenfrequencies of *Bending* and *Torsion* modes leading to higher road noise index in both the drumming and rumble frequency bands, 2) a tendency of higher bending stiffness leading to lower road noise index in the drumming frequency band, 3) higher mobility index leading to higer road noise index. Subsequently, the results in Chapter 7 show: 1) weak correlation of eigenfrequencies and road noise index, 2) a tendency of higher bending and torsional stiffness leading to lower road noise index in the drumming frequency band, 3) higher mobility index leading to higher road noise index. The results in Chapters 6 and 7 lead to the following main observations:

- Some of the tendencies of correlation between early measures and road noise index observed in the survey are not present in the case study, for example, the correlation of the eigenfrequencies and road noise index is seen in the survey but not the case study. The results from the case study are used as basis for the conclusions presented here since they offer a greater statistical basis than the results from the survey.

- The comparison of road-induced forces on the body among the investigated vehicles (cf. Chapter 4 and Appendix A) indicates that the road-induced forces are similar when analyzed in broad frequency bands. Thus, this average road-induced force may be useful in the concept development stages. It should be noted that all vehicles are built on the same platform.

- There exists a general trend of higher mobility index leading to higher road noise index (cf. Chapter 7 and Appendix B). Specifically, the mobility index calculated using all of the evaluation points or those on the platform offer a measure that has a good correlation to the road noise index for all of the investigated frequency bands.

Thus, the mobility index has been shown to be a measure usable in an early concept development phase.

- Global static stiffness as an early measure offers some tendencies of correlation in the drumming frequency band (cf. Figure 7.4). The tendency is not present in higher frequency bands.
- The eigenfrequencies of the BIG and the road noise index (cf. Figure 7.3) show very weak indications of correlation, compared to the global static stiffness and mobility index.

8.2 Discussion

Applying statistical metrics on a dataset with a small sample size, such as the survey, necessitates caution when drawing conclusions. Further investigation, to ensure the statistical certainty of the survey, is needed if conclusions drawn from the survey are to be used in the concept development stages. When comparing the results of the survey to those of the case study (cf. Figure 7.3–7.6) a difference in the distribution of the results of the survey and case study is visible, for example, the mobility index in the drumming frequency band (cf. Figure 7.5). Here, the results of the survey show a greater spread of the road noise index relative to the mobility index, compared to the results of the case study. The difference in the distribution of the results implies that the early measures should be used with great caution when comparing different types of vehicles (e.g. sedans and SUVs) to each other, even when built on the same platform architecture. This should be kept in mind when setting targets, for the attributes related to the NVH performance of the BIG, in development programs.

As seen in Appendix B, the correlation between mobility index and road noise index varies heavily depending on the number and position of the evaluation points used to calculate the mobility index. Some tendencies can be discerned when inspecting all three frequency bands at the same time, such as more evaluation points and choosing evaluation points close to large panels, as those in the floor or roof, leading to a higher coefficient of determination. An argument may be made for using the mobility index calculated using a unit load, instead of the road-induced load described in Chapter 4, but the difference is slight. The point mobility index (which as previously stated is a measure of how much vibrations enters the system) does not show as high tendencies of correlation (cf. Figure 7.6) as those of the mobility index (cf. Figure 7.5).

The conclusion that the broad-band road-induced forces are similar among cars built on the same platform architecture can be used in the early concept development stages. The common road-induced load can be used for analysis until narrow band experimental load data of the car being developed is acquired. If the road-induced forces shown in Chapter 4 would be used on other cars than those built on the SPA platform, further investigations would have to be performed. A difficulty when performing this investigation is that other platforms or newer types of propulsion system may lead to different interface points between the chassis and the body. Thus, further analysis is needed if the broad-band

road-induced load is to be applied on any other types of vehicles than those investigated in the dissertation.

The observation that the global static stiffness tends to correlate to the road noise index at low frequencies is intuitive when considering a single degree of freedom mass spring system. At low frequencies, the motion can be assumed as quasi-static, and is thus controlled by the stiffness of the spring and not the mass. Similar logic can be applied to the more geometrically complex system that is the vehicle body. The absence of correlation at higher frequencies can thus possibly be explained by the stiffness measure being unable to account for the behavior due to the mass distribution.

Even though three different criteria were used to select eigenmodes for investigation of eigenfrequencies, the work to keep the results objective was difficult. The objective measure used was the MAC, which is time consuming to calculate. Calculating the MAC for all cars has a time complexity of $O(n^2)$, where n is the number of eigenmodes investigated. This excludes the work needed to select what points that should represent the structure, which is subjective, as well as the work to select the modes with highest overall MAC. In summary, these difficulties and the weak correlation imply that eigenfrequencies and modes are less suitable as early measures.

8.3 Proposals for Future Work

In order to convert the early measures into something directly applicable in the vehicle development process, further studies are needed. Mainly, more data sets would be useful in order to investigate if the found tendencies of correlation remain. Such data could be gathered through further case studies on different vehicles, and ideally the distribution from those studies would agree with the case study performed in the dissertation. Also, newly developed cars could be incorporated into the survey. It would be especially beneficial if fully electrified cars could be studied as well, since they are not a part of the investigation presented in the dissertation.

Since the early measures were evaluated for the BIG without trim items, their correlation may be improved by introducing trim components to the model of the BIG. Either through the use of FE models of trim components from previous cars, as is currently done when calculating the acoustic pressure in the early development stages, or through the use of simplified representations. This is likely to increase the correlation.

The procedure for calculating the mobilities of the BIG uses evaluation points on, essentially, the ends and the midpoints of beams. Such points capture the first bending modes of the beams, but not the higher-order modes. It would be of interest to investigate whether more evaluation points on the individual beams increases the coefficient of determination, or if the points used are sufficient.

The mobility and road noise indices are essentially calculated by applying a band-pass filter on the calculated pressure and velocity response, where data outside of the defined frequency bands is disregarded. Because the transfer functions exhibit resonant behavior, this could mean that if some change was implemented on the structure which pushes some resonance peak outside of the given frequency bands, it would not be reflected in the road noise or mobility index. If the resonance peaks are merely shifted, and not diminished,

the measures could lead one to believe that the structure has been improved when in reality this might not be the case. A better reflection of the behavior of the system may be achieved by, instead of using a band-pass filter, applying a ramp or other function that would filter the data in a smoother way. With such an approach, a gradual instead of sudden change of the road noise and mobility index would be seen if the resonance peaks are shifted outside of the frequency band of interest.

Another interesting aspect to investigate is if the general approach used in the dissertation of evaluating early measures and NVH performance is applicable to other attributes of a car. Vehicle dynamic attributes, such as handling, are possible candidate. Both the work concerning vehicle dynamics and NVH is done by performing analyses in the frequency domain and evaluating FRFs. Applying the procedure used in the dissertation would entail both finding a suitable way of evaluating the vehicle dynamic performance as well as early measures that correlate to this. Initially, the early measures investigated in the dissertation could be evaluated for this as well.

Bibliography

[1] M. Balasubramanian and A. Shaik. "Optimizing Body Panels for NVH Performance." In: *SAE International Journal of Passenger Cars: Mechanical Systems* 8.3 (2015), pp. 948–955. ISSN: 19463995.

[2] H. Bodén, U. Carlsson, R. Glav, H. P Wallin, and M. Åbom. *Ljud och Vibrationer*. Stockholm: Marcus Wallenberg Laboratoriet, 2001.

[3] B. Cho. "Spindle Load Application for NVH CAE Models by Using Principal Vector Approach". In: *SAE 2005 World Congress* (2005). ISSN: 0148-7191.

[4] R. Craig and A. Kurdila. *Fundamentals of Structural Dynamics*. Hoboken: Wiley, 2006.

[5] G. De Gaetano, D. Mundo, F. Cosco, C. Maletta, and S. Donders. "Concept Modelling of Vehicle Joints and Beam-Like Structures through Dynamic FE-Based Methods." In: *Shock and Vibration* (2014). ISSN: 1070-9622.

[6] G. De Gaetano, D. Mundo, C. Maletta, M. Kroiss, and L. Cremers. "Multi-Objective Optimization of a Vehicle Body by Combining Gradient-Based Methods and Vehicle Concept Modelling." In: *Case Studies in Mechanical Systems and Signal Processing* 1.1 (2015), p. 1. ISSN: 23519886.

[7] S. Donders, Y. Takahashi, R. Hadjit, T. Van Langenhove, M. Brughmans, B. Van Genechten, and W. Desmet. "A Reduced Beam and Joint Concept Modeling Approach to Optimize Global Vehicle Body Dynamics." In: *Finite Elements in Analysis & Design* 45 (2009), pp. 439–455. ISSN: 0168-874X.

[8] J. Helsen, L. Cremers, P. Mas, and P. Sas. "Global Static and Dynamic Car Body Stiffness Based on a Single Experimental Modal Analysis Test." In: Proceeding of ISMA 2010-USD 2010. Leuven, Belgium, 2010.

[9] K.R. Holland and F.J. Fahy. "A Guide to the Exploitation of Vibroacoustic Reciprocity in Noise Control Technology". In: ISVR Technical Report No 264. University of Southampton, (1997).

[10] D. Howard and J. Angus. *Acoustics and Psychoacoustics*. New York: Routledge, 2017.

[11] M. Klaerner, M. Wuehrl, L. Kroll, and S. Marburg. "FEA-Based Methods for Optimising Structure-Borne Sound radiation." In: *Mechanical Systems and Signal Processing* 89 (2017), pp. 37–47. ISSN: 0888-3270.

[12] J. Liang, J. Powers, S. Stevens, and B. Shahidi. "A Method of Evaluating the Joint Effectiveness on Contribution to Global Stiffness and NVH Performance of Vehicles." In: vol. 2017. SAE World Congress Experience. Cobo Center Detroit: SAE International, Mar. 2017.

[13] P. Mihaylova, N. Baldanzini, and M. Pierini. "Potential Error Factors in 1D Beam FE Modeling for the Early Stage Vehicle Design." In: *Finite Elements in Analysis & Design* 74 (2013), pp. 53–66. ISSN: 0168-874X.

[14] D. Mundo, R. Hadjit, S. Donders, M. Brughmans, P. Mas, and W. Desmet. "Simplified Modelling of Joints and Beam-Like Structures for BIW Optimization in a Concept Phase of the Vehicle Design Process." In: *Finite Elements in Analysis & Design* 45 (2009), pp. 456–462. ISSN: 0168-874X.

[15] N. Ottosen and M. Ristinmaa. *The Mechanics of Constitutive Modeling*. Lund: Elsevier, 2005.

[16] J. Park, P. Gu, J. Juan, A. Ni, and J. Van Loon. "Operational Spindle Load Estimation Methodology for Road NVH Applications". In: *SAE 2001 Noise & Vibration Conference & Exposition* (2001). ISSN: 0148-7191.

[17] *Sambandsanalys, Regression och Korrelation*. Matematikcentrum, Lund University, 2014.

[18] G. Sandberg and R. Ohayon. *Computational Aspects of Structural Acoustics and Vibration.* CISM International Centre for Mechanical Sciences: 505. Springer Vienna, 2009. ISBN: 9783211896518.

[19] S. Tebby, E. Esmailzadeh, and A Barari. "Methods to Determine Torsion Stiffness in an Automotive Chassi." In: *Computer-Aided Design & Applications* PACE (1) (2011), pp. 67–75.

[20] M. Zhang, J. Ren, Y. Yin, and J. Du. "Coach Simplified Structure Modeling and Optimization Study Based on the PBM Method." In: *Chinese Journal of Mechanical Engineering* 29.5 (2016), p. 1010. ISSN: 10009345.

A. Dynamic Forces on a Vehicle Body

In Tables A.1–A.3 the road-induced forces for all the points used in the analysis is shown.

Table A.1: Averages of road induced forces on different Volvo cars in the drumming frequency band (30–60 Hz). The forces are normalized to a largest value of 1.

Point	**Dir**	**Mean**	**Car #**	**Car #**	**Car #**	**Car #**
001	x	0.4	0.5	0.3	0.4	0.3
001	y	0.2	0.3	0.2	0.3	0.2
001	z	0.2	0.3	0.2	0.2	0.2
002	x	0.5	0.6	0.3	0.6	0.3
002	y	0.9	0.9	0.6	1.0	0.9
002	z	0.2	0.3	0.2	0.3	0.2
003	x	0.2	0.2	0.2	0.2	0.1
003	y	0.6	0.7	0.5	0.6	0.5
003	z	0.1	0.1	0.1	0.1	0.1
004	x	0.2	0.2	0.1	0.2	0.1
004	y	0.5	0.6	0.4	0.5	0.4
004	z	0.1	0.1	0.1	0.1	0.1
005	x	0.2	0.2	0.2	0.2	0.1
005	y	0.2	0.2	0.2	0.2	0.2
005	z	0.7	0.7	0.7	0.7	0.5
006	x	0.0	0.1	0.0	0.1	0.0
006	y	0.0	0.0	0.0	0.0	0.0
006	z	0.0	0.1	0.0	0.1	0.0
007	x	0.1	0.1	0.1	0.1	0.1
007	y	0.0	0.0	0.0	0.0	0.0
007	z	0.1	0.0	0.1	0.0	0.1
008	x	0.4	0.5	0.3	0.4	0.3
008	y	0.2	0.2	0.2	0.2	0.2
008	z	0.3	0.3	0.2	0.3	0.2
009	x	0.5	0.6	0.4	0.6	0.4
009	y	0.8	0.9	0.6	0.9	0.9
009	z	0.3	0.4	0.3	0.4	0.3
010	x	0.0	0.0	0.0	0.0	0.0
010	y	0.0	0.0	0.0	0.0	0.0

Continued on next page

Table A.1 – continued from previous page

Point #	Dir	Mean	Car #	Car #	Car #	Car #
010	z	0.0	0.0	0.0	0.0	0.0
011	x	0.2	0.2	0.2	0.2	0.2
011	y	0.6	0.8	0.5	0.7	0.5
011	z	0.1	0.1	0.1	0.1	0.1
012	x	0.2	0.2	0.1	0.2	0.2
012	y	0.5	0.5	0.4	0.6	0.5
012	z	0.1	0.1	0.1	0.1	0.1
013	x	0.2	0.2	0.2	0.3	0.2
013	y	0.2	0.3	0.1	0.3	0.2
013	z	0.7	1.0	0.2	1.0	0.7
014	x	0.0	0.0	0.0	0.0	0.0
014	y	0.0	0.0	0.0	0.0	0.0
014	z	0.0	0.1	0.0	0.1	0.0
015	x	0.3	0.4	0.3	0.3	0.3
015	y	0.6	0.7	0.5	0.7	0.6
015	z	0.3	0.4	0.4	0.3	0.3
016	x	0.3	0.3	0.2	0.3	0.2
016	y	0.6	0.8	0.5	0.8	0.5
016	z	0.5	0.5	0.5	0.5	0.4
017	x	0.0	0.0	0.1	0.0	0.0
017	y	0.1	0.1	0.1	0.1	0.1
017	z	0.9	0.9	1.0	0.9	0.7
018	x	0.4	0.4	0.4	0.4	0.3
018	y	0.6	0.7	0.5	0.7	0.6
018	z	0.4	0.4	0.4	0.3	0.3
019	x	0.3	0.3	0.2	0.3	0.2
019	y	0.6	0.8	0.4	0.8	0.5
019	z	0.5	0.5	0.5	0.5	0.4
020	x	0.0	0.0	0.1	0.1	0.0
020	y	0.1	0.1	0.1	0.1	0.1
020	z	0.9	1	1	1	0.7

Table A.2: Averages of road induced forces on different Volvo cars in the rumble frequency band (70–150 Hz). The forces are normalized to a largest value of 1.

Point	**Dir**	**Mean**	**Car #**	**Car #**	**Car #**	**Car #**
001	x	0.5	0.5	0.5	0.5	0.4
001	y	0.3	0.3	0.3	0.3	0.3
001	z	0.3	0.4	0.3	0.3	0.3
002	x	0.4	0.5	0.3	0.5	0.5
002	y	1.0	1.0	1.0	1.0	1.0
002	z	0.5	0.5	0.4	0.5	0.4
003	x	0.3	0.3	0.3	0.3	0.3
003	y	0.6	0.6	0.6	0.6	0.7
003	z	0.1	0.1	0.1	0.1	0.1
004	x	0.3	0.2	0.3	0.3	0.3
004	y	0.6	0.5	0.7	0.5	0.6
004	z	0.1	0.1	0.1	0.1	0.1
005	x	0.1	0.1	0.2	0.1	0.1
005	y	0.1	0.1	0.1	0.1	0.1
005	z	0.3	0.3	0.3	0.3	0.3
006	x	0.1	0.1	0.1	0.1	0.1
006	y	0.1	0.1	0.1	0.1	0.1
006	z	0.1	0.1	0.2	0.1	0.1
007	x	0.1	0.1	0.2	0.1	0.1
007	y	0.0	0.0	0.0	0.0	0.0
007	z	0.1	0.1	0.1	0.1	0.1
008	x	0.5	0.5	0.6	0.6	0.5
008	y	0.3	0.3	0.3	0.3	0.3
008	z	0.4	0.4	0.3	0.4	0.4
009	x	0.4	0.5	0.4	0.4	0.4
009	y	1.0	1.0	1.0	1.0	1.0
009	z	0.3	0.3	0.2	0.3	0.3
010	x	0.0	0.0	0.0	0.0	0.0
010	y	0.0	0.0	0.0	0.0	0.0
010	z	0.0	0.0	0.0	0.0	0.0
011	x	0.3	0.3	0.3	0.3	0.4
011	y	0.7	0.6	0.6	0.6	0.8
011	z	0.1	0.1	0.1	0.1	0.1
012	x	0.3	0.3	0.3	0.3	0.3
012	y	0.6	0.5	0.7	0.5	0.7
012	z	0.1	0.1	0.1	0.1	0.1
013	x	0.2	0.2	0.2	0.2	0.1
013	y	0.1	0.1	0.1	0.1	0.1
013	z	0.3	0.4	0.2	0.4	0.3
014	x	0.1	0.1	0.1	0.1	0.1

Continued on next page

Table A.2 – continued from previous page

Point #	Dir	Mean	Car #	Car #	Car #	Car #
014	y	0.1	0.1	0.1	0.1	0.1
014	z	0.1	0.1	0.2	0.1	0.1
015	x	0.4	0.4	0.4	0.4	0.4
015	y	0.5	0.5	0.5	0.5	0.5
015	z	0.5	0.6	0.5	0.5	0.6
016	x	0.3	0.3	0.3	0.3	0.3
016	y	0.4	0.4	0.4	0.4	0.4
016	z	0.5	0.5	0.4	0.5	0.5
017	x	0.2	0.2	0.1	0.2	0.1
017	y	0.1	0.1	0.1	0.1	0.1
017	z	0.4	0.4	0.4	0.4	0.4
018	x	0.4	0.4	0.4	0.4	0.4
018	y	0.5	0.5	0.5	0.5	0.5
018	z	0.5	0.5	0.5	0.4	0.5
019	x	0.3	0.3	0.2	0.3	0.3
019	y	0.4	0.4	0.4	0.4	0.4
019	z	0.5	0.5	0.4	0.4	0.6
020	x	0.2	0.2	0.1	0.2	0.1
020	y	0.1	0.1	0.1	0.1	0.1
020	z	0.4	0.4	0.4	0.4	0.4

Table A.3: Averages of road induced forces on different Volvo cars in the tyre cavity frequency band (170–240 Hz). The forces are normalized to a largest value of 1.

Point	**Dir**	**Mean**	**Car #**	**Car #**	**Car #**	**Car #**
001	x	0.9	0.9	1.0	0.7	0.8
001	y	0.3	0.3	0.3	0.2	0.3
001	z	0.5	0.4	0.6	0.5	0.5
002	x	0.7	0.6	0.7	0.7	0.6
002	y	0.7	0.8	0.6	0.7	0.8
002	z	0.6	0.7	0.5	0.8	0.5
003	x	0.1	0.1	0.2	0.1	0.2
003	y	0.3	0.2	0.3	0.3	0.4
003	z	0.1	0.1	0.1	0.1	0.1
004	x	0.1	0.1	0.2	0.1	0.2
004	y	0.3	0.3	0.4	0.3	0.4
004	z	0.1	0.1	0.1	0.1	0.1
005	x	0.2	0.2	0.2	0.2	0.2
005	y	0.1	0.1	0.1	0.1	0.1
005	z	0.4	0.4	0.4	0.5	0.4
006	x	0.1	0.1	0.3	0.1	0.1
006	y	0.1	0.1	0.2	0.1	0.1
006	z	0.2	0.2	0.2	0.2	0.1
007	x	0.3	0.2	0.4	0.2	0.4
007	y	0.1	0.1	0.1	0.1	0.1
007	z	0.2	0.1	0.3	0.1	0.2
008	x	0.9	0.9	1.0	0.8	0.9
008	y	0.2	0.2	0.2	0.2	0.2
008	z	0.5	0.4	0.6	0.6	0.5
009	x	0.9	1.0	0.9	1.0	0.8
009	y	0.7	0.7	0.6	0.7	0.8
009	z	0.6	0.6	0.6	0.6	0.5
010	x	0.0	0.0	0.0	0.0	0.0
010	y	0.0	0.0	0.0	0.0	0.1
010	z	0.0	0.0	0.0	0.0	0.0
011	x	0.2	0.1	0.2	0.2	0.2
011	y	0.3	0.2	0.3	0.3	0.4
011	z	0.1	0.1	0.1	0.1	0.1
012	x	0.2	0.1	0.2	0.2	0.2
012	y	0.3	0.2	0.4	0.3	0.3
012	z	0.1	0.1	0.1	0.1	0.1
013	x	0.2	0.2	0.2	0.2	0.3
013	y	0.2	0.2	0.2	0.2	0.1
013	z	0.5	0.6	0.4	0.7	0.5
014	x	0.2	0.1	0.3	0.1	0.1

Continued on next page

Table A.3 – continued from previous page

Point #	Dir	Mean	Car #	Car #	Car #	Car #
014	y	0.2	0.1	0.2	0.2	0.1
014	z	0.2	0.2	0.3	0.2	0.1
015	x	0.4	0.4	0.6	0.4	0.5
015	y	0.5	0.4	0.5	0.6	0.5
015	z	0.2	0.2	0.3	0.2	0.2
016	x	0.2	0.2	0.3	0.1	0.3
016	y	0.5	0.5	0.5	0.5	0.5
016	z	0.2	0.2	0.1	0.2	0.2
017	x	0.1	0.1	0.1	0.1	0.1
017	y	0.1	0.0	0.1	0.0	0.1
017	z	0.3	0.3	0.4	0.3	0.3
018	x	0.4	0.4	0.5	0.4	0.5
018	y	0.5	0.5	0.5	0.6	0.5
018	z	0.2	0.2	0.3	0.2	0.2
019	x	0.2	0.2	0.3	0.2	0.3
019	y	0.5	0.5	0.6	0.5	0.5
019	z	0.2	0.2	0.1	0.2	0.2
020	x	0.1	0.1	0.1	0.1	0.1
020	y	0.1	0.0	0.1	0.0	0.1
020	z	0.3	0.3	0.4	0.3	0.3

B. Mobilities as an Early Measure

This appendix shows an overview of all the different sets of evaluation points, used for calculating the mobility index, investigated in this dissertation. First the results from the survey of the existing vehicles are presented followed by those of the case study.

B.1 Survey of Current Vehicles

In Figures B.1–B.36 the results for the mobility index used as an early measure for all the subset of points analyzed is shown. The position of these respective points are included in the Figures directly following the results.

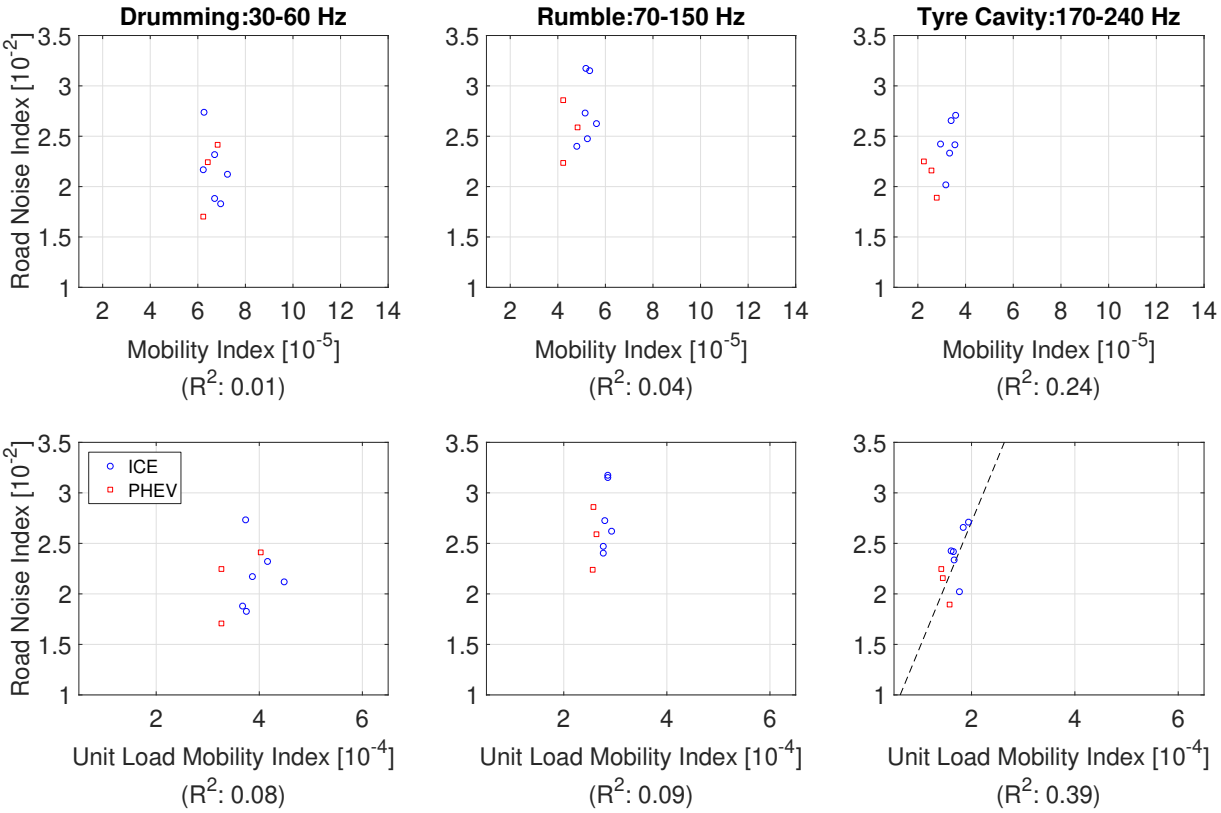

Figure B.1: The mobility index of the BIG, calculated both using the discretized forces described in Chapter 4 (top row) and a unit load (bottom row), and the road noise index. The mobility index is calculated using the evaluation points highlighted in Figure B.2. The dotted line is the linear approximation acquired by use of linear regression, shown for datasets with $R^2 > 0.25$.

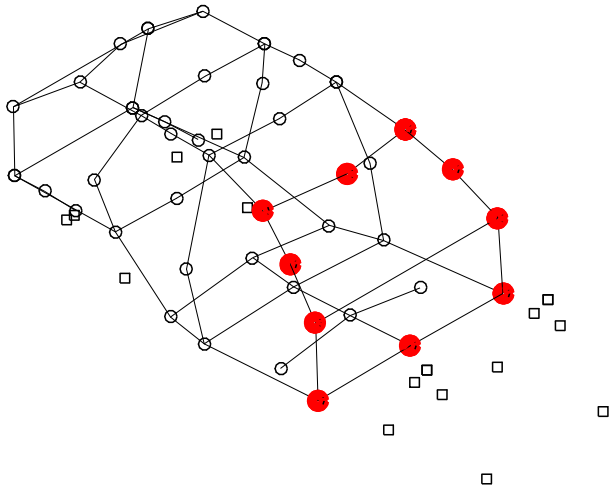

Figure B.2: Highlighted points show the evaluation points used for the result plots in Figure B.1.

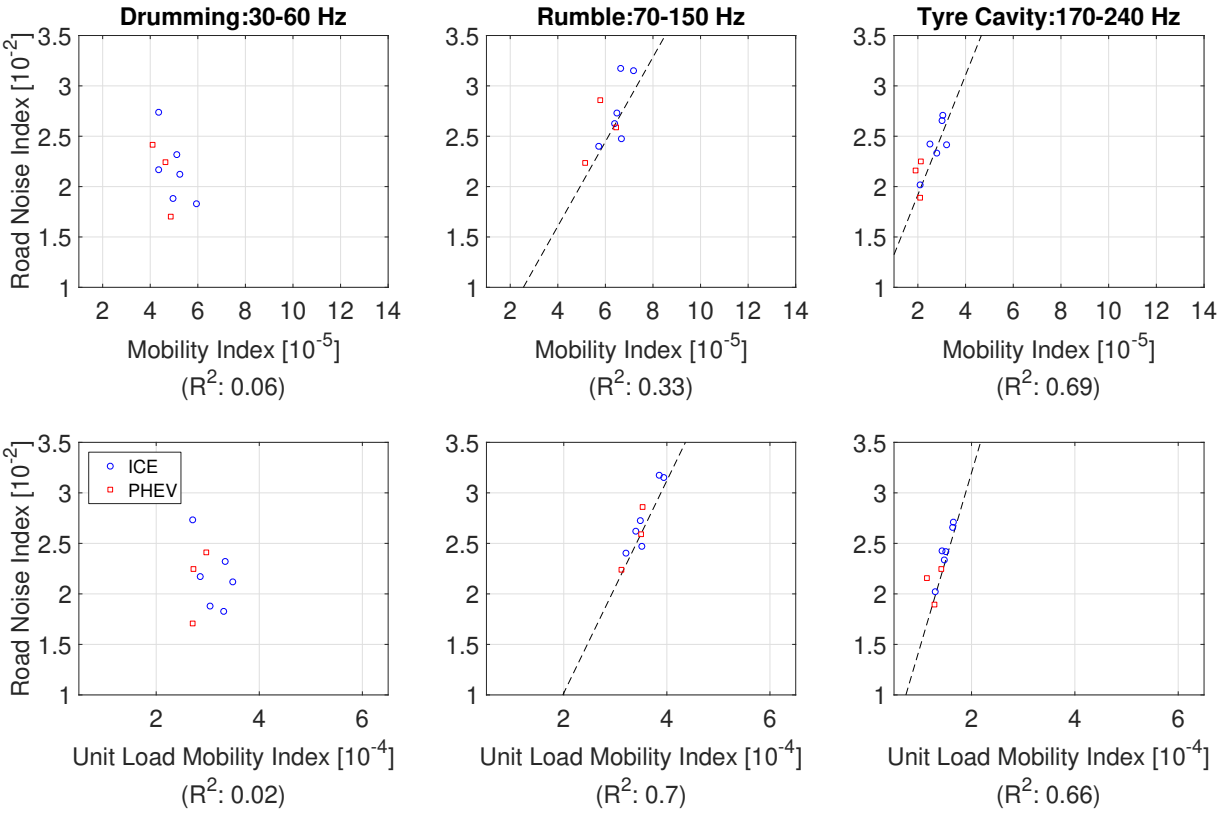

Figure B.3: The mobility index of the BIG, calculated both using the discretized forces described in Chapter 4 (top row) and a unit load (bottom row), and the road noise index. The mobility index is calculated using the evaluation points highlighted in Figure B.4. The dotted line is the linear approximation acquired by use of linear regression, shown for datasets with $R^2 > 0.25$.

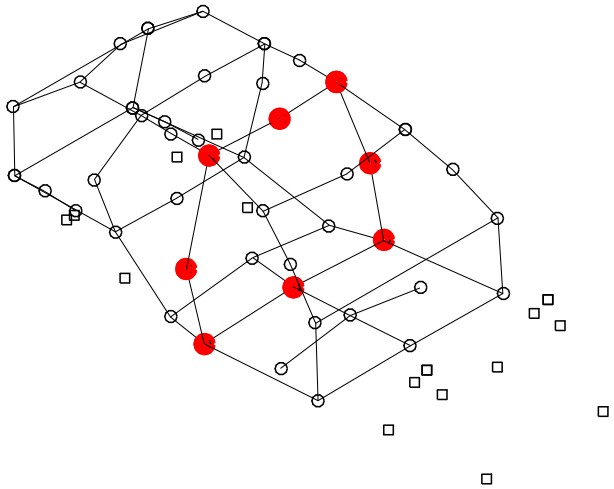

Figure B.4: Highlighted points show the evaluation points used for the result plots in Figure B.3.

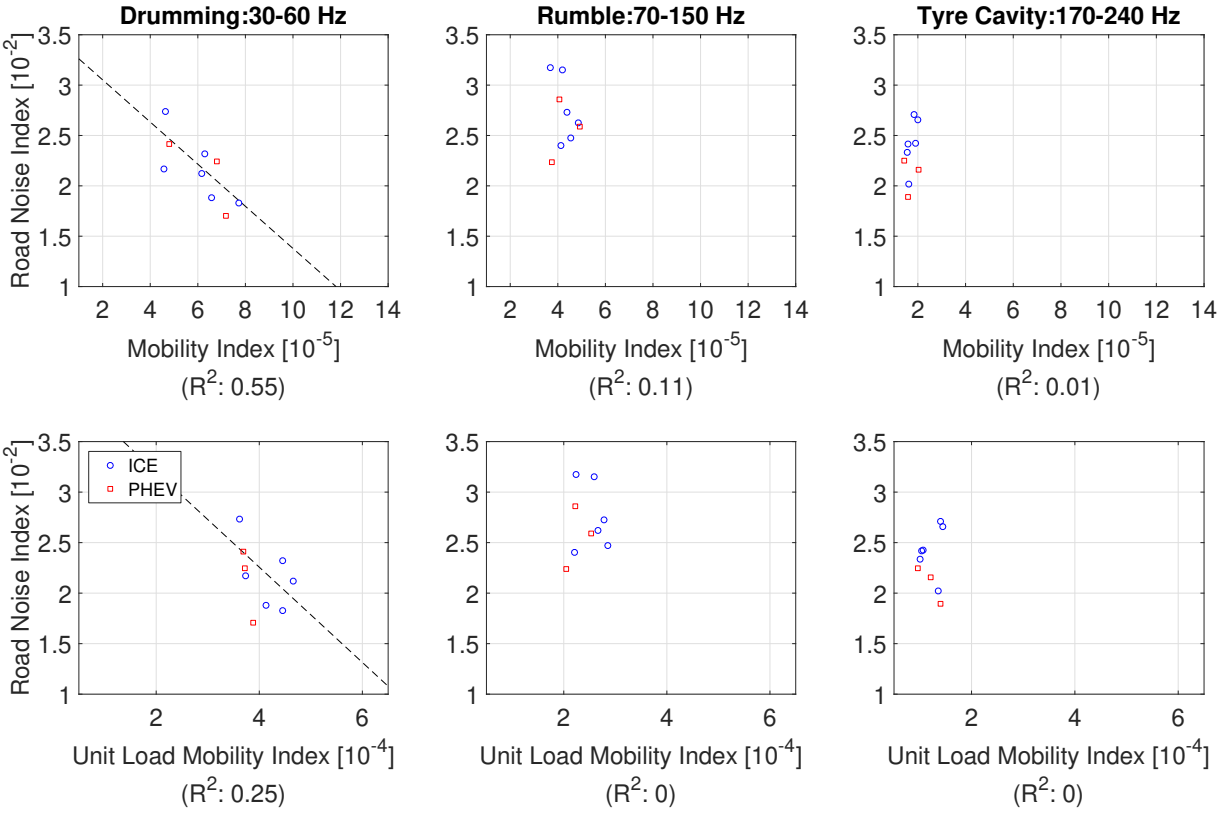

Figure B.5: The mobility index of the BIG, calculated both using the discretized forces described in Chapter 4 (top row) and a unit load (bottom row), and the road noise index. The mobility index is calculated using the evaluation points highlighted in Figure B.6. The dotted line is the linear approximation acquired by use of linear regression, shown for datasets with $R^2 > 0.25$.

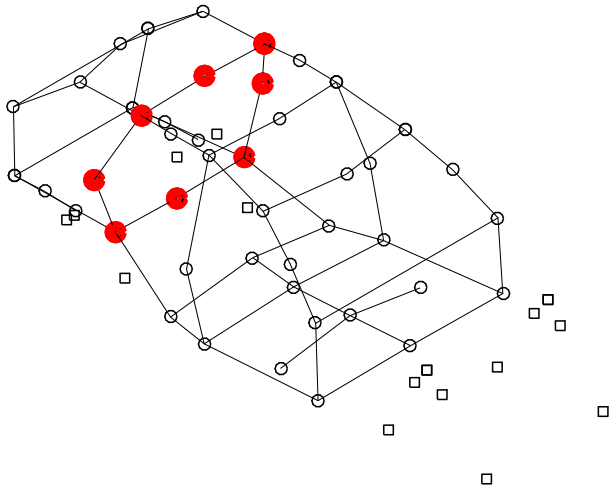

Figure B.6: Highlighted points show the evaluation points used for the result plots in Figure B.5.

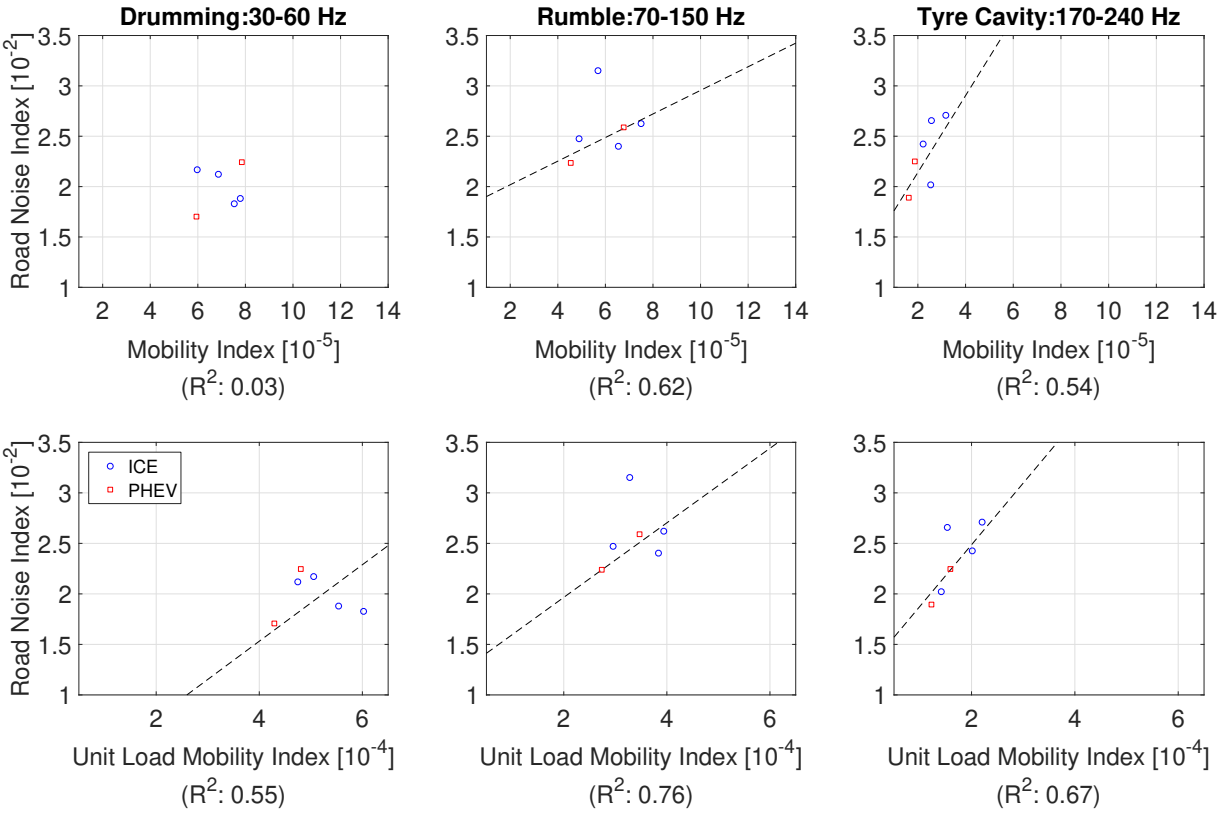

Figure B.7: The mobility index of the BIG, calculated both using the discretized forces described in Chapter 4 (top row) and a unit load (bottom row), and the road noise index. The mobility index is calculated using the evaluation points highlighted in Figure B.8. The dotted line is the linear approximation acquired by use of linear regression, shown for datasets with $R^2 > 0.25$.

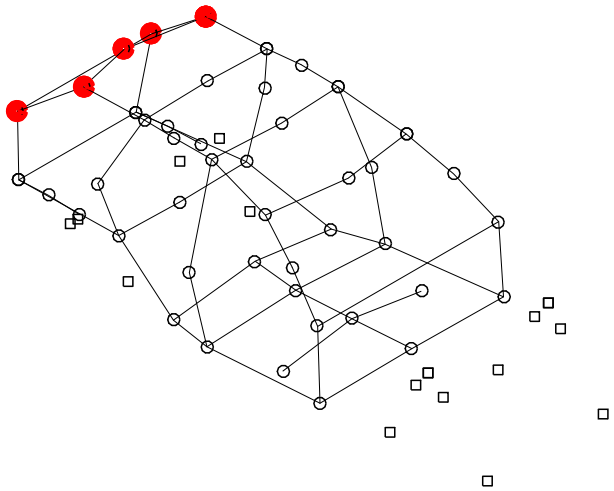

Figure B.8: Highlighted points show the evaluation points used for the result plots in Figure B.7.

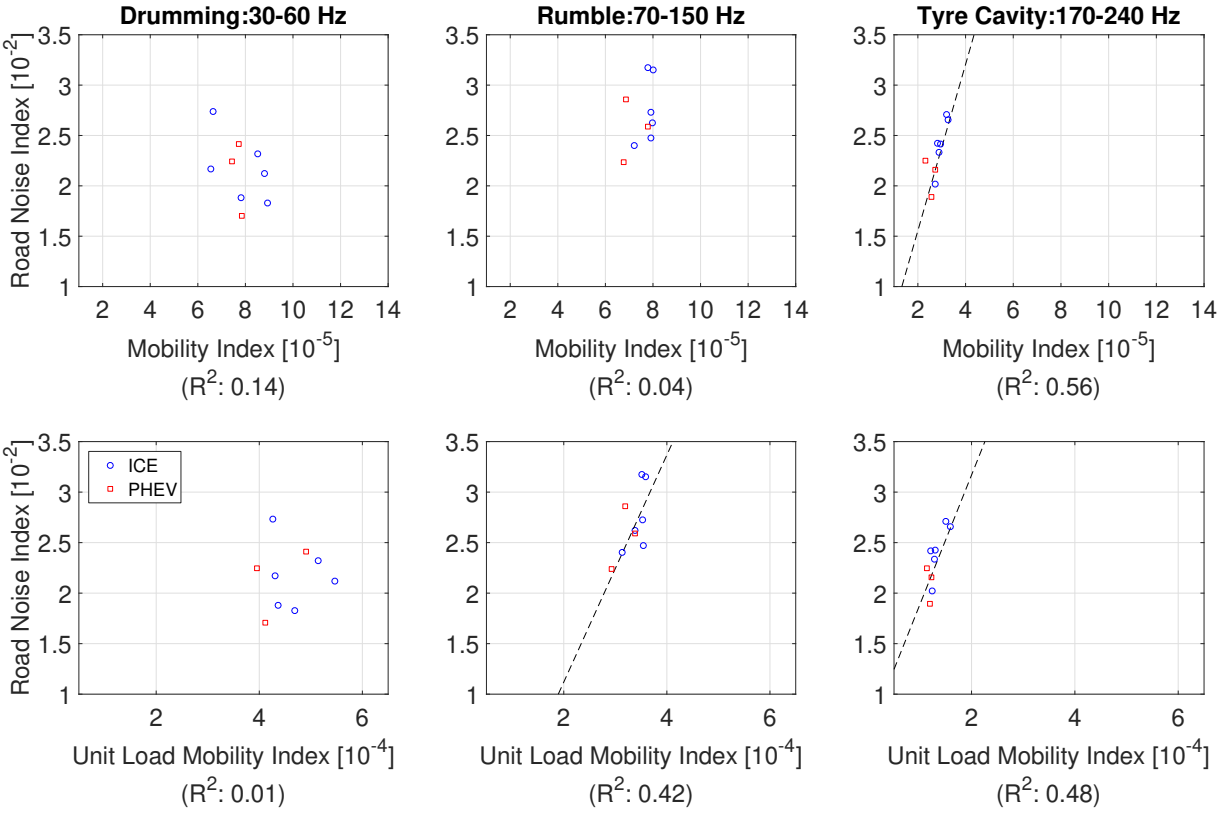

Figure B.9: The mobility index of the BIG, calculated both using the discretized forces described in Chapter 4 (top row) and a unit load (bottom row), and the road noise index. The mobility index is calculated using the evaluation points highlighted in Figure B.10. The dotted line is the linear approximation acquired by use of linear regression, shown for datasets with $R^2 > 0.25$.

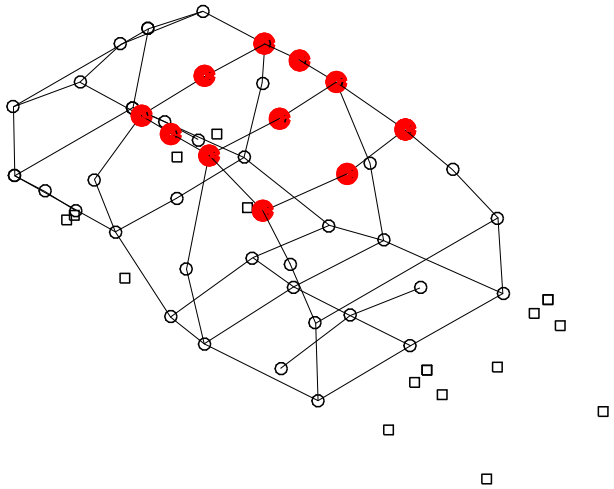

Figure B.10: Highlighted points show the evaluation points used for the result plots in Figure B.9.

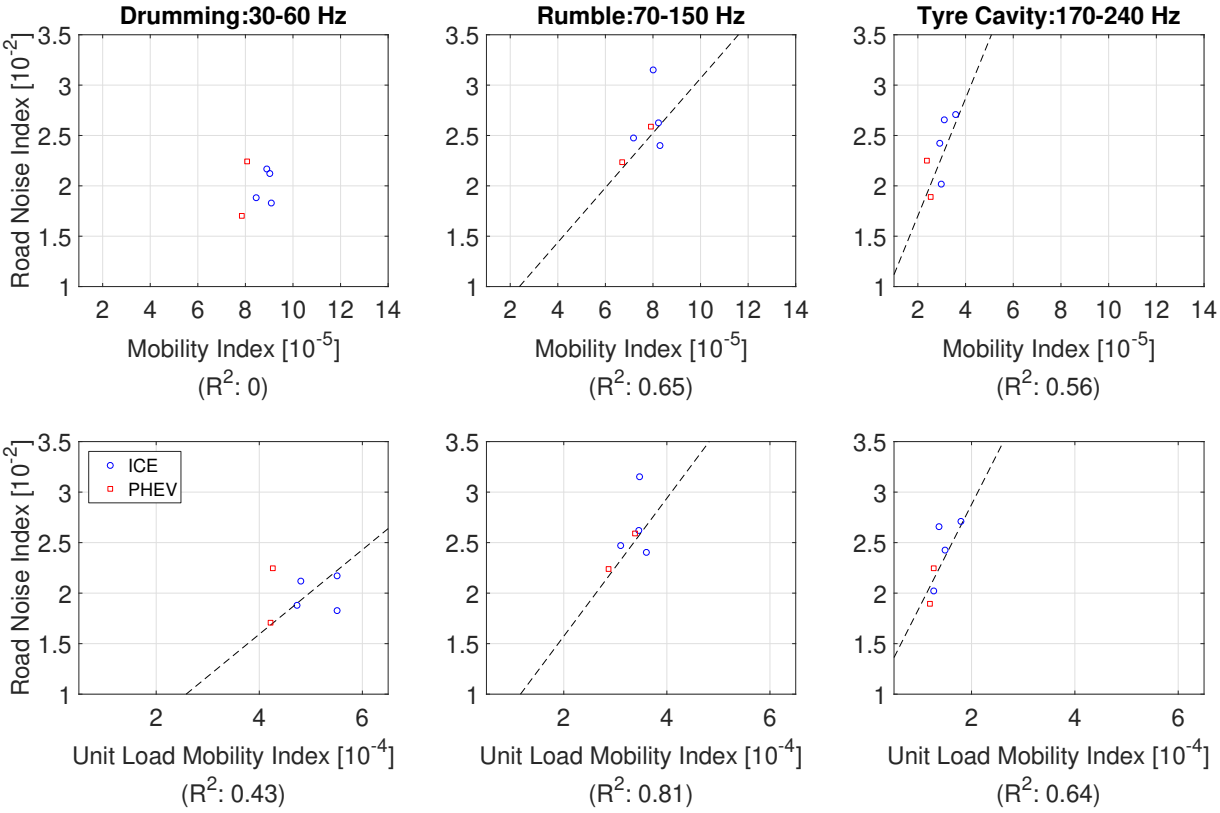

Figure B.11: The mobility index of the BIG, calculated both using the discretized forces described in Chapter 4 (top row) and a unit load (bottom row), and the road noise index. The mobility index is calculated using the evaluation points highlighted in Figure B.12. The dotted line is the linear approximation acquired by use of linear regression, shown for datasets with $R^2 > 0.25$.

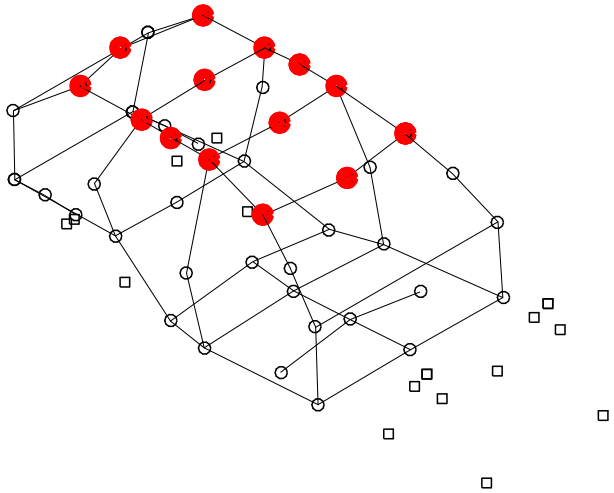

Figure B.12: Highlighted points show the evaluation points used for the result plots in Figure B.11.

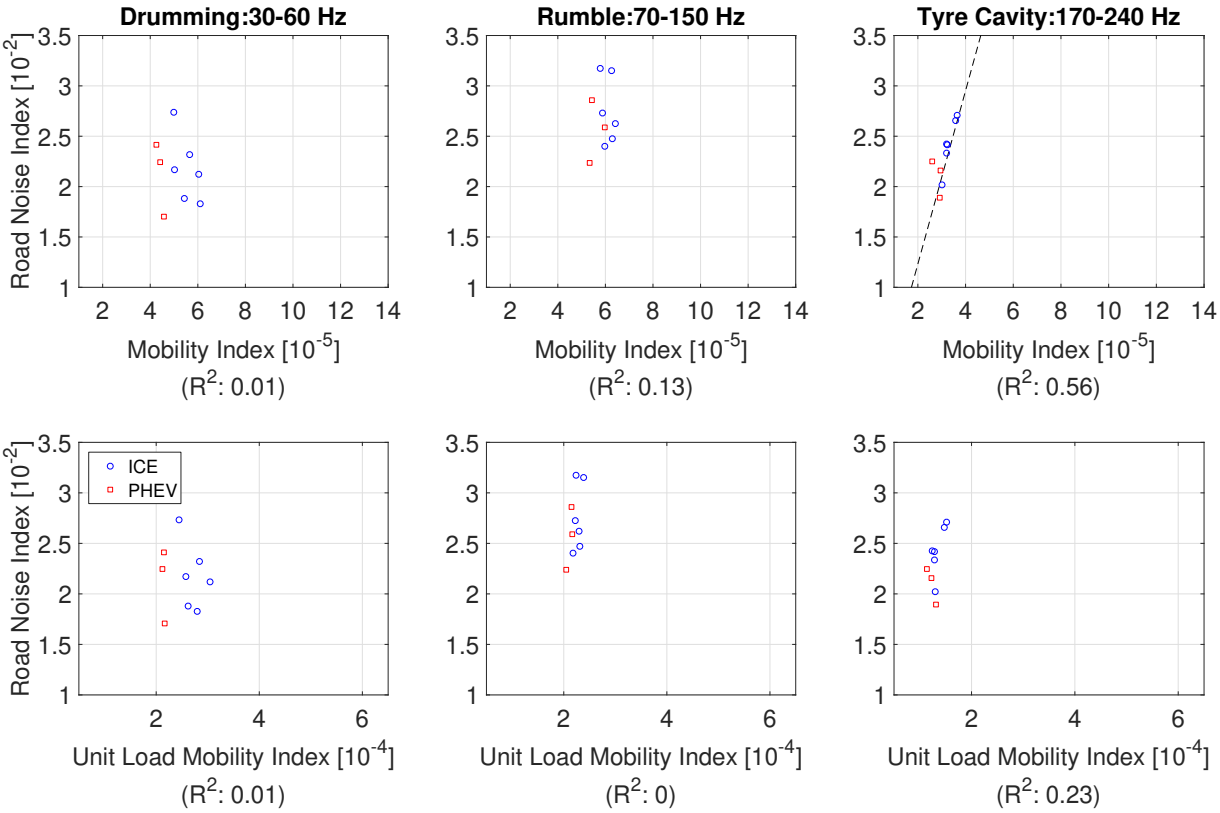

Figure B.13: The mobility index of the BIG, calculated both using the discretized forces described in Chapter 4 (top row) and a unit load (bottom row), and the road noise index. The mobility index is calculated using the evaluation points highlighted in Figure B.14. The dotted line is the linear approximation acquired by use of linear regression, shown for datasets with $R^2 > 0.25$.

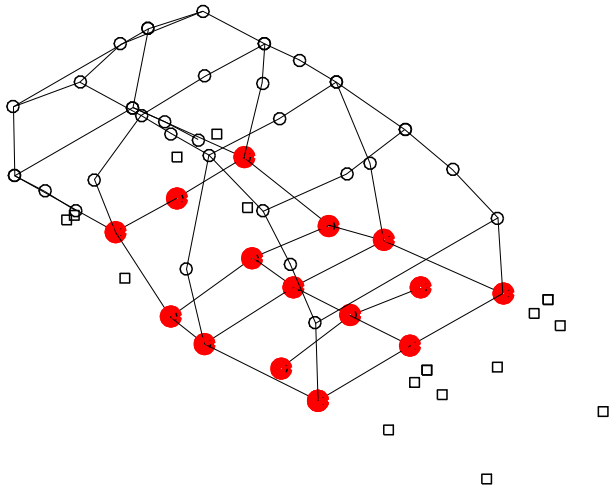

Figure B.14: Highlighted points show the evaluation points used for the result plots in Figure B.13.

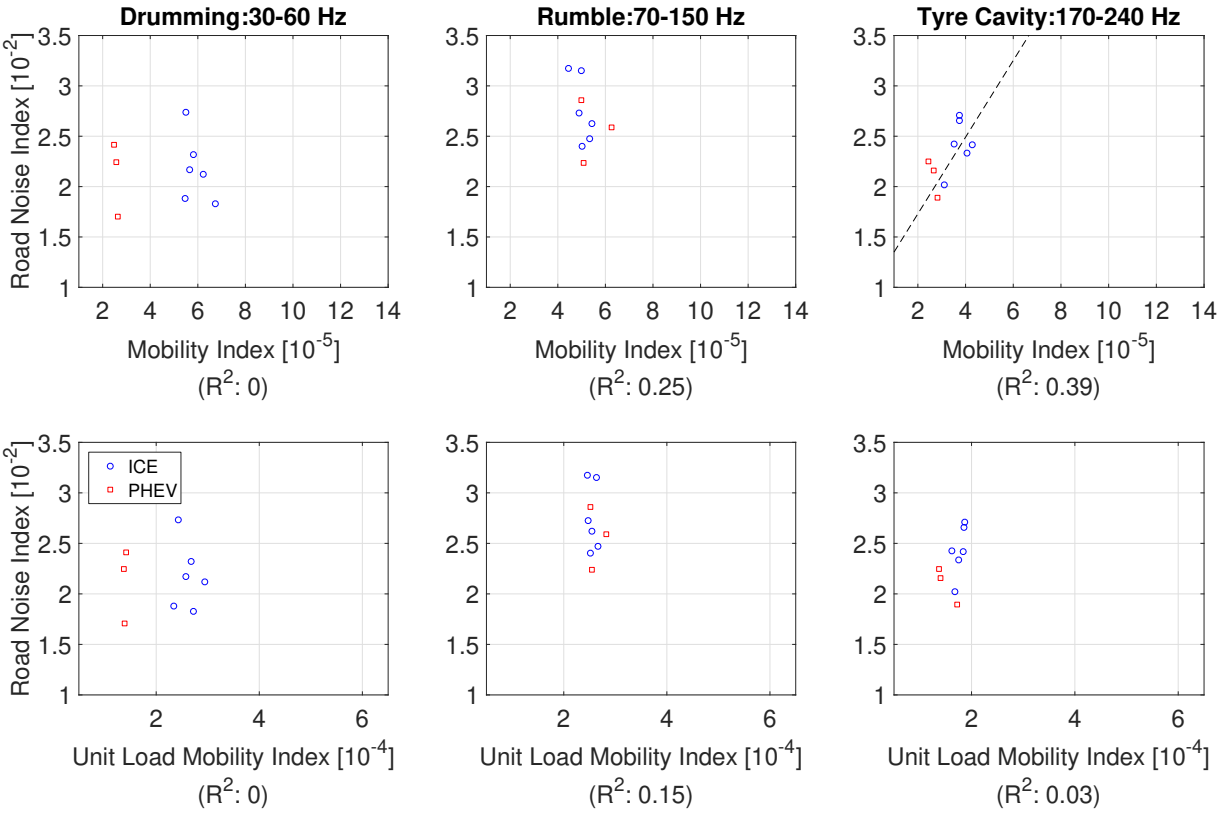

Figure B.15: The mobility index of the BIG, calculated both using the discretized forces described in Chapter 4 (top row) and a unit load (bottom row), and the road noise index. The mobility index is calculated using the evaluation points highlighted in Figure B.16. The dotted line is the linear approximation acquired by use of linear regression, shown for datasets with $R^2 > 0.25$.

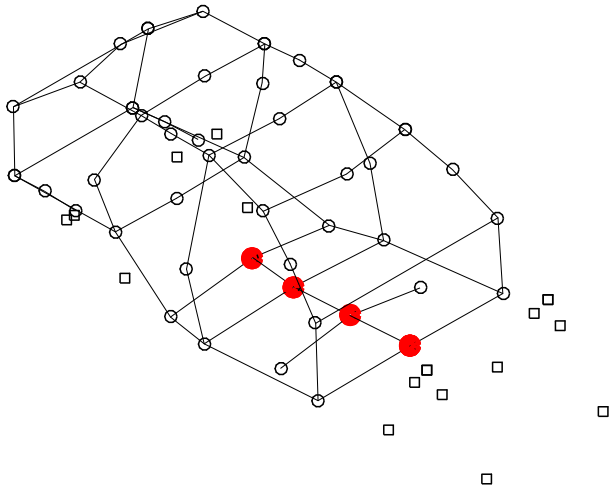

Figure B.16: Highlighted points show the evaluation points used for the result plots in Figure B.15.

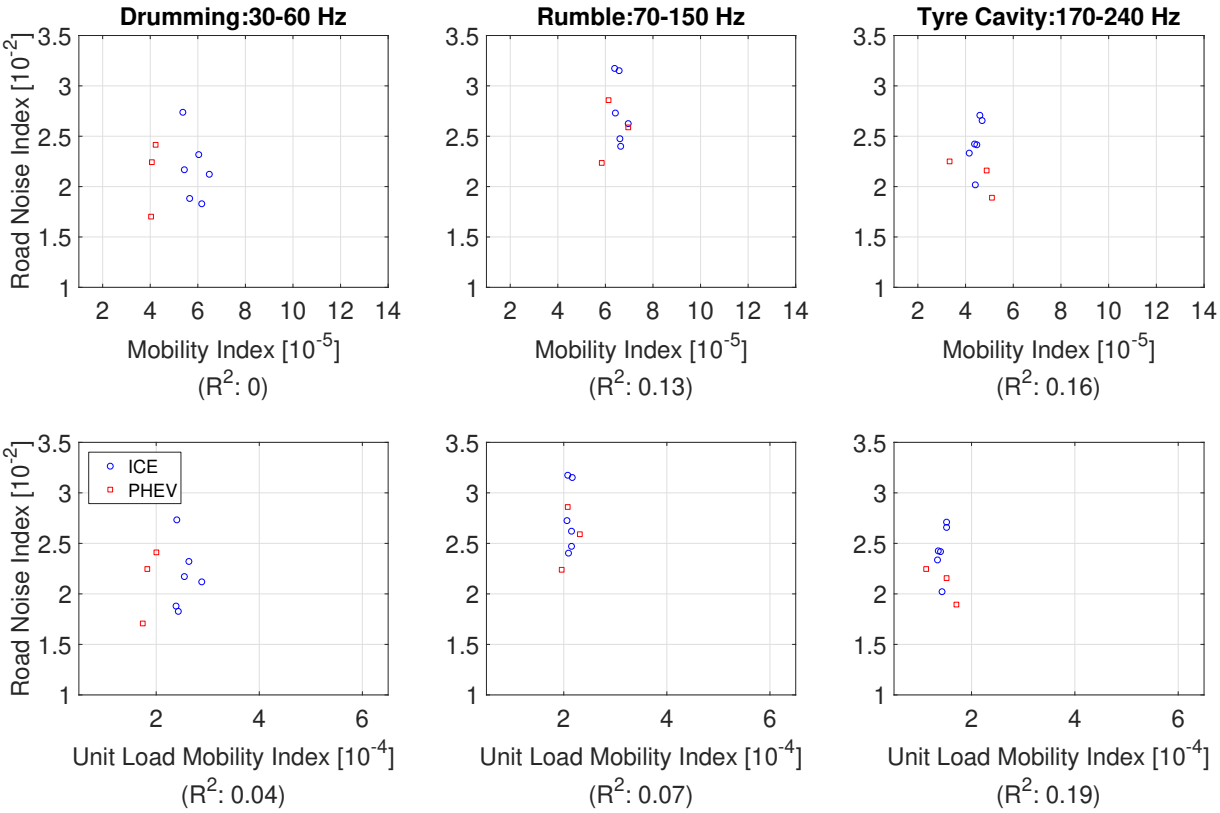

Figure B.17: The mobility index of the BIG, calculated both using the discretized forces described in Chapter 4 (top row) and a unit load (bottom row), and the road noise index. The mobility index is calculated using the evaluation points highlighted in Figure B.18. The dotted line is the linear approximation acquired by use of linear regression, shown for datasets with $R^2 > 0.25$.

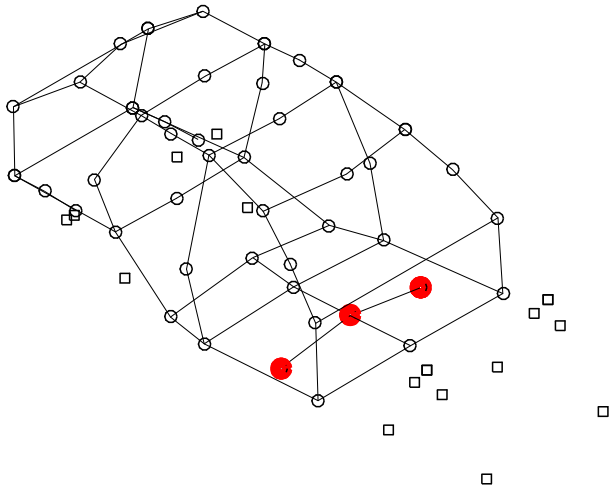

Figure B.18: Highlighted points show the evaluation points used for the result plots in Figure B.17.

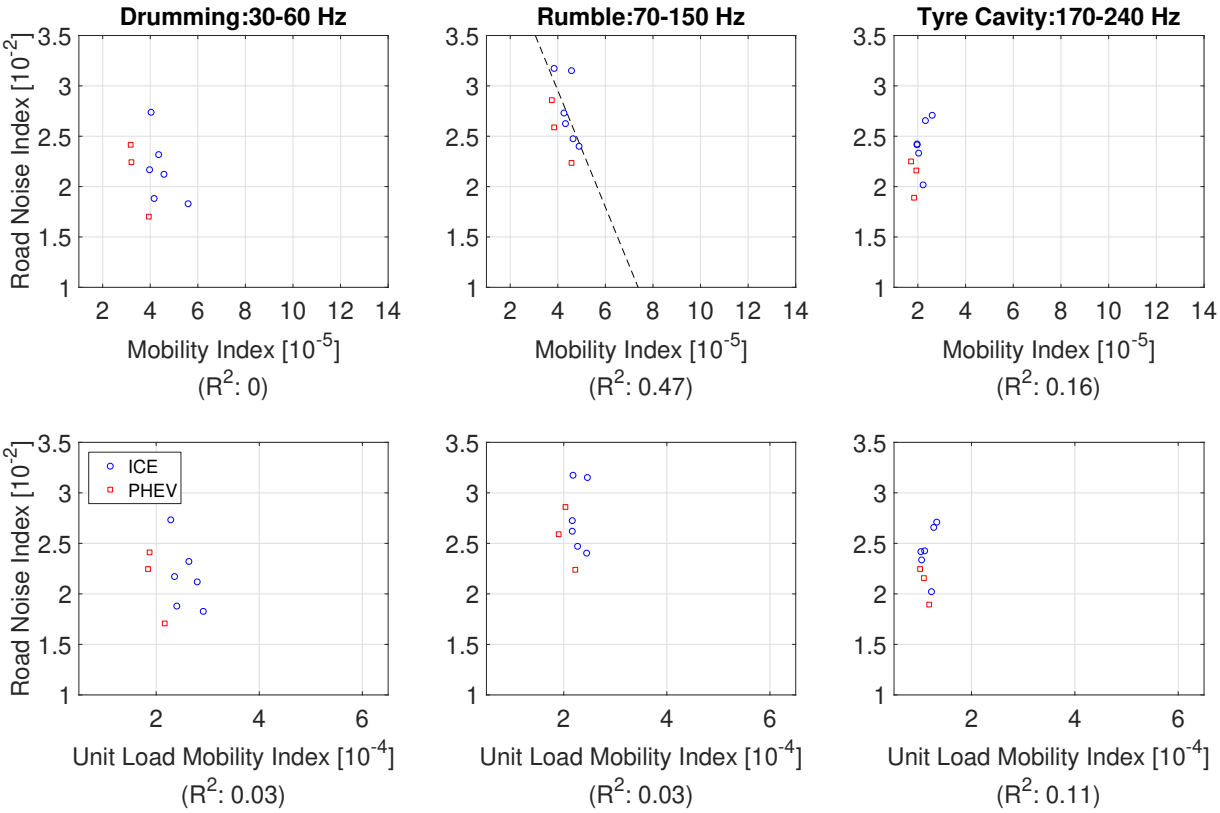

Figure B.19: The mobility index of the BIG, calculated both using the discretized forces described in Chapter 4 (top row) and a unit load (bottom row), and the road noise index. The mobility index is calculated using the evaluation points highlighted in Figure B.20. The dotted line is the linear approximation acquired by use of linear regression, shown for datasets with $R^2 > 0.25$.

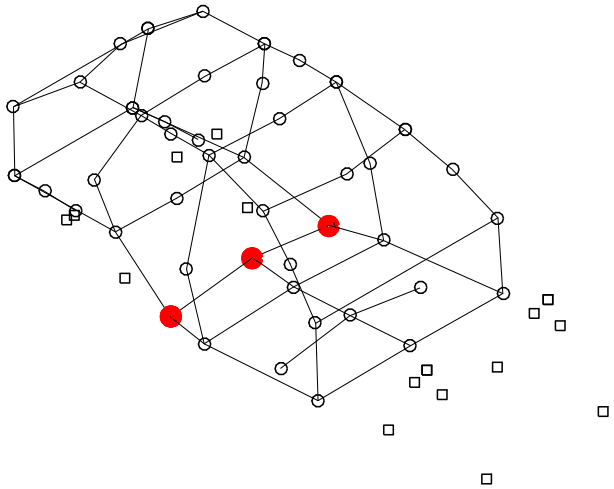

Figure B.20: Highlighted points show the evaluation points used for the result plots in Figure B.19.

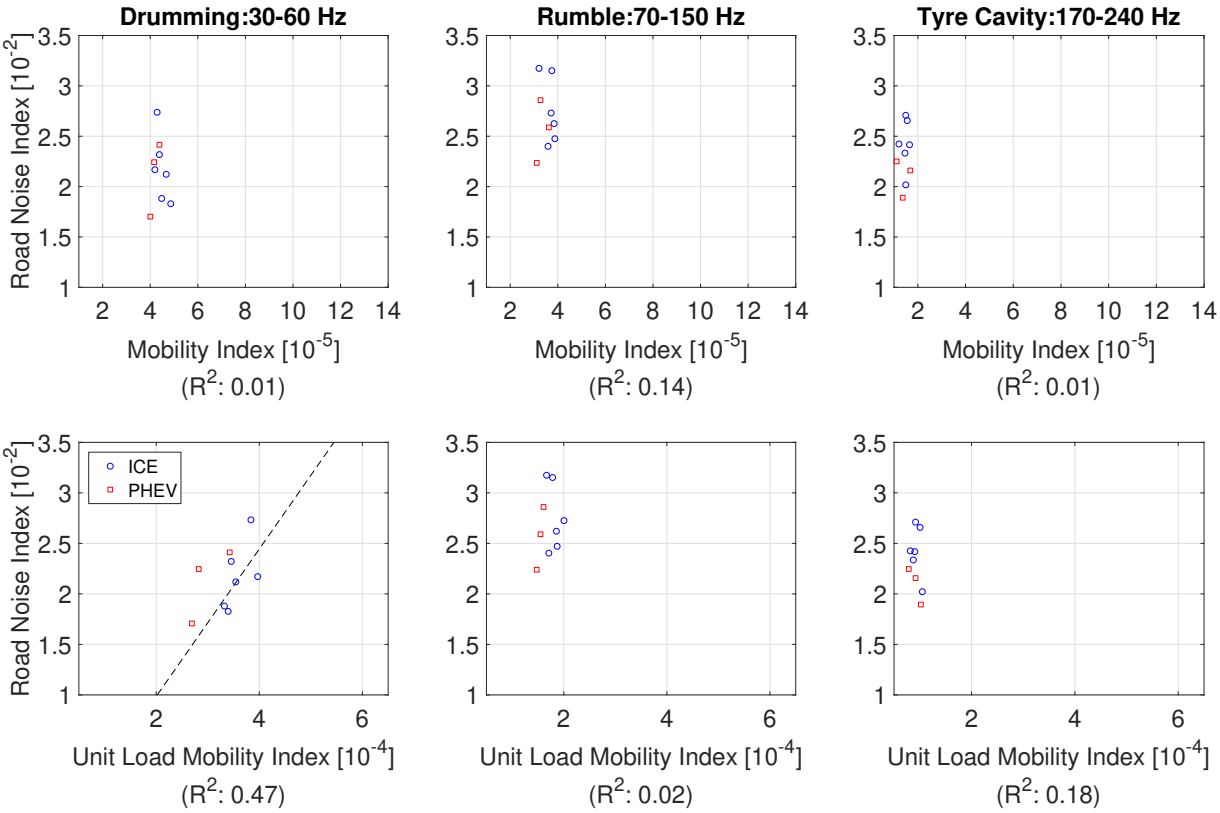

Figure B.21: The mobility index of the BIG, calculated both using the discretized forces described in Chapter 4 (top row) and a unit load (bottom row), and the road noise index. The mobility index is calculated using the evaluation points highlighted in Figure B.22. The dotted line is the linear approximation acquired by use of linear regression, shown for datasets with $R^2 > 0.25$.

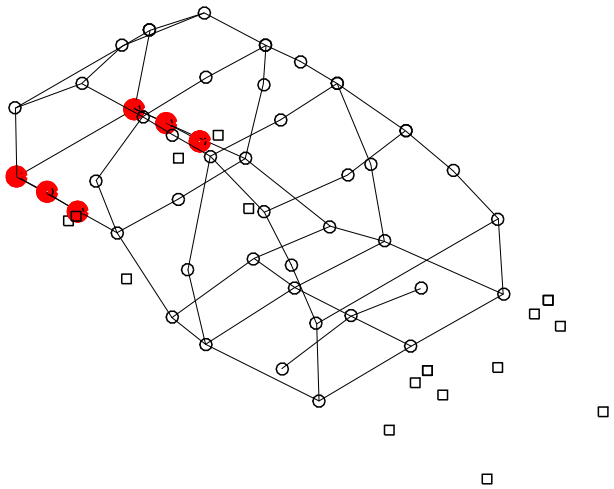

Figure B.22: Highlighted points show the evaluation points used for the result plots in Figure B.21.

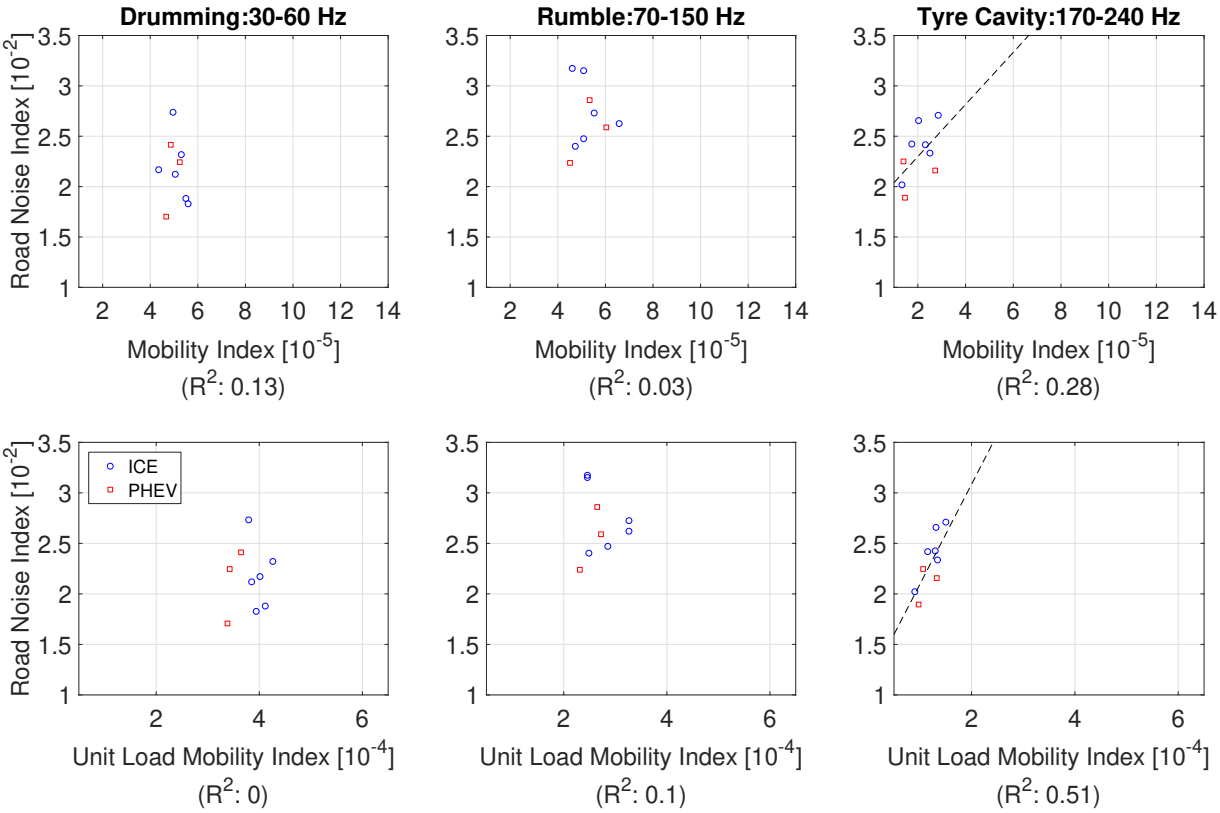

Figure B.23: The mobility index of the BIG, calculated both using the discretized forces described in Chapter 4 (top row) and a unit load (bottom row), and the road noise index. The mobility index is calculated using the evaluation points highlighted in Figure B.24. The dotted line is the linear approximation acquired by use of linear regression, shown for datasets with $R^2 > 0.25$.

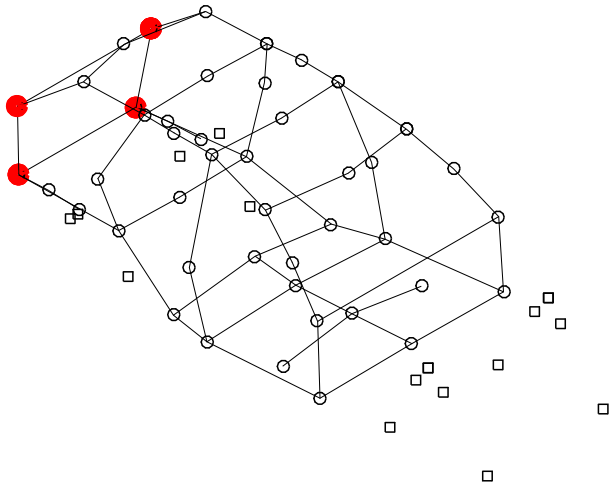

Figure B.24: Highlighted points show the evaluation points used for the result plots in Figure B.23.

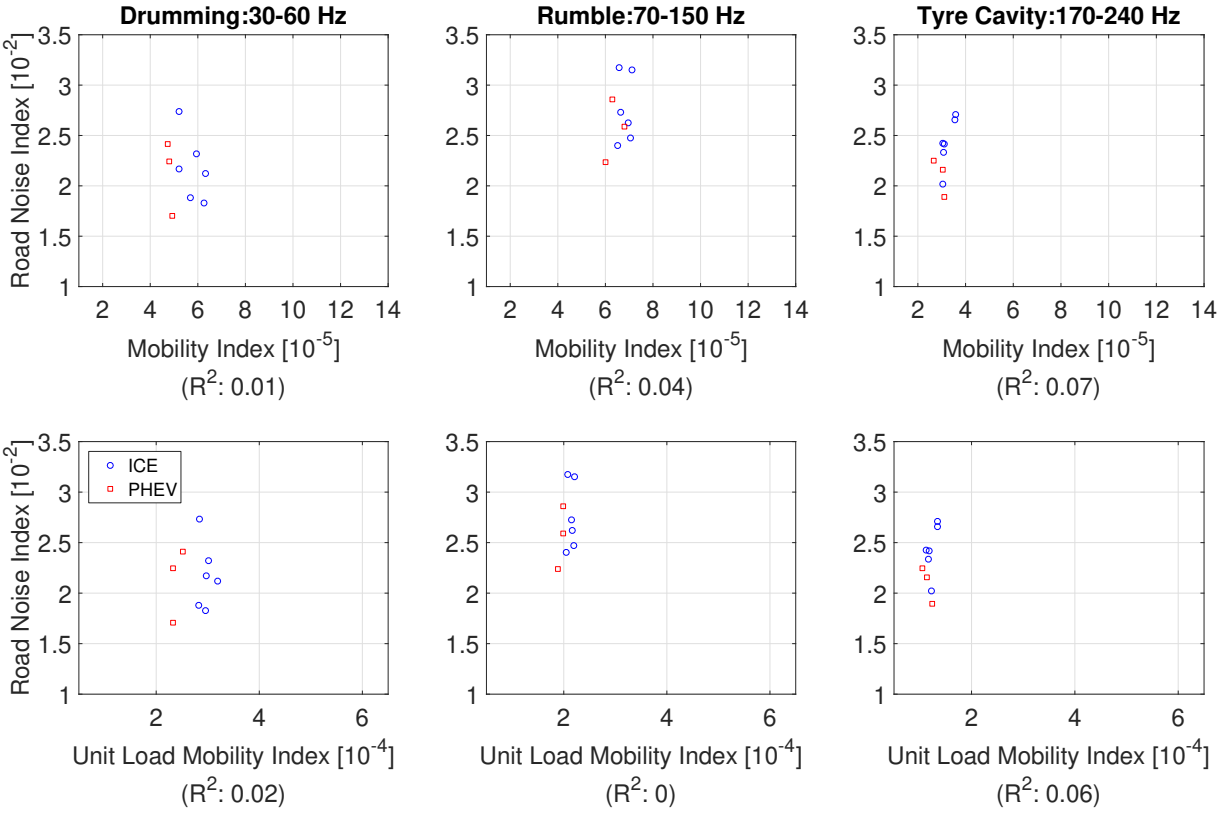

Figure B.25: The mobility index of the BIG, calculated both using the discretized forces described in Chapter 4 (top row) and a unit load (bottom row), and the road noise index. The mobility index is calculated using the evaluation points highlighted in Figure B.26. The dotted line is the linear approximation acquired by use of linear regression, shown for datasets with $R^2 > 0.25$.

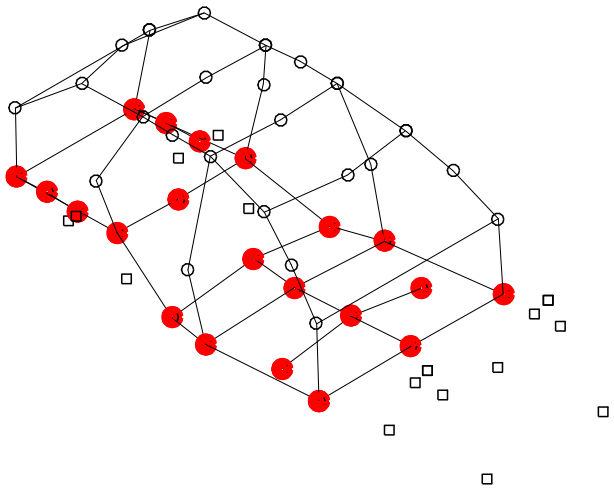

Figure B.26: Highlighted points show the evaluation points used for the result plots in Figure B.25.

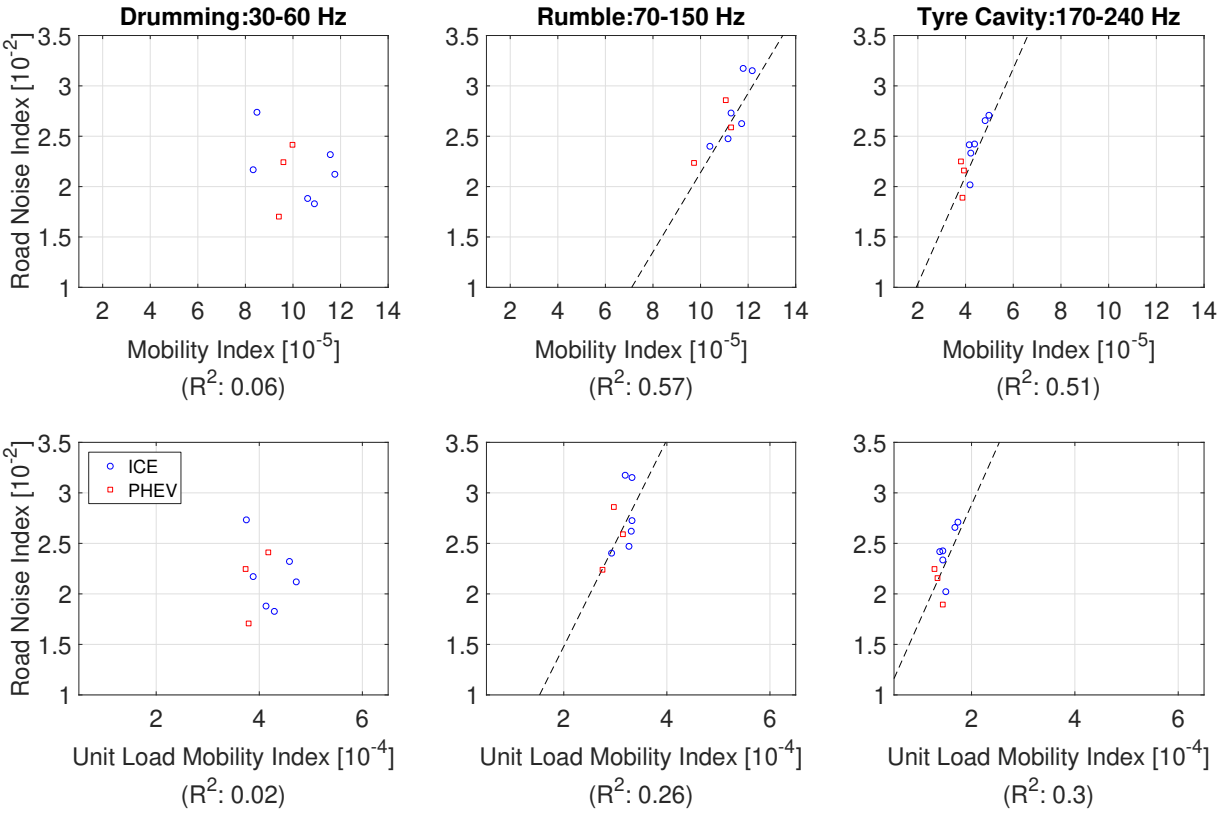

Figure B.27: The mobility index of the BIG, calculated both using the discretized forces described in Chapter 4 (top row) and a unit load (bottom row), and the road noise index. The mobility index is calculated using the evaluation points highlighted in Figure B.28. The dotted line is the linear approximation acquired by use of linear regression, shown for datasets with $R^2 > 0.25$.

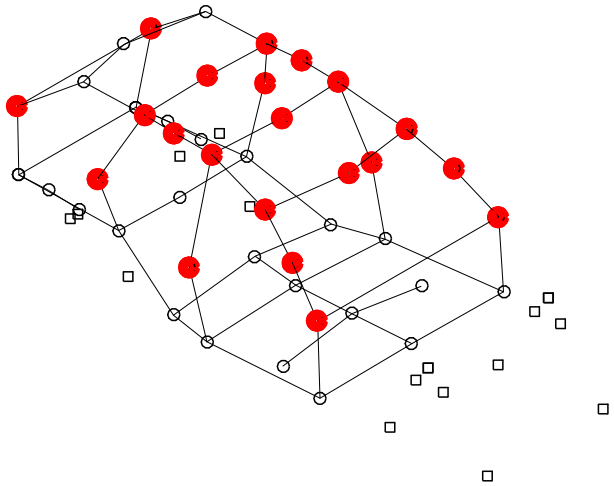

Figure B.28: Highlighted points show the evaluation points used for the result plots in Figure B.27.

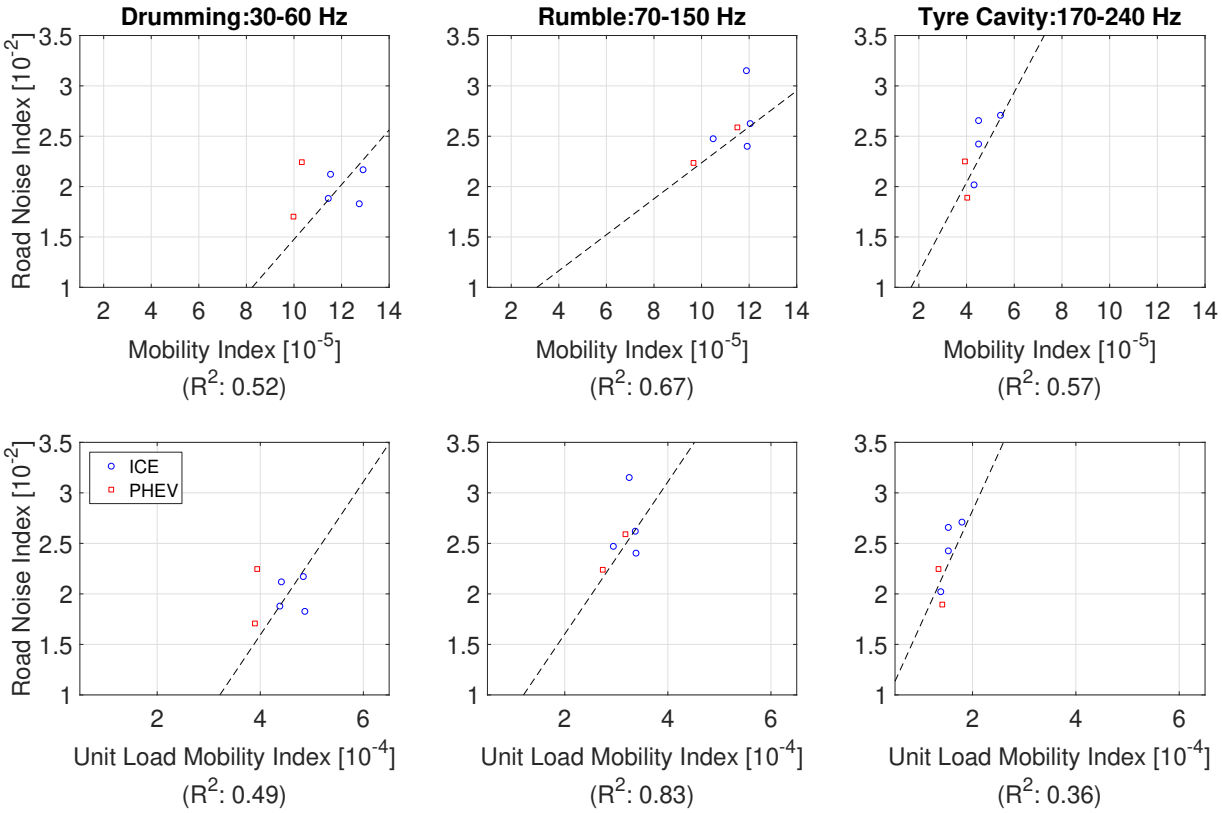

Figure B.29: The mobility index of the BIG, calculated both using the discretized forces described in Chapter 4 (top row) and a unit load (bottom row), and the road noise index. The mobility index is calculated using the evaluation points highlighted in Figure B.30. The dotted line is the linear approximation acquired by use of linear regression, shown for datasets with $R^2 > 0.25$.

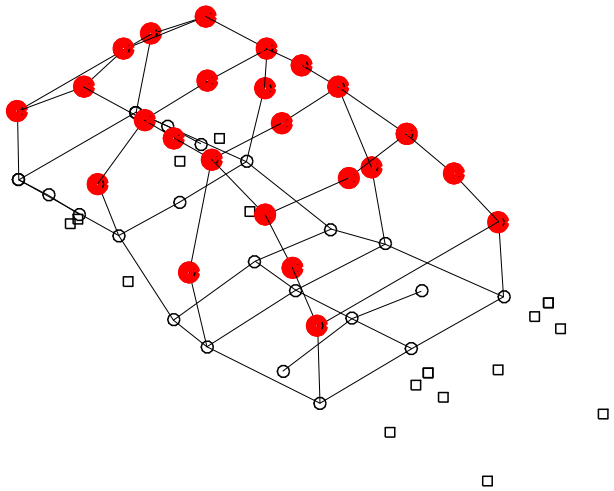

Figure B.30: Highlighted points show the evaluation points used for the result plots in Figure B.29.

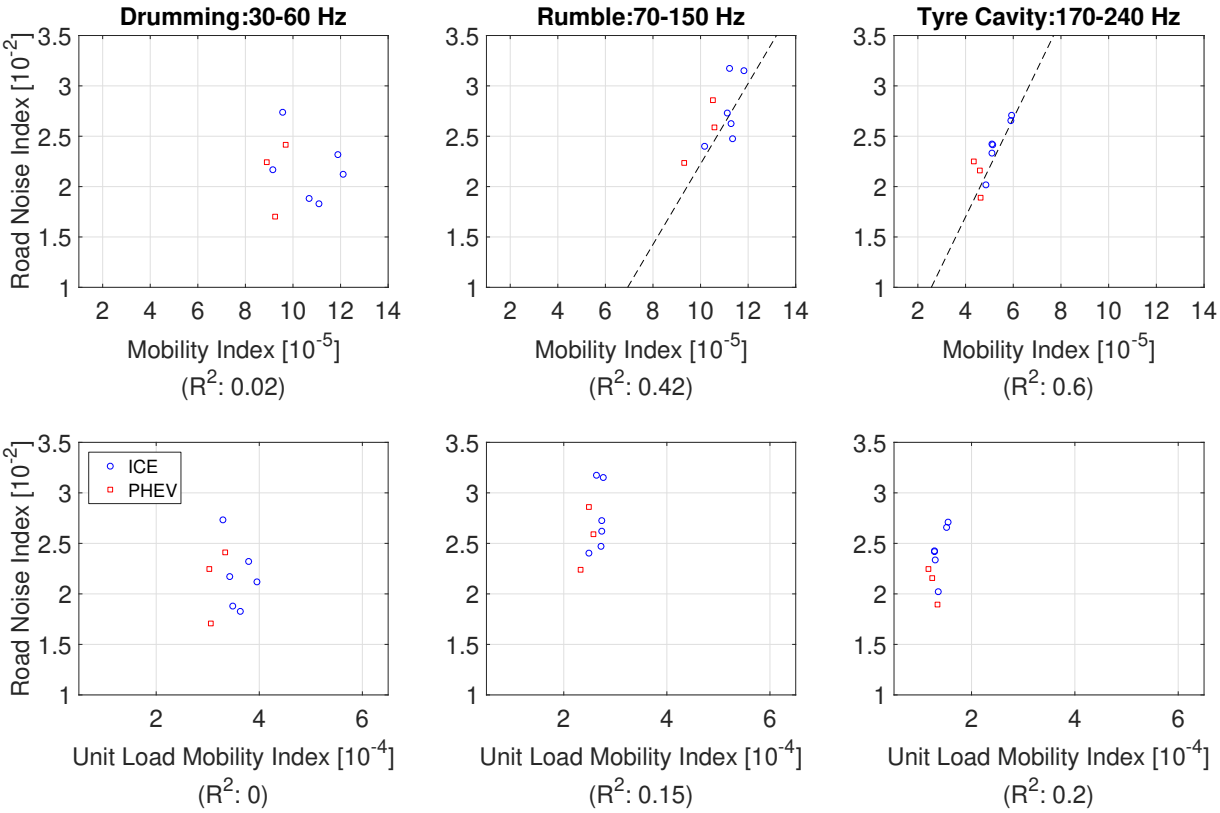

Figure B.31: The mobility index of the BIG, calculated both using the discretized forces described in Chapter 4 (top row) and a unit load (bottom row), and the road noise index. The mobility index is calculated using the evaluation points highlighted in Figure B.32. The dotted line is the linear approximation acquired by use of linear regression, shown for datasets with $R^2 > 0.25$.

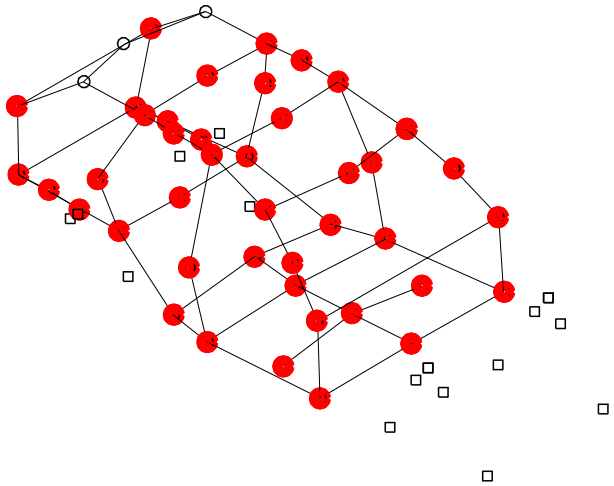

Figure B.32: Highlighted points show the evaluation points used for the result plots in Figure B.31.

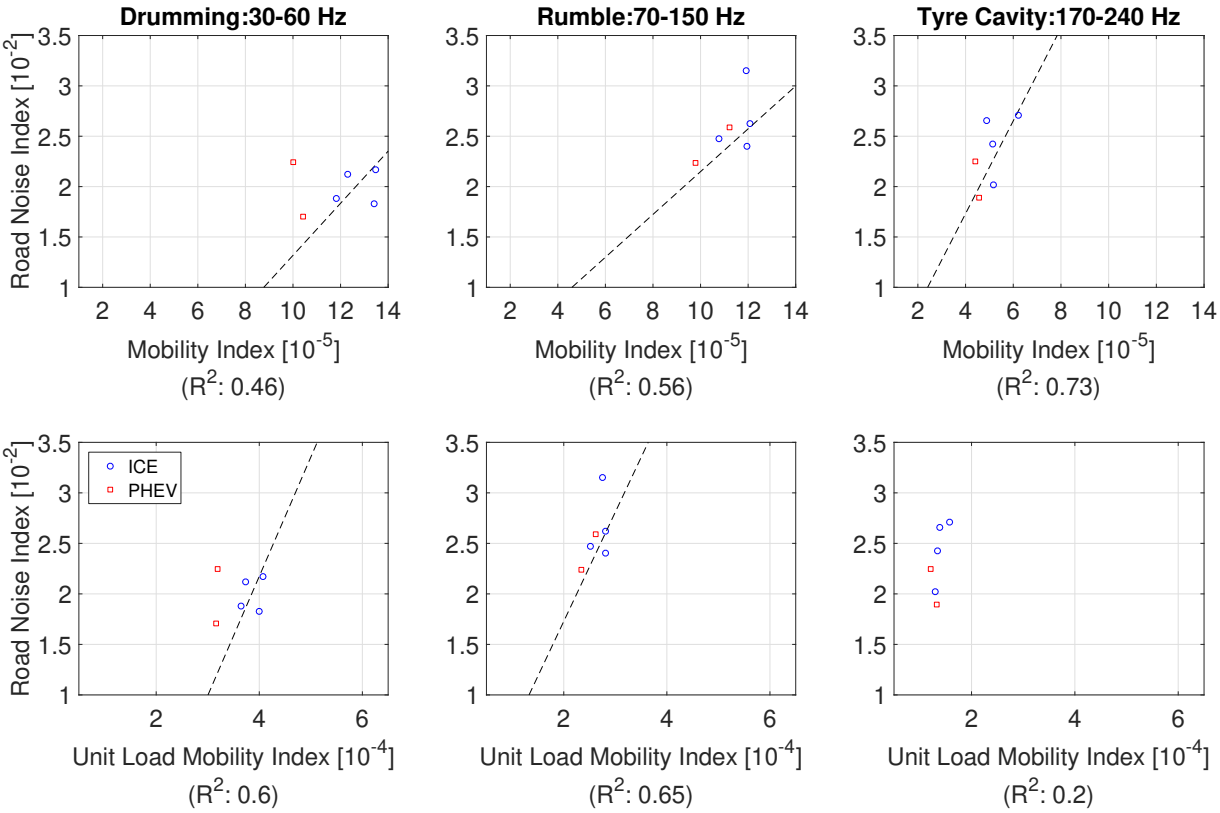

Figure B.33: The mobility index of the BIG, calculated both using the discretized forces described in Chapter 4 (top row) and a unit load (bottom row), and the road noise index. The mobility index is calculated using the evaluation points highlighted in Figure B.34. The dotted line is the linear approximation acquired by use of linear regression, shown for datasets with $R^2 > 0.25$.

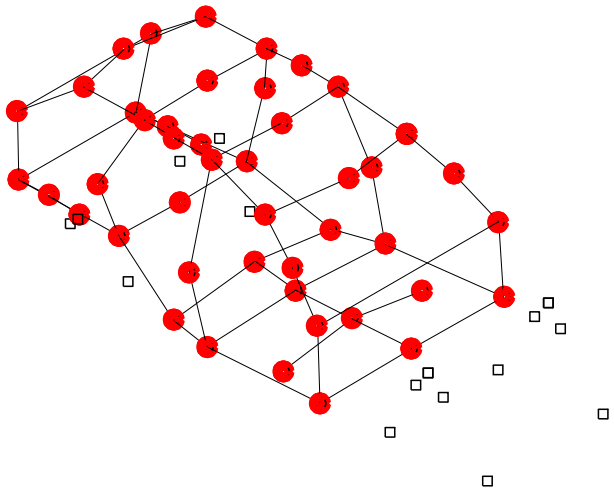

Figure B.34: Highlighted points show the evaluation points used for the result plots in Figure B.33.

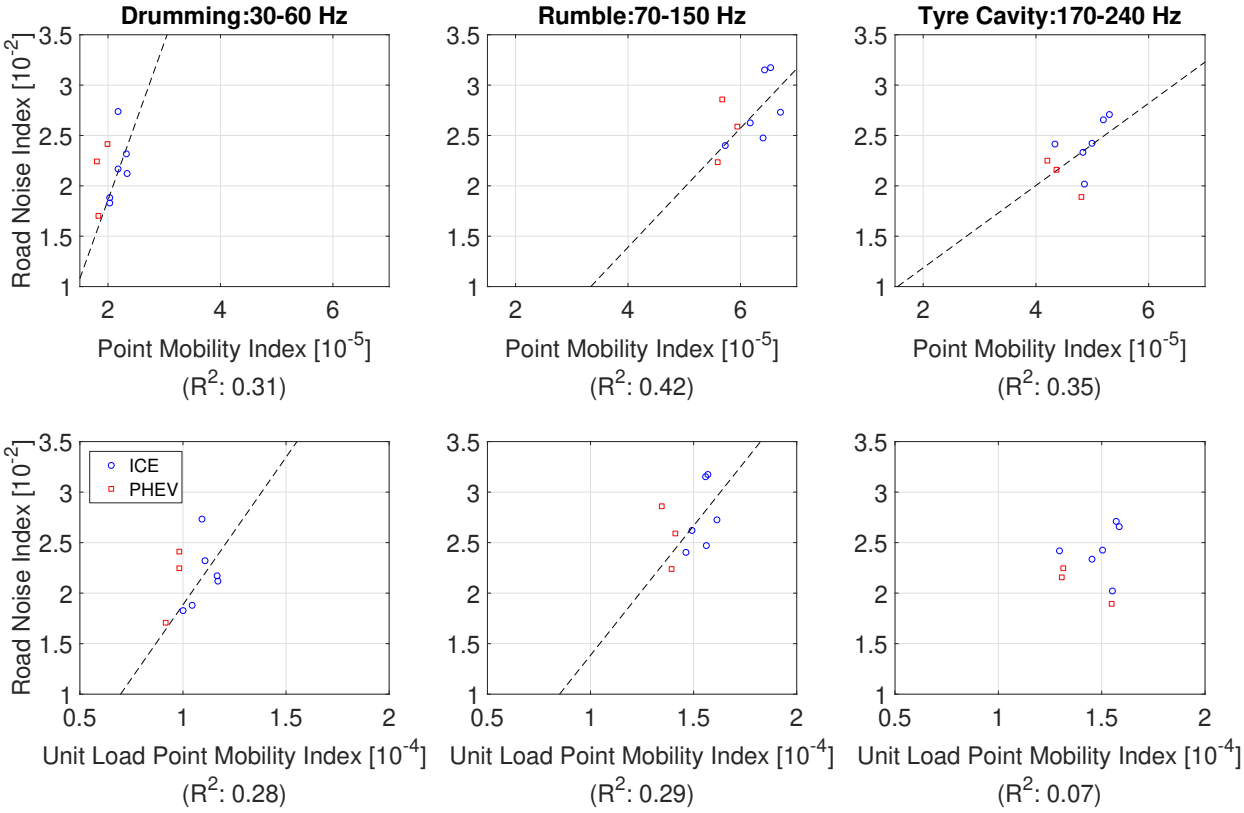

Figure B.35: The point mobility index of the BIG, calculated both using the discretized forces described in Chapter 4 (top row) and a unit load (bottom row), and the road noise index. The point mobility index is calculated using the evaluation points highlighted in Figure B.36. The dotted line is the linear approximation acquired by use of linear regression, shown for datasets with $R^2 > 0.25$.

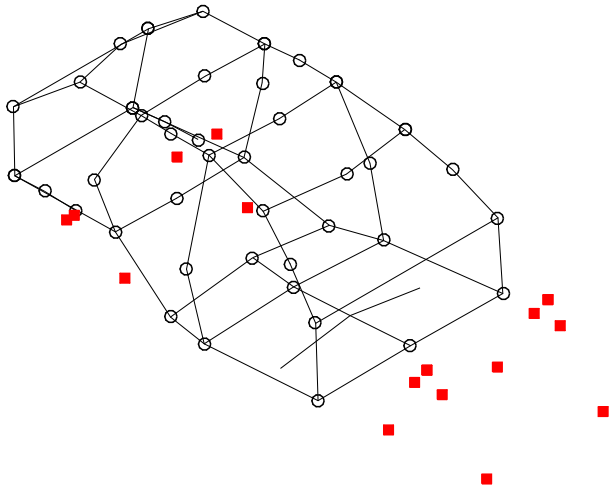

Figure B.36: Highlighted points show the evaluation points used for the result plots in Figure B.35.

B.2 Case Study

In Figures B.37–B.71 the results for the mobility index used as an early measure for all the subset of points analyzed is shown. The position of these evaluation points are the same as those used in the survey. Additionally the results are presented in the same order as the survey.

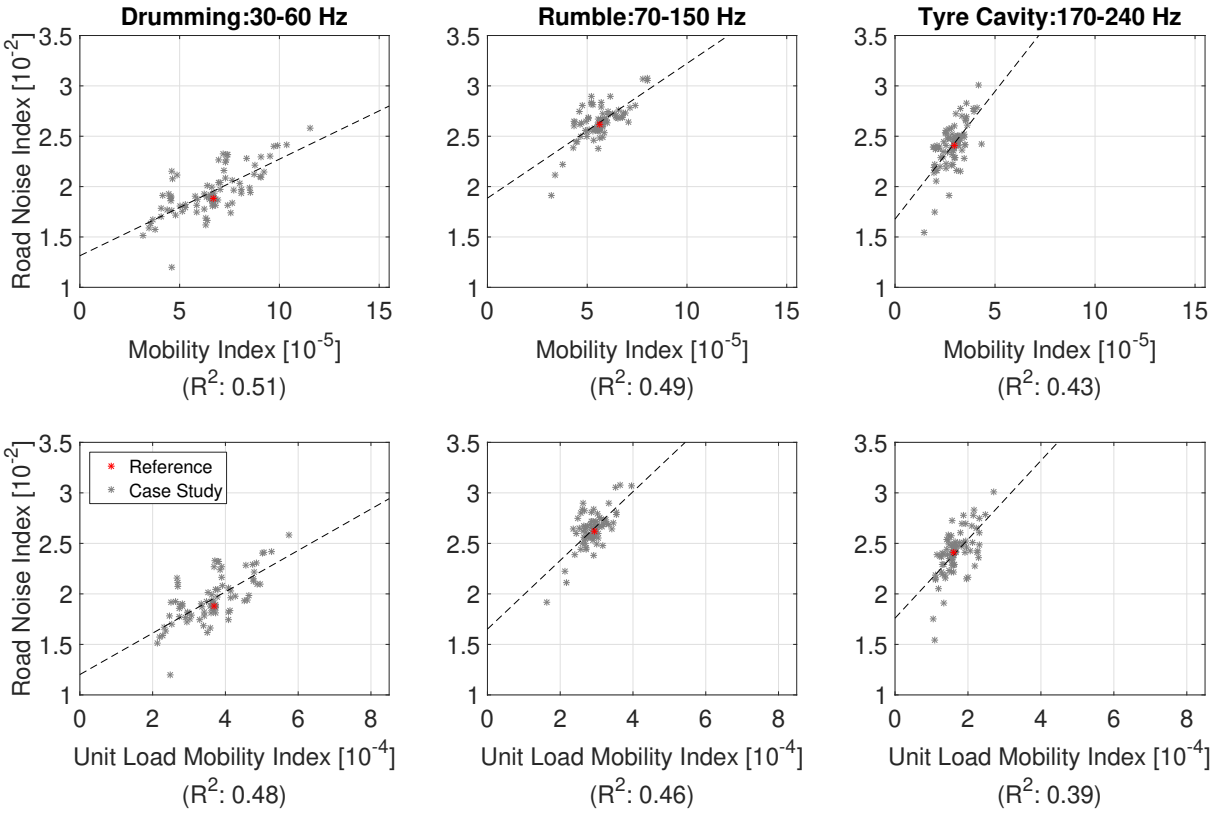

Figure B.37: The mobility index of the BIG, calculated both using the road-induced forces described in Chapter 4 (top row) and a unit load (bottom row), and the road noise index. The mobility index is calculated using the evaluation points highlighted in Figure B.38. The dotted line is the linear approximation acquired by use of linear regression, shown for datasets with $R^2 > 0.25$.

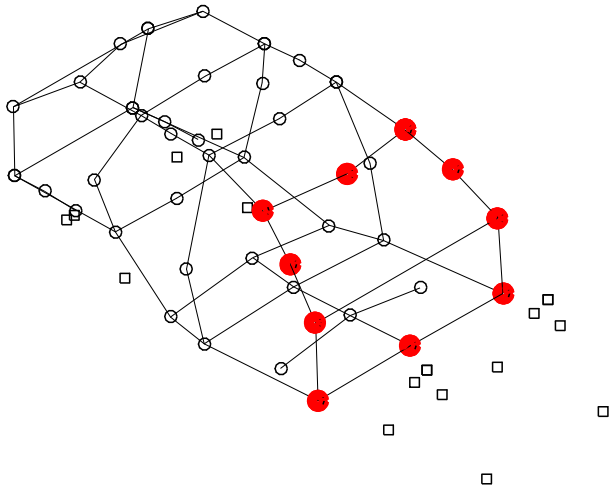

Figure B.38: Highlighted points show the evaluation points used for the result plots in Figure B.37.

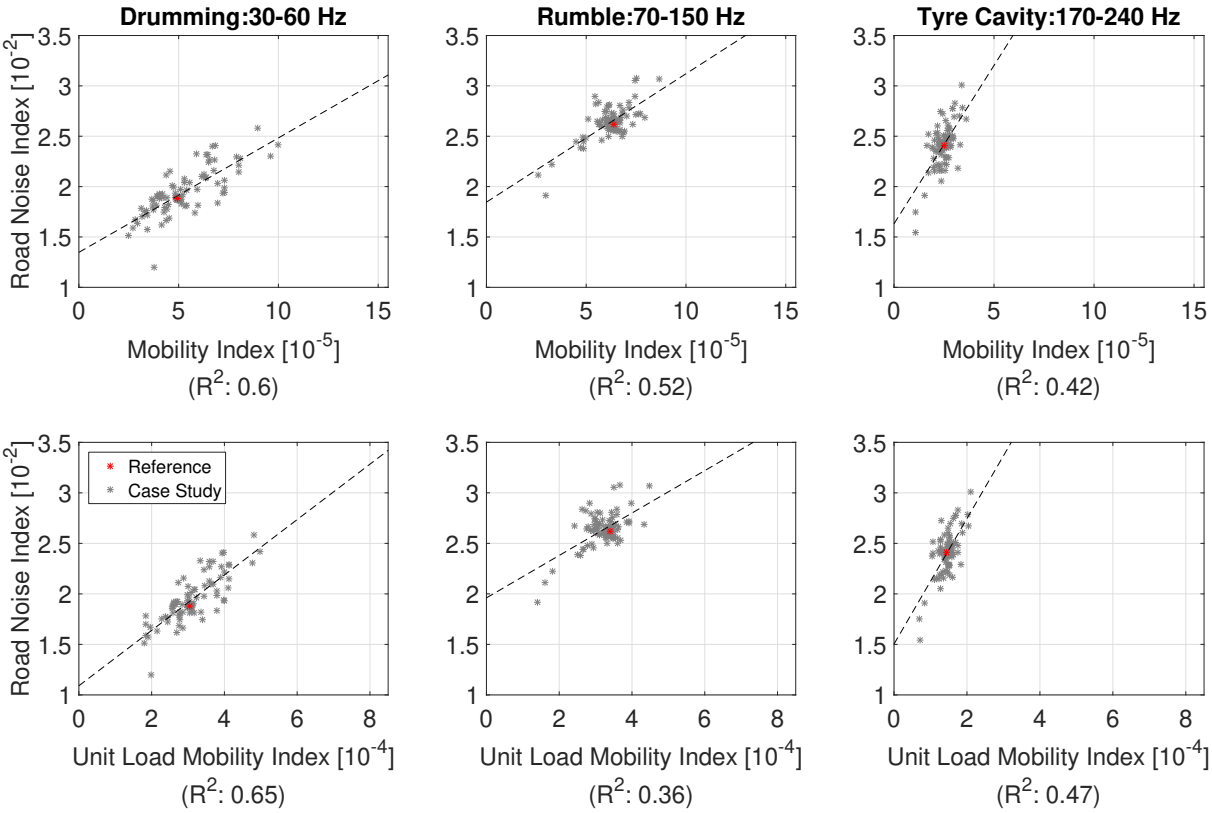

Figure B.39: The mobility index of the BIG, calculated both using the road-induced forces described in Chapter 4 (top row) and a unit load (bottom row), and the road noise index. The mobility index is calculated using the evaluation points highlighted in Figure B.40. The dotted line is the linear approximation acquired by use of linear regression, shown for datasets with $R^2 > 0.25$.

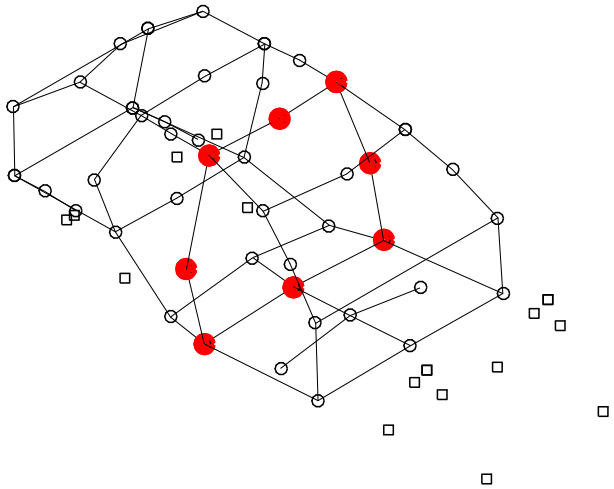

Figure B.40: Highlighted points show the evaluation points used for the result plots in Figure B.39.

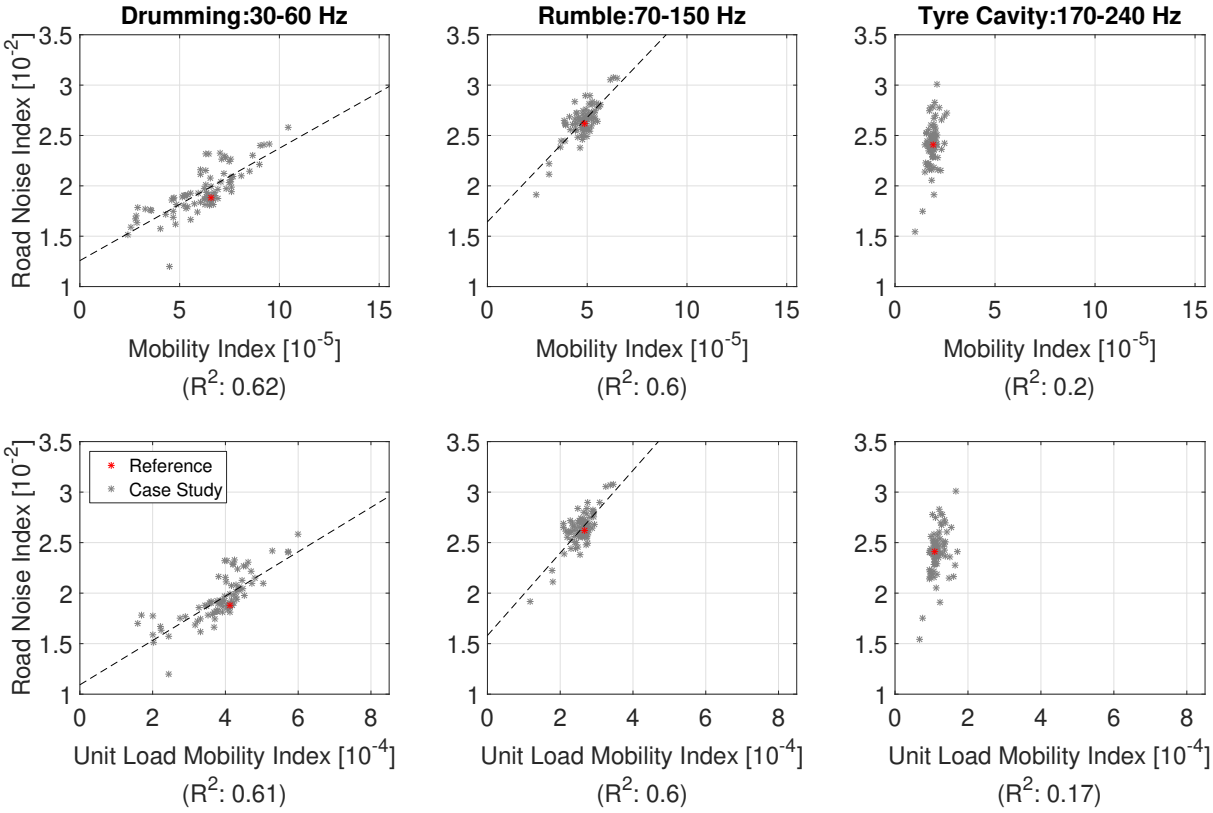

Figure B.41: The mobility index of the BIG, calculated both using the road-induced forces described in Chapter 4 (top row) and a unit load (bottom row), and the road noise index. The mobility index is calculated using the evaluation points highlighted in Figure B.42. The dotted line is the linear approximation acquired by use of linear regression, shown for datasets with $R^2 > 0.25$.

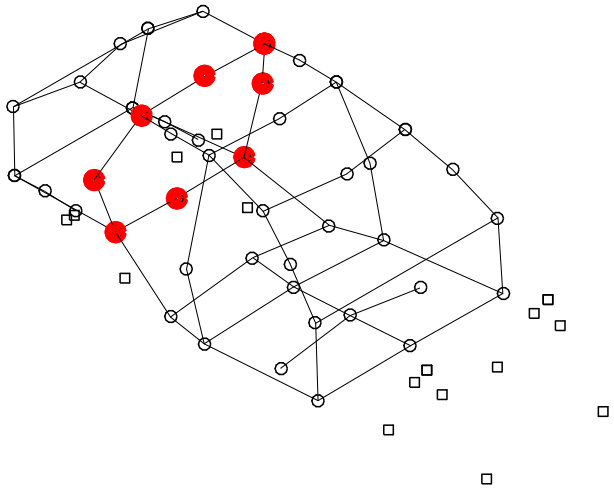

Figure B.42: Highlighted points show the evaluation points used for the result plots in Figure B.41.

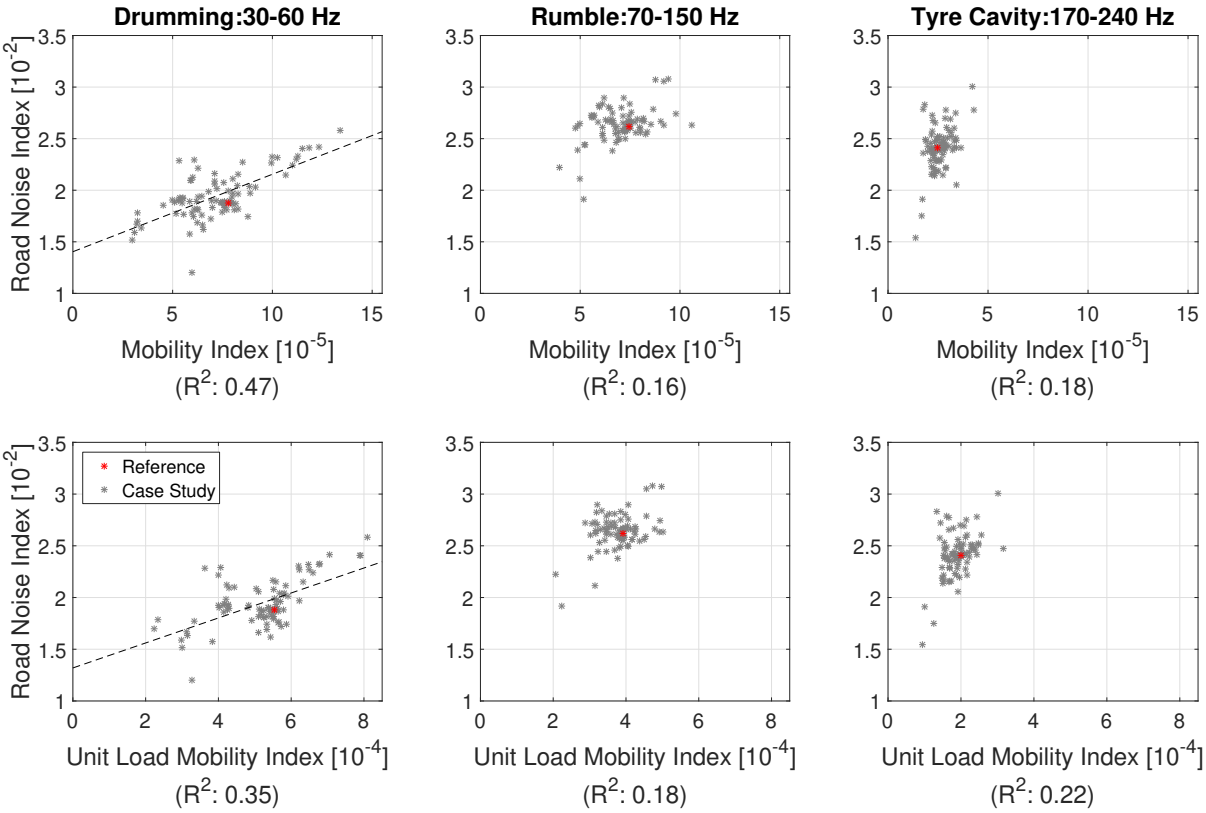

Figure B.43: The mobility index of the BIG, calculated both using the road-induced forces described in Chapter 4 (top row) and a unit load (bottom row), and the road noise index. The mobility index is calculated using the evaluation points highlighted in Figure B.44. The dotted line is the linear approximation acquired by use of linear regression, shown for datasets with $R^2 > 0.25$.

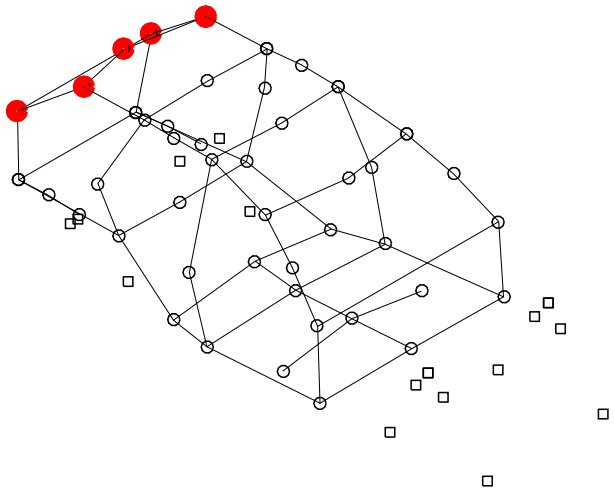

Figure B.44: Highlighted points show the evaluation points used for the result plots in Figure B.43.

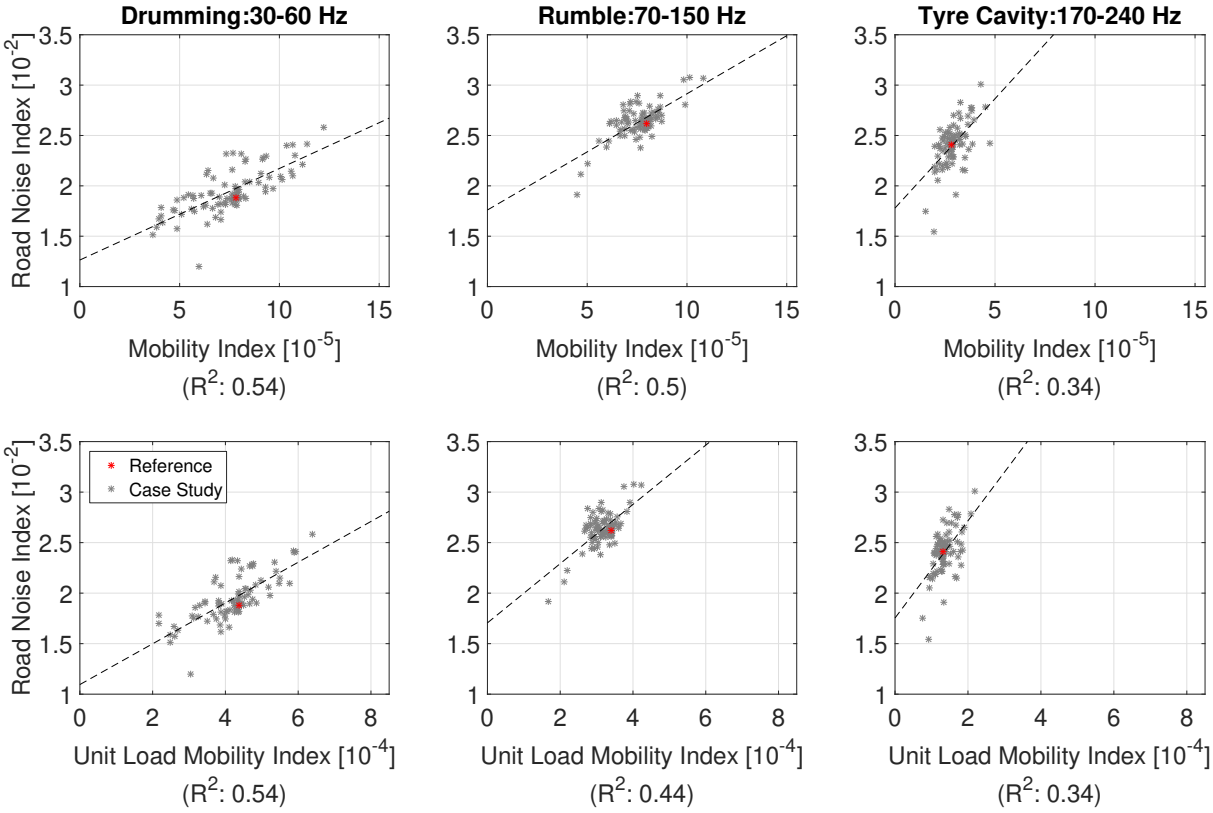

Figure B.45: The mobility index of the BIG, calculated both using the road-induced forces described in Chapter 4 (top row) and a unit load (bottom row), and the road noise index. The mobility index is calculated using the evaluation points highlighted in Figure B.46. The dotted line is the linear approximation acquired by use of linear regression, shown for datasets with $R^2 > 0.25$.

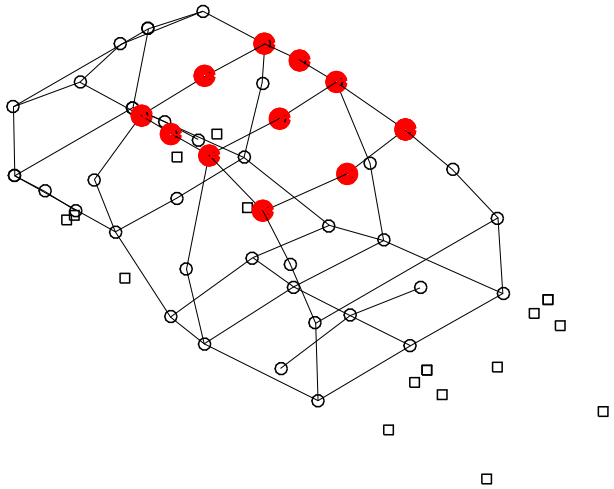

Figure B.46: Highlighted points show the evaluation points used for the result plots in Figure B.45.

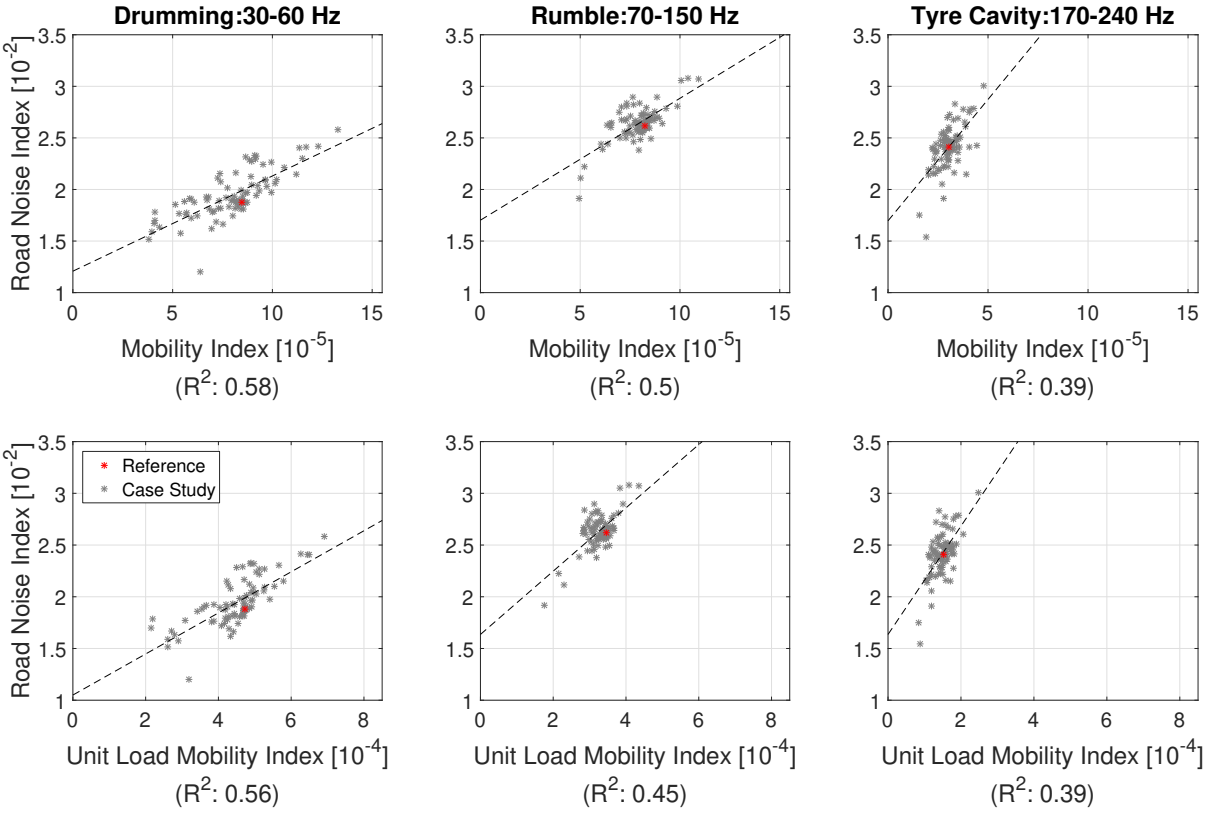

Figure B.47: The mobility index of the BIG, calculated both using the road-induced forces described in Chapter 4 (top row) and a unit load (bottom row), and the road noise index. The mobility index is calculated using the evaluation points highlighted in Figure B.48. The dotted line is the linear approximation acquired by use of linear regression, shown for datasets with $R^2 > 0.25$.

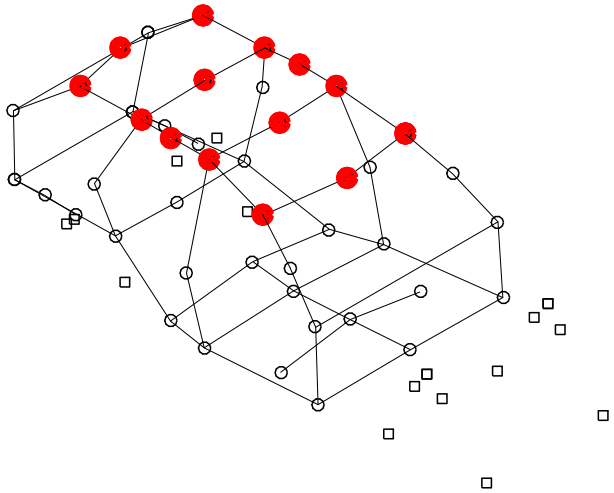

Figure B.48: Highlighted points show the evaluation points used for the result plots in Figure B.47.

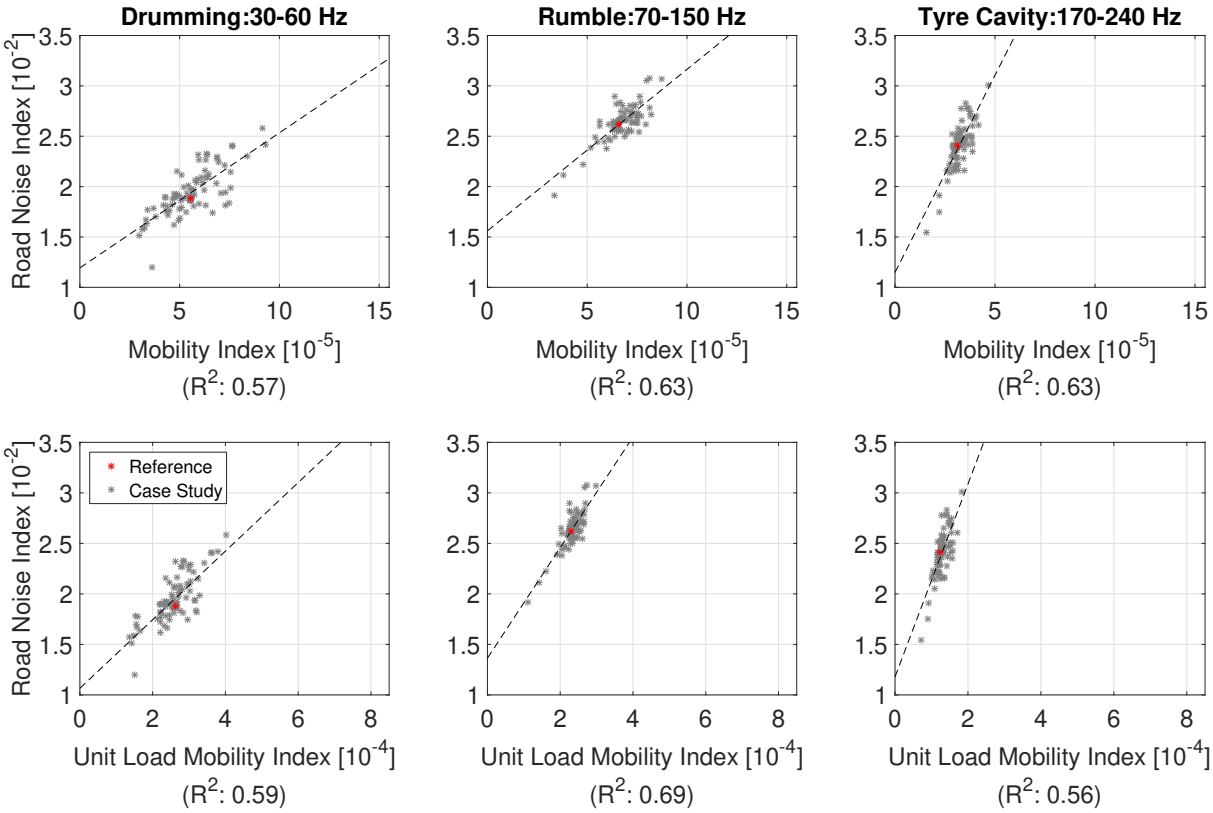

Figure B.49: The mobility index of the BIG, calculated both using the road-induced forces described in Chapter 4 (top row) and a unit load (bottom row), and the road noise index. The mobility index is calculated using the evaluation points highlighted in Figure B.50. The dotted line is the linear approximation acquired by use of linear regression, shown for datasets with $R^2 > 0.25$.

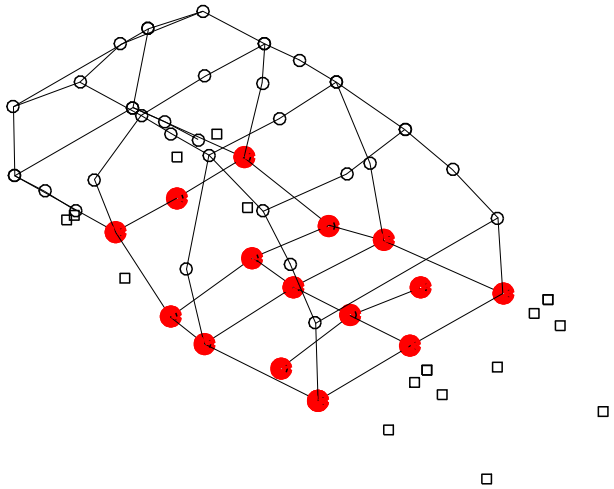

Figure B.50: Highlighted points show the evaluation points used for the result plots in Figure B.49.

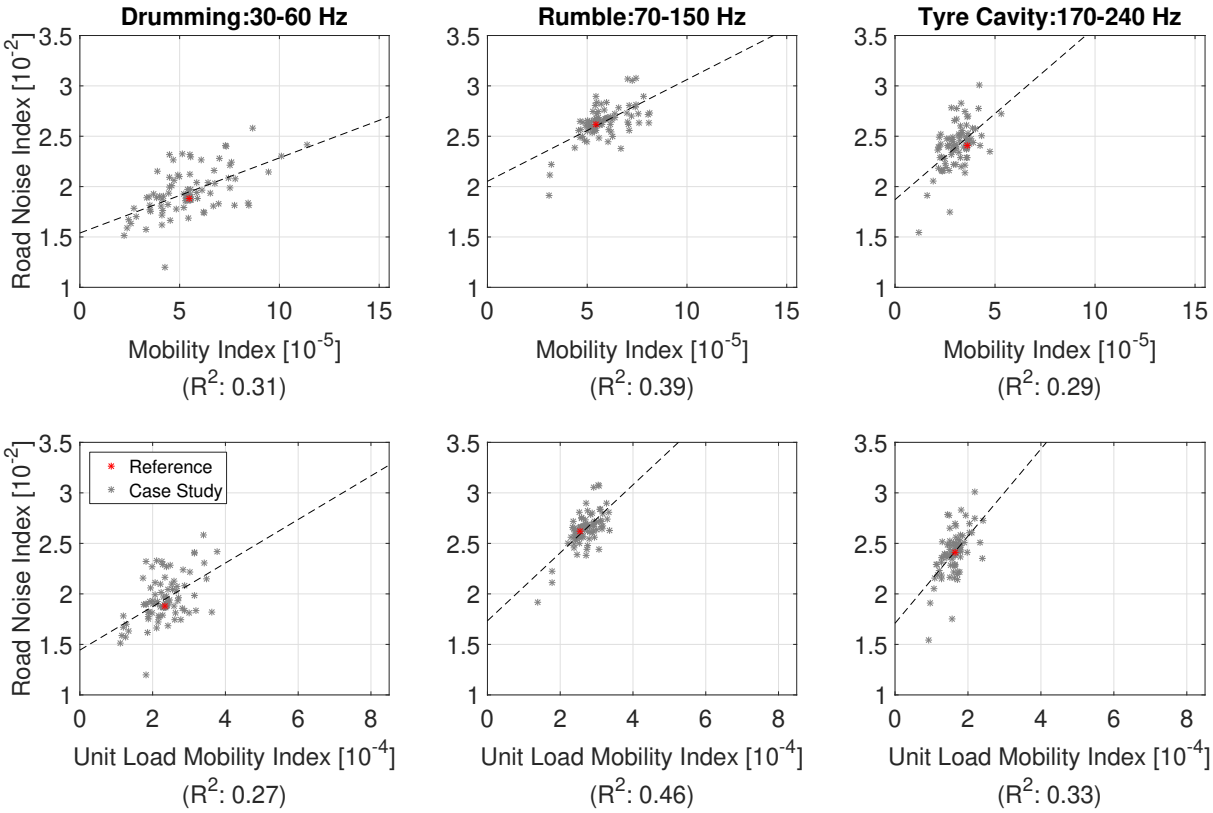

Figure B.51: The mobility index of the BIG, calculated both using the road-induced forces described in Chapter 4 (top row) and a unit load (bottom row), and the road noise index. The mobility index is calculated using the evaluation points highlighted in Figure B.52. The dotted line is the linear approximation acquired by use of linear regression, shown for datasets with $R^2 > 0.25$.

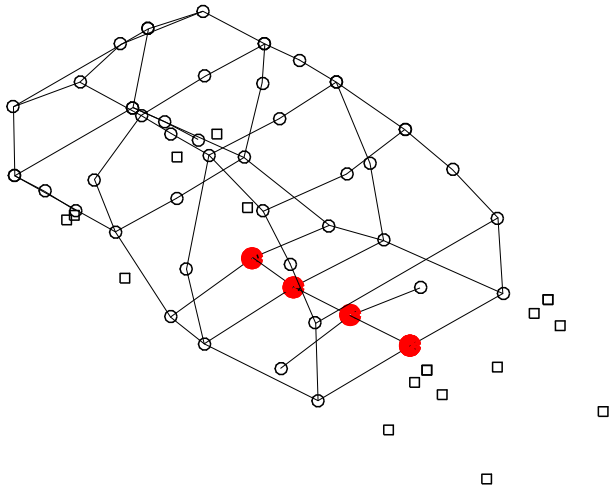

Figure B.52: Highlighted points show the evaluation points used for the result plots in Figure B.51.

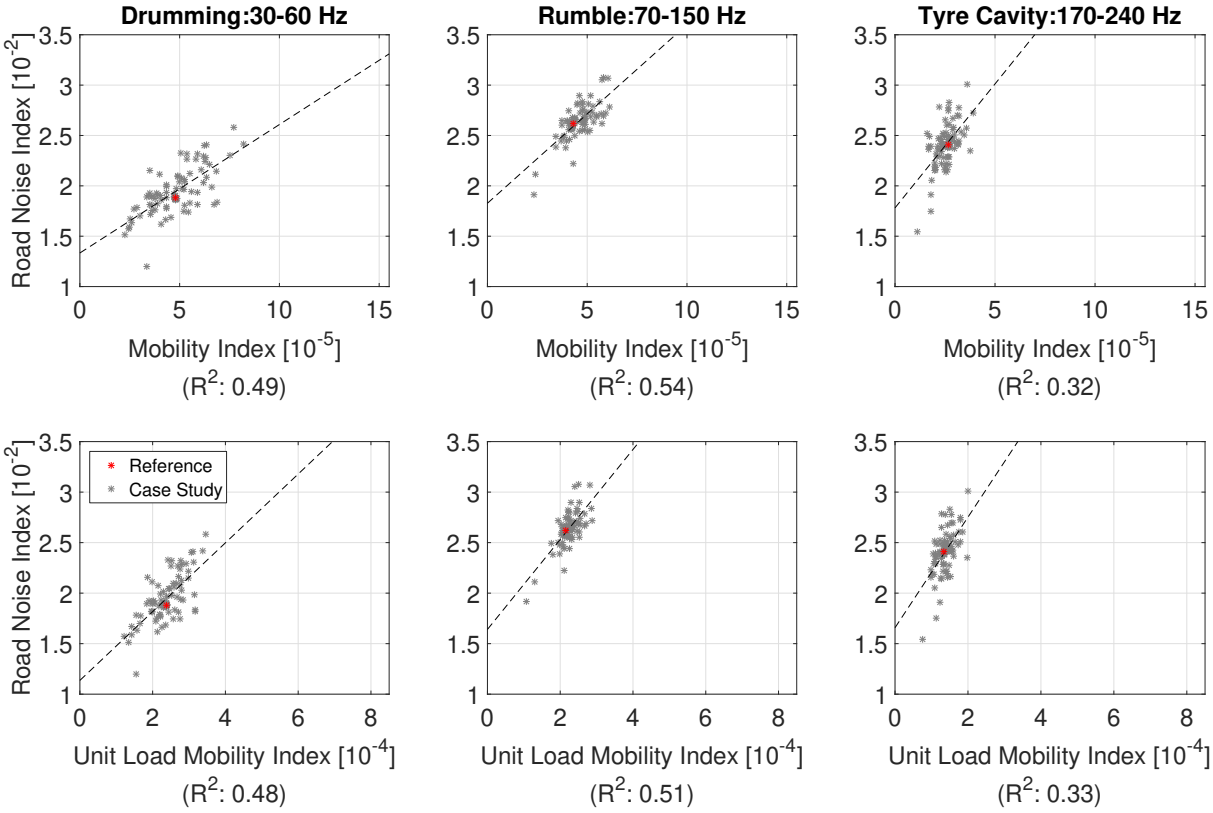

Figure B.53: The mobility index of the BIG, calculated both using the road-induced forces described in Chapter 4 (top row) and a unit load (bottom row), and the road noise index. The mobility index is calculated using the evaluation points highlighted in Figure B.54. The dotted line is the linear approximation acquired by use of linear regression, shown for datasets with $R^2 > 0.25$.

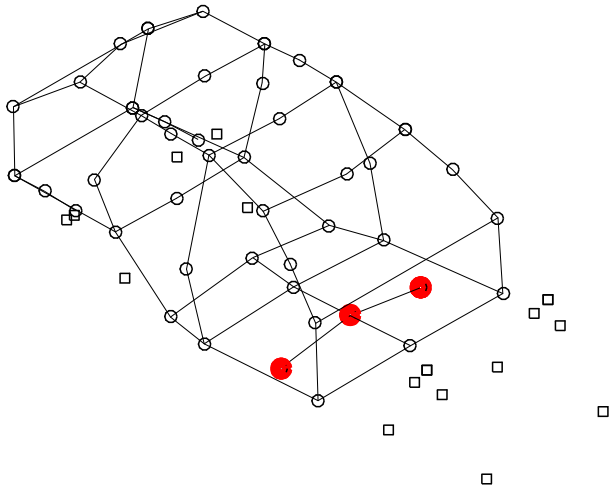

Figure B.54: Highlighted points show the evaluation points used for the result plots in Figure B.53.

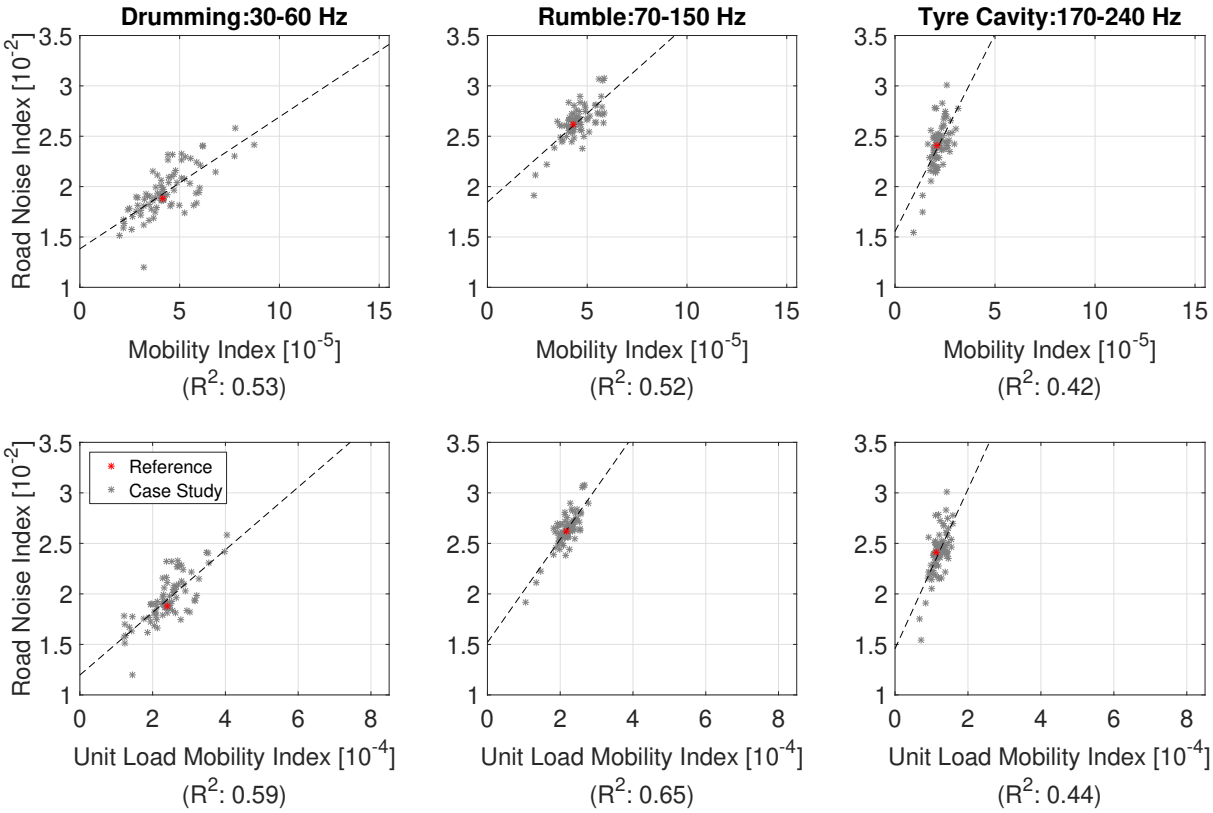

Figure B.55: The mobility index of the BIG, calculated both using the road-induced forces described in Chapter 4 (top row) and a unit load (bottom row), and the road noise index. The mobility index is calculated using the evaluation points highlighted in Figure B.56. The dotted line is the linear approximation acquired by use of linear regression, shown for datasets with $R^2 > 0.25$.

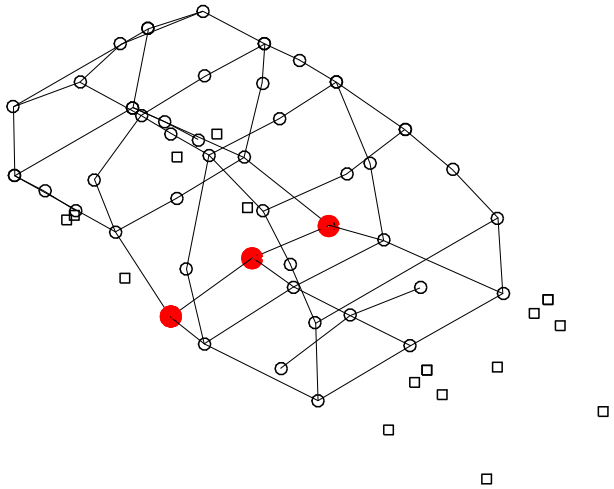

Figure B.56: Highlighted points show the evaluation points used for the result plots in Figure B.55.

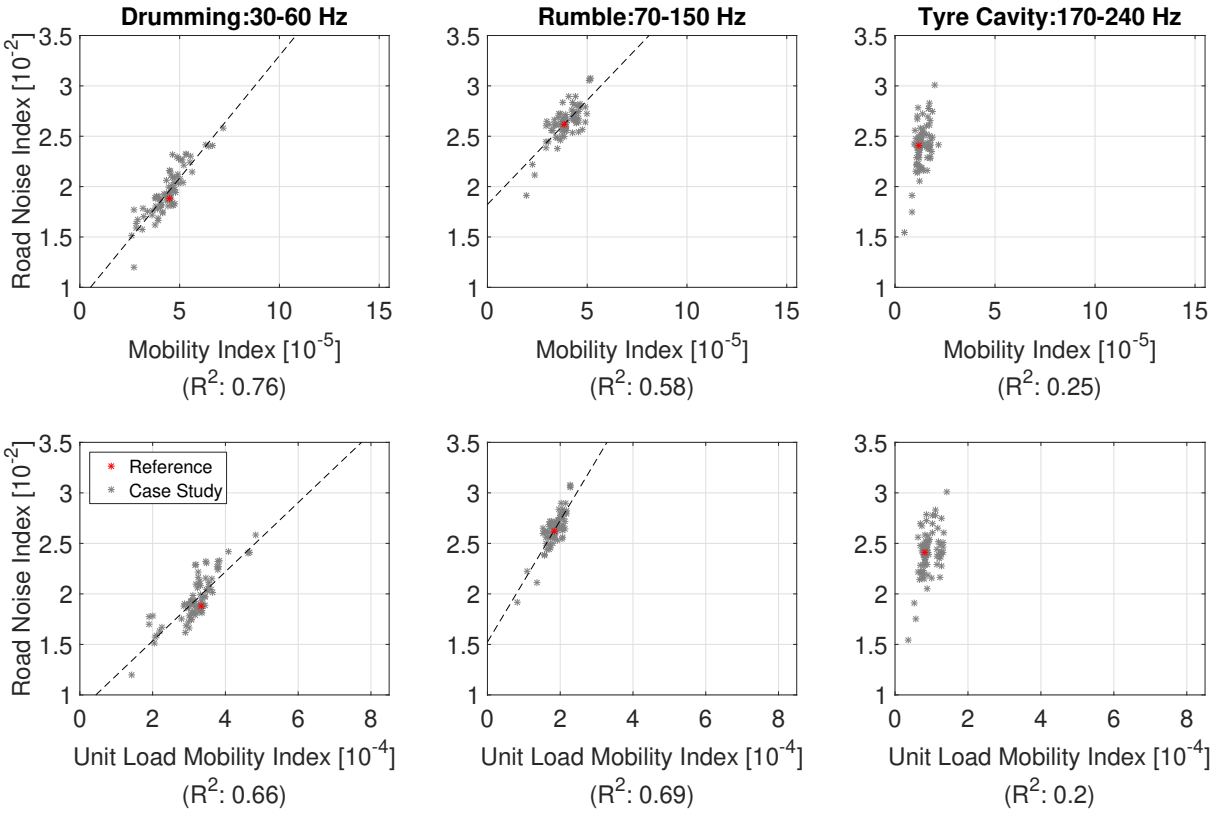

Figure B.57: The mobility index of the BIG, calculated both using the road-induced forces described in Chapter 4 (top row) and a unit load (bottom row), and the road noise index. The mobility index is calculated using the evaluation points highlighted in Figure B.58. The dotted line is the linear approximation acquired by use of linear regression, shown for datasets with $R^2 > 0.25$.

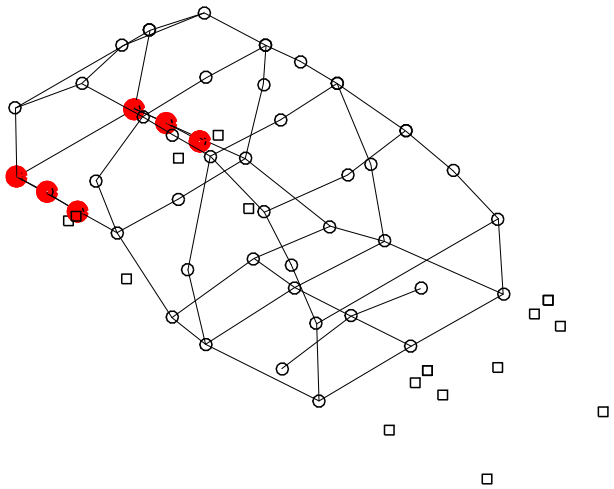

Figure B.58: Highlighted points show the evaluation points used for the result plots in Figure B.57.

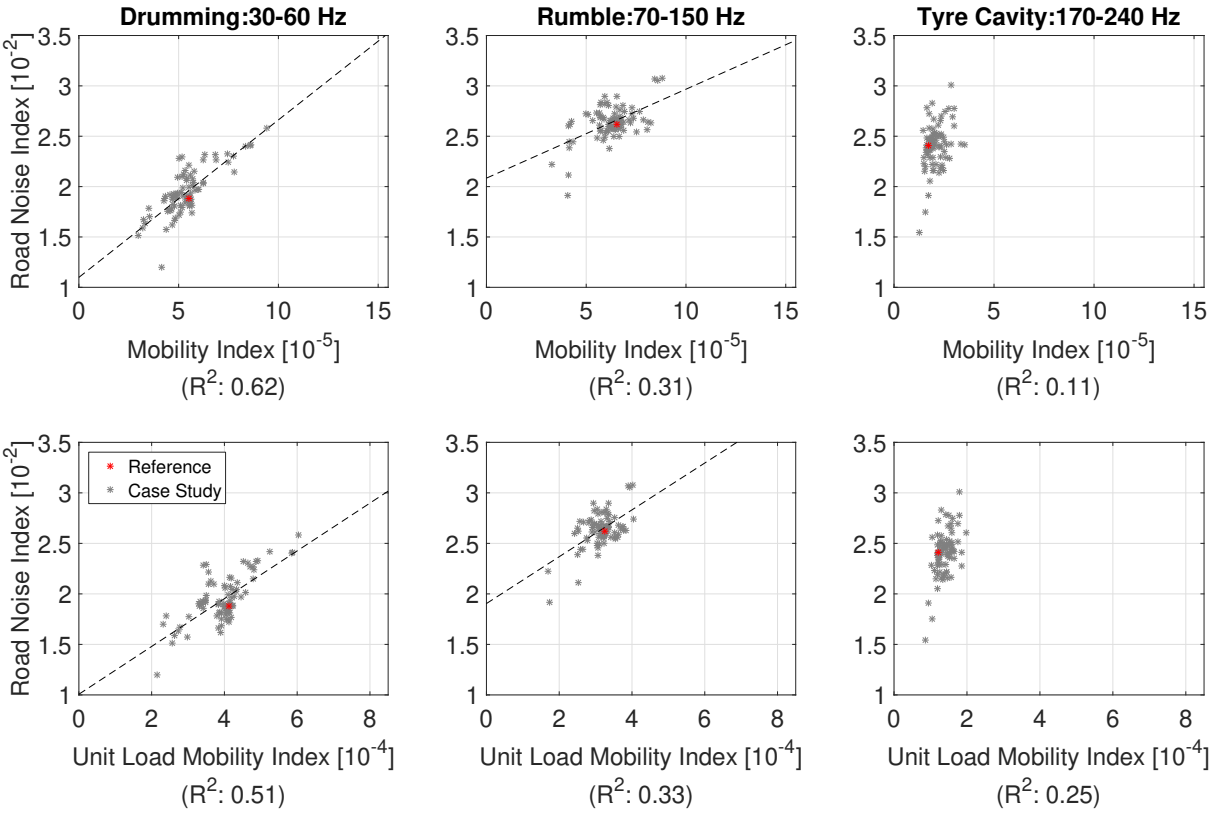

Figure B.59: The mobility index of the BIG, calculated both using the road-induced forces described in Chapter 4 (top row) and a unit load (bottom row), and the road noise index. The mobility index is calculated using the evaluation points highlighted in Figure B.60. The dotted line is the linear approximation acquired by use of linear regression, shown for datasets with $R^2 > 0.25$.

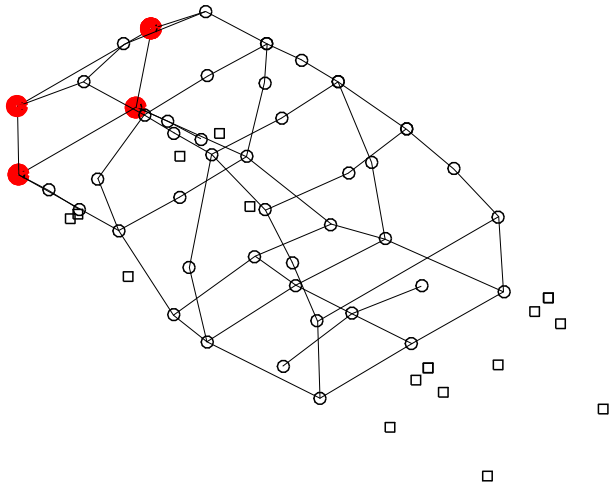

Figure B.60: Highlighted points show the evaluation points used for the result plots in Figure B.59.

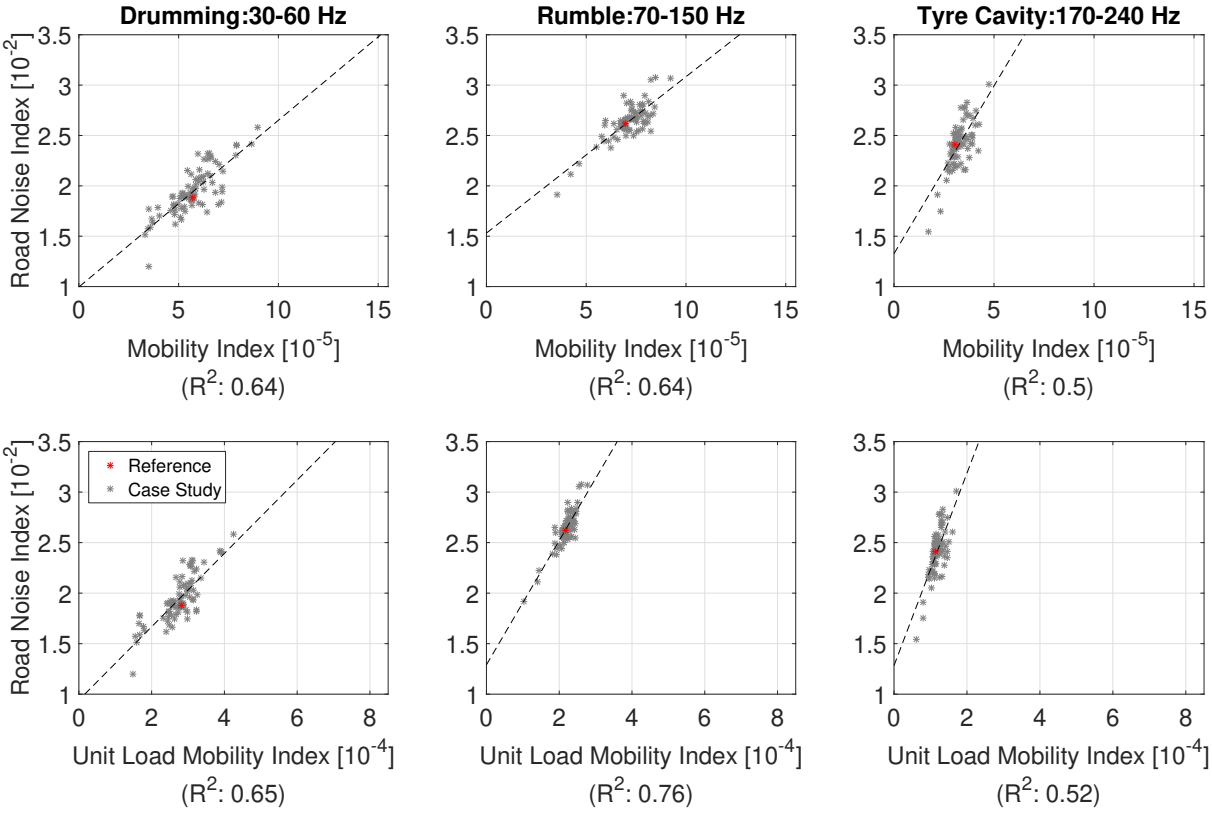

Figure B.61: The mobility index of the BIG, calculated both using the road-induced forces described in Chapter 4 (top row) and a unit load (bottom row), and the road noise index. The mobility index is calculated using the evaluation points highlighted in Figure B.62. The dotted line is the linear approximation acquired by use of linear regression, shown for datasets with $R^2 > 0.25$.

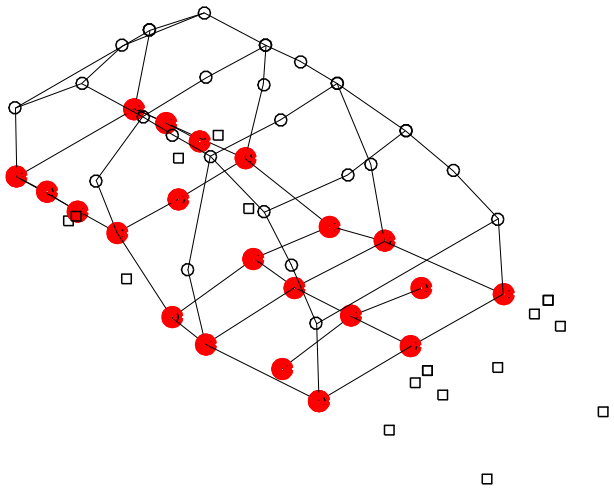

Figure B.62: Highlighted points show the evaluation points used for the result plots in Figure B.61.

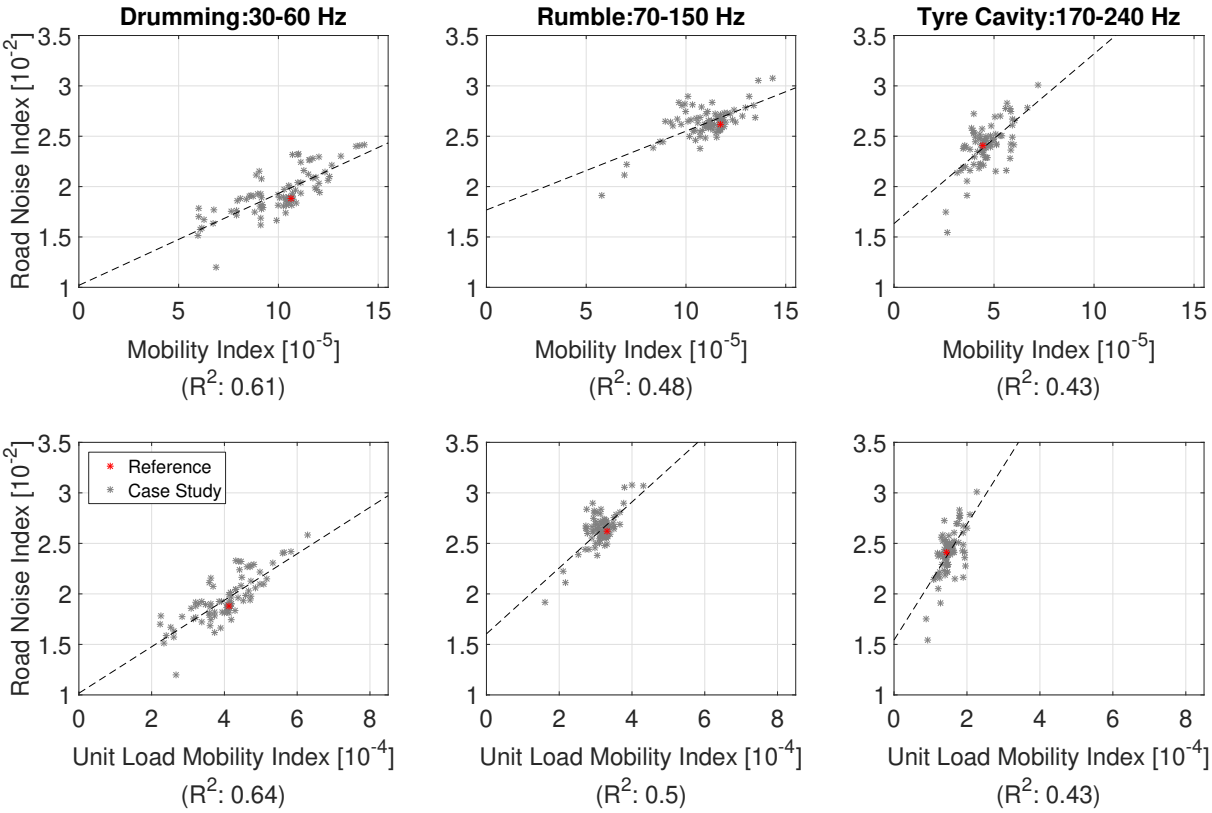

Figure B.63: The mobility index of the BIG, calculated both using the road-induced forces described in Chapter 4 (top row) and a unit load (bottom row), and the road noise index. The mobility index is calculated using the evaluation points highlighted in Figure B.64. The dotted line is the linear approximation acquired by use of linear regression, shown for datasets with $R^2 > 0.25$.

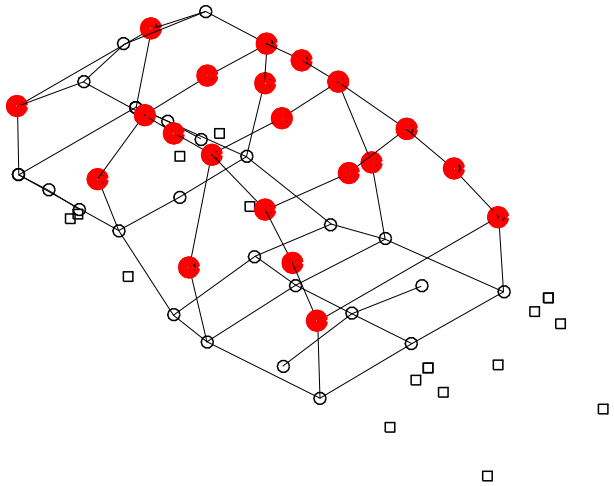

Figure B.64: Highlighted points show the evaluation points used for the result plots in Figure B.63.

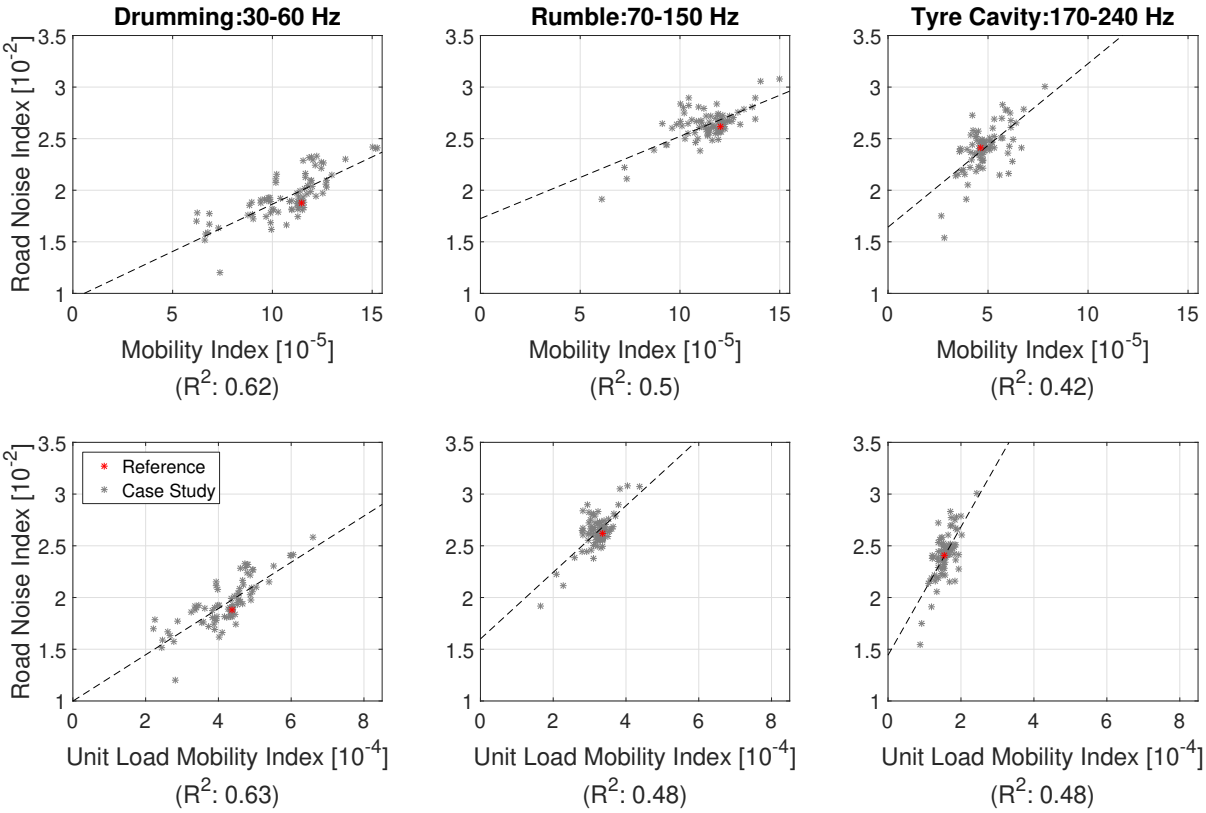

Figure B.65: The mobility index of the BIG, calculated both using the road-induced forces described in Chapter 4 (top row) and a unit load (bottom row), and the road noise index. The mobility index is calculated using the evaluation points highlighted in Figure B.66. The dotted line is the linear approximation acquired by use of linear regression, shown for datasets with $R^2 > 0.25$.

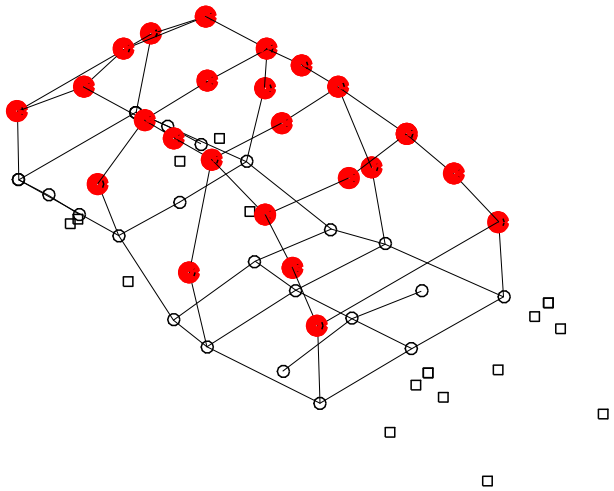

Figure B.66: Highlighted points show the evaluation points used for the result plots in Figure B.65.

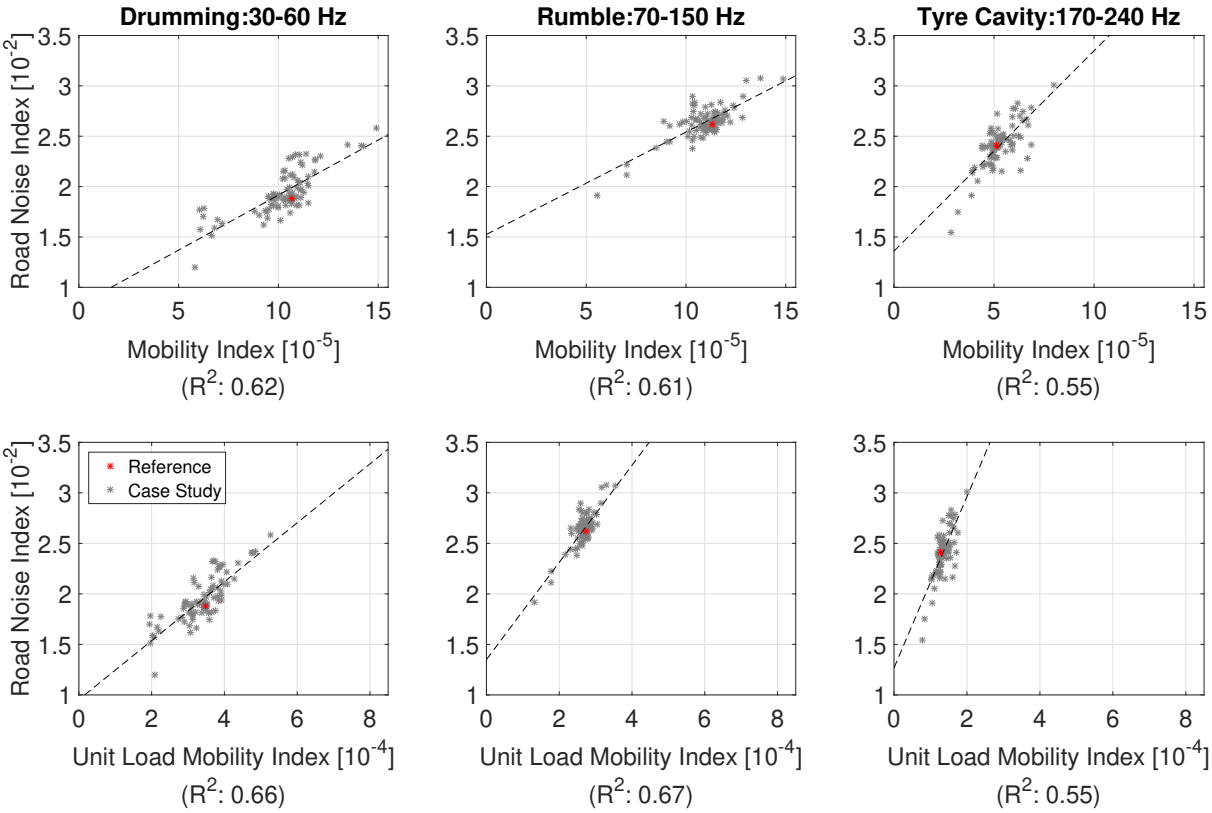

Figure B.67: The mobility index of the BIG, calculated both using the road-induced forces described in Chapter 4 (top row) and a unit load (bottom row), and the road noise index. The mobility index is calculated using the evaluation points highlighted in Figure B.68. The dotted line is the linear approximation acquired by use of linear regression, shown for datasets with $R^2 > 0.25$.

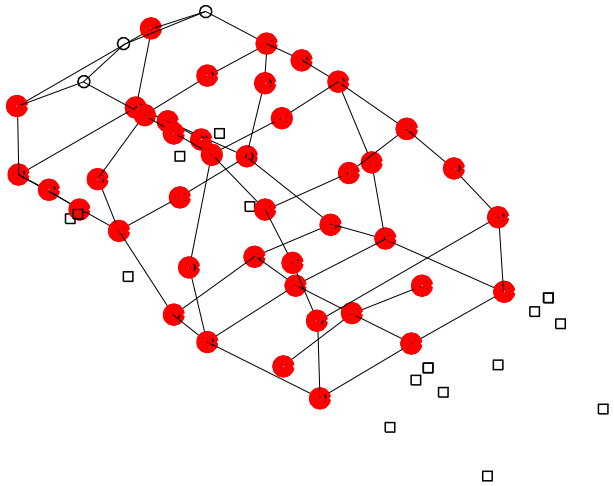

Figure B.68: Highlighted points show the evaluation points used for the result plots in Figure B.67.

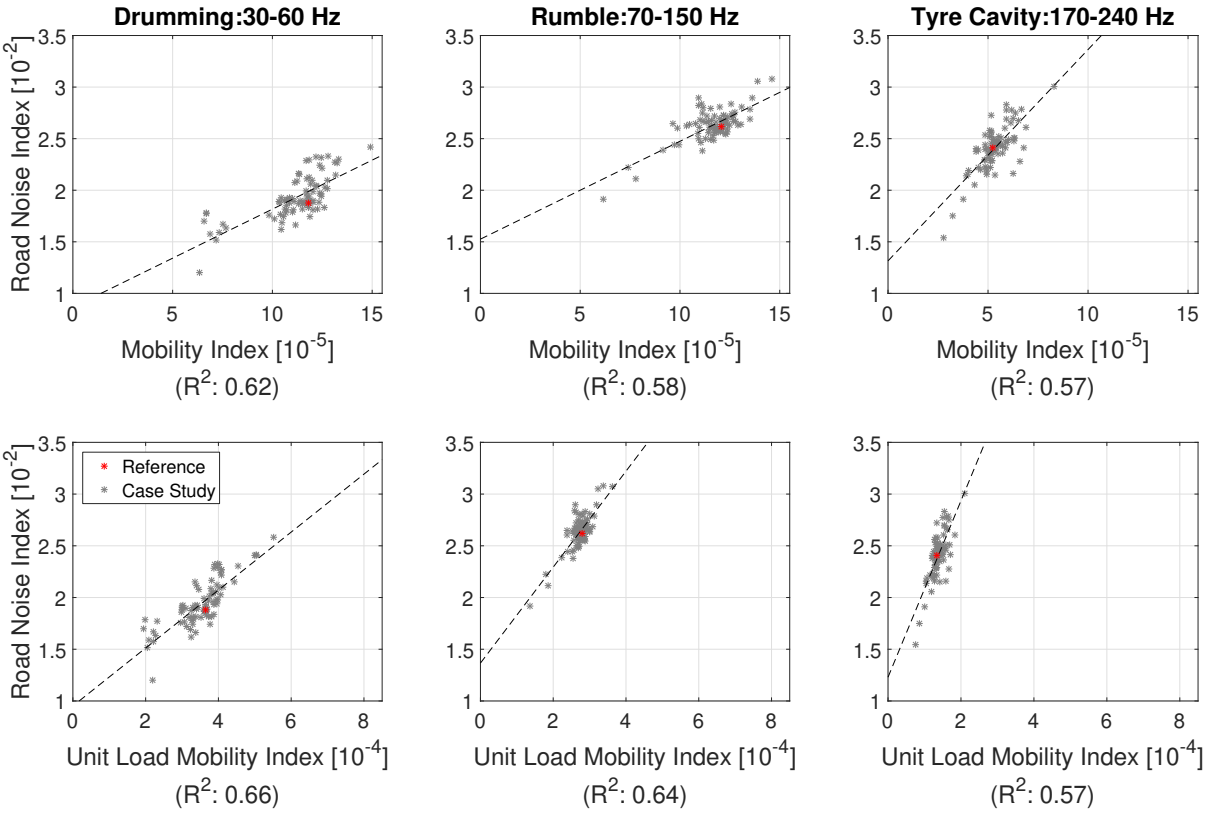

Figure B.69: The mobility index of the BIG, calculated both using the road-induced forces described in Chapter 4 (top row) and a unit load (bottom row), and the road noise index. The mobility index is calculated using the evaluation points highlighted in Figure B.70. The dotted line is the linear approximation acquired by use of linear regression, shown for datasets with $R^2 > 0.25$.

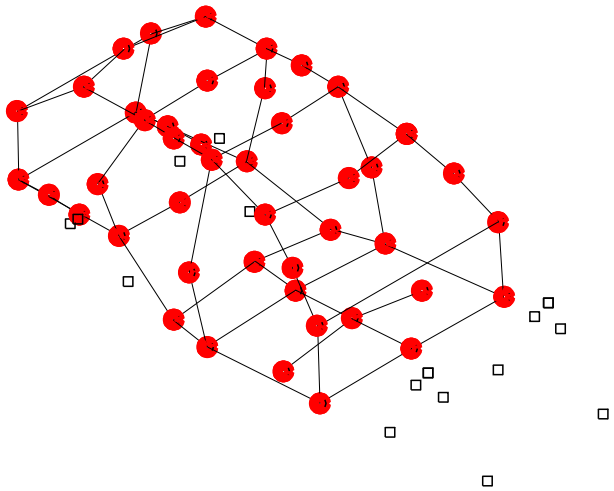

Figure B.70: Highlighted points show the evaluation points used for the result plots in Figure B.69.

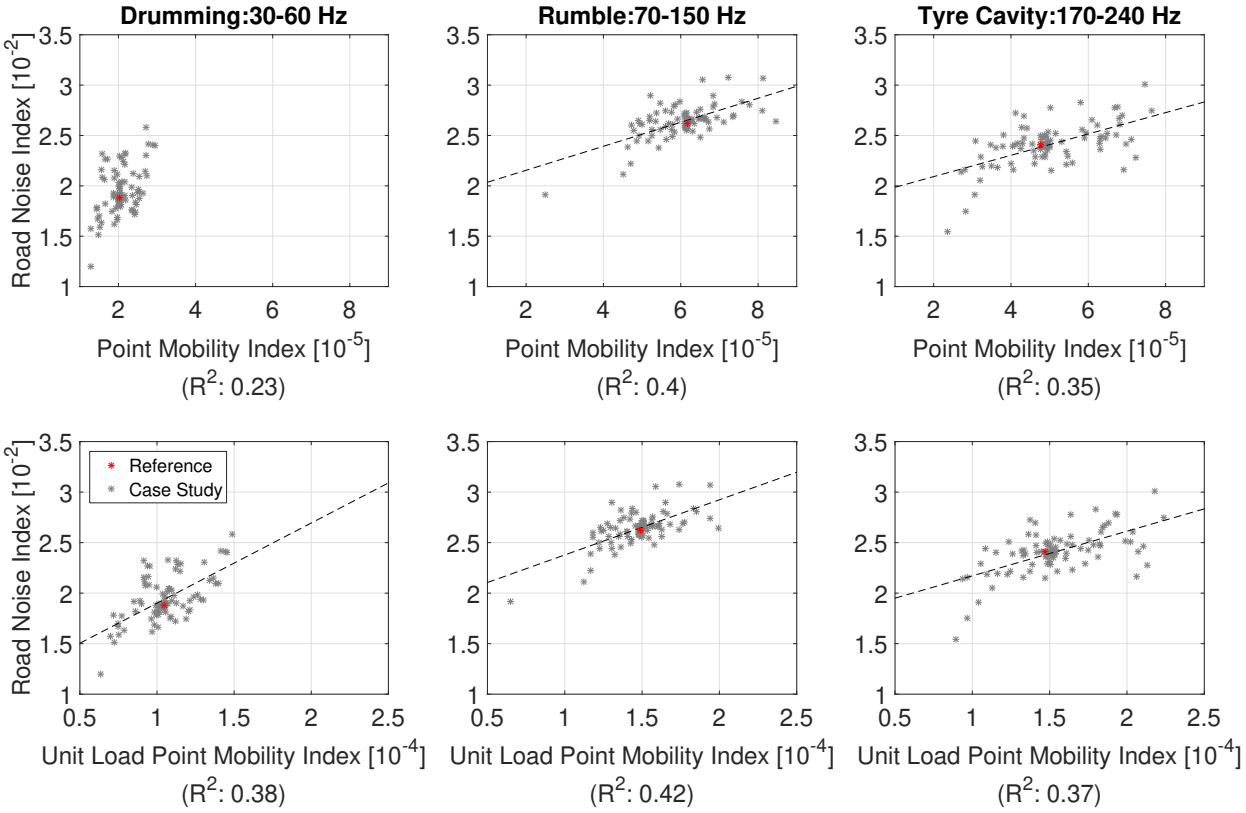

Figure B.71: The point mobility index of the BIG, calculated both using the road-induced forces described in Chapter 4 (top row) and a unit load (bottom row), and the road noise index. The point mobility index is calculated using the evaluation points highlighted in Figure B.72. The dotted line is the linear approximation acquired by use of linear regression, shown for datasets with $R^2 > 0.25$.

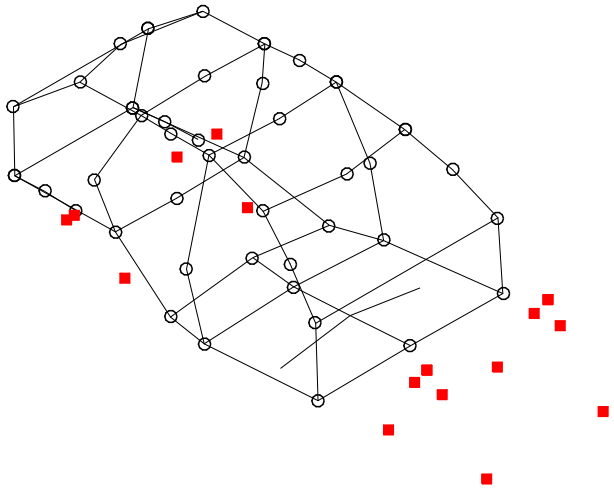

Figure B.72: Highlighted points show the evaluation points used for the result plots in Figure B.71.

C. Variation of Material Parameters Used in Case Study

In Table C.1 the variation of the material parameters used in the case study is shown.

Table C.1: Table describing how the material parameters were varied for the different simulation runs of the case study. -1 indicates a low setting, 0 a baseline and 1 high. The specific material parameters corresponding to these settings can be seen in Table 7.1

Run #	**E of Set #**							**ρ of Set #**						
	1	**2**	**3**	**4**	**5**	**6**	**7**	**1**	**2**	**3**	**4**	**5**	**6**	**7**
1	0	0	0	0	0	0	0	0	0	0	0	0	0	0
2	1	0	0	0	0	0	0	0	0	0	0	0	0	0
3	0	1	0	0	0	0	0	0	0	0	0	0	0	0
4	0	0	1	0	0	0	0	0	0	0	0	0	0	0
5	0	0	0	1	0	0	0	0	0	0	0	0	0	0
6	0	0	0	0	1	0	0	0	0	0	0	0	0	0
7	0	0	0	0	0	1	0	0	0	0	0	0	0	0
8	0	0	0	0	0	0	1	0	0	0	0	0	0	0
9	-1	0	0	0	0	0	0	0	0	0	0	0	0	0
10	0	1	0	0	0	0	0	0	0	0	0	0	0	0
11	0	0	-1	0	0	0	0	0	0	0	0	0	0	0
12	0	0	0	-1	0	0	0	0	0	0	0	0	0	0
13	0	0	0	0	-1	0	0	0	0	0	0	0	0	0
14	0	0	0	0	0	-1	0	0	0	0	0	0	0	0
15	0	0	0	0	0	0	-1	0	0	0	0	0	0	0
16	0	0	0	0	0	0	0	1	0	0	0	0	0	0
17	0	0	0	0	0	0	0	0	1	0	0	0	0	0
18	0	0	0	0	0	0	0	0	0	1	0	0	0	0
19	0	0	0	0	0	0	0	0	0	0	1	0	0	0
20	0	0	0	0	0	0	0	0	0	0	0	1	0	0
21	0	0	0	0	0	0	0	0	0	0	0	0	1	0
22	0	0	0	0	0	0	0	0	0	0	0	0	0	1
23	0	0	0	0	0	0	0	-1	0	0	0	0	0	0
24	0	0	0	0	0	0	0	0	-1	0	0	0	0	0
25	0	0	0	0	0	0	0	0	0	-1	0	0	0	0

Continued on next page

Table C.1 – continued from previous page

Run #	E of Set #							ρ of Set #						
	1	**2**	**3**	**4**	**5**	**6**	**7**	**1**	**2**	**3**	**4**	**5**	**6**	**7**
26	0	0	0	0	0	0	0	0	0	0	-1	0	0	0
27	0	0	0	0	0	0	0	0	0	0	0	-1	0	0
28	0	0	0	0	0	0	0	0	0	0	0	0	-1	0
29	0	0	0	0	0	0	0	0	0	0	0	0	0	-1
30	1	1	1	1	1	1	1	0	0	0	0	0	0	0
31	-1	-1	-1	-1	-1	-1	-1	0	0	0	0	0	0	0
32	0	0	0	0	0	0	0	1	1	1	1	1	1	1
33	0	0	0	0	0	0	0	-1	-1	-1	-1	-1	-1	-1
34	1	1	1	1	1	1	1	1	1	1	1	1	1	1
35	-1	-1	-1	-1	-1	-1	-1	-1	-1	-1	-1	-1	-1	-1
36	-1	-1	-1	-1	-1	-1	-1	1	1	1	1	1	1	1
37	1	1	1	1	1	1	1	-1	-1	-1	-1	-1	-1	-1
38	0	1	1	1	1	1	1	0	0	0	0	0	0	1
39	0	1	1	1	1	1	1	1	1	1	1	1	1	-1
40	0	1	1	1	1	1	1	-1	-1	-1	-1	-1	-1	0
41	0	-1	-1	-1	-1	-1	-1	0	0	0	0	0	0	-1
42	0	-1	-1	-1	-1	-1	-1	1	1	1	1	1	1	0
43	0	-1	-1	-1	-1	-1	-1	-1	-1	-1	-1	-1	-1	1
44	1	0	0	1	1	-1	-1	0	0	1	1	-1	-1	0
45	1	0	0	1	1	-1	-1	1	1	-1	-1	0	0	1
46	1	0	0	1	1	-1	-1	-1	-1	0	0	1	1	-1
47	1	1	1	-1	-1	0	0	0	0	1	1	-1	-1	1
48	1	1	1	-1	-1	0	0	1	1	-1	-1	0	0	-1
49	1	1	1	-1	-1	0	0	-1	-1	0	0	1	1	0
50	1	-1	-1	0	0	1	1	0	0	1	1	-1	-1	-1
51	1	-1	-1	0	0	1	1	1	1	-1	-1	0	0	0
52	1	-1	-1	0	0	1	1	-1	-1	0	0	1	1	1
53	-1	0	1	0	-1	1	-1	0	1	0	-1	1	-1	0
54	-1	0	1	0	-1	1	-1	1	-1	1	0	-1	0	1
55	-1	0	1	0	-1	1	-1	-1	0	-1	1	0	1	-1
56	-1	1	-1	1	0	-1	0	0	1	0	-1	1	-1	1
57	-1	1	-1	1	0	-1	0	1	-1	1	0	-1	0	-1
58	-1	1	-1	1	0	-1	0	-1	0	-1	1	0	1	0
59	-1	-1	0	-1	1	0	1	0	1	0	-1	1	-1	-1
60	-1	-1	0	-1	1	0	1	1	-1	1	0	-1	0	0
61	-1	-1	0	-1	1	0	1	-1	0	-1	1	0	1	1
62	0	0	-1	-1	1	1	0	0	-1	-1	1	1	0	0
63	0	0	-1	-1	1	1	0	1	0	0	-1	-1	1	1
64	0	0	-1	-1	1	1	0	-1	1	1	0	0	-1	-1
65	0	1	0	0	-1	-1	1	0	-1	-1	1	1	0	1
66	0	1	0	0	-1	-1	1	1	0	0	-1	-1	1	-1

Continued on next page

Table C.1 – continued from previous page

Run #	E of Set #							ρ of Set #						
	1	**2**	**3**	**4**	**5**	**6**	**7**	**1**	**2**	**3**	**4**	**5**	**6**	**7**
67	0	1	0	0	-1	-1	1	-1	1	1	0	0	-1	0
68	0	-1	1	1	0	0	-1	0	-1	-1	1	1	0	-1
69	0	-1	1	1	0	0	-1	1	0	0	-1	-1	1	0
70	0	-1	1	1	0	0	-1	-1	1	1	0	0	-1	1
71	1	0	1	-1	0	-1	1	0	1	-1	0	-1	1	0
72	1	0	1	-1	0	-1	1	1	-1	0	1	0	-1	1
73	1	0	1	-1	0	-1	1	-1	0	1	-1	1	0	-1
74	1	1	-1	0	1	0	-1	0	1	-1	0	-1	1	1
75	1	1	-1	0	1	0	-1	1	-1	0	1	0	-1	-1
76	1	1	-1	0	1	0	-1	-1	0	1	-1	1	0	0
77	1	-1	0	1	-1	1	0	0	1	-1	0	-1	1	-1
78	1	-1	0	1	-1	1	0	1	-1	0	1	0	-1	0
79	1	-1	0	1	-1	1	0	-1	0	1	-1	1	0	1
80	-1	0	-1	1	-1	0	1	0	-1	1	-1	0	1	0
81	-1	0	-1	1	-1	0	1	1	0	-1	0	1	-1	1
82	-1	0	-1	1	-1	0	1	-1	1	0	1	-1	0	-1
83	-1	1	0	-1	0	1	-1	0	-1	1	-1	0	1	1
84	-1	1	0	-1	0	1	-1	1	0	-1	0	1	-1	-1
85	-1	1	0	-1	0	1	-1	-1	1	0	1	-1	0	0
86	-1	-1	1	0	1	-1	0	0	-1	1	-1	0	1	-1
87	-1	-1	1	0	1	-1	0	1	0	-1	0	1	-1	0
88	-1	-1	1	0	1	-1	0	-1	1	0	1	-1	0	1